UNIVERSITAT POLITÈCNICA DE CATALUNYA
BARCELONATECH
Escola d'Enginyeria de Telecomunicació
i Aeroespacial de Castelldefels

TREBALL DE FI DE GRAU

TÍTOL DEL TFG: Sweeping-jet active flow control actuation effects on boundary layer separation on airfoil at ultralow Reynolds

TITULACIÓ: Grau en Enginyeria d'Aeronavegació

AUTORS: Luciano Colitti Garcia
Javier Mateu López

DIRECTOR: Fernando Pablo Mellibovsky Elstein

DATA: February 8, 2019

Títol: Sweeping-jet active flow control actuation effects on boundary layer separation on airfoil

Autors: Luciano Colitti Garcia
Javier Mateu López

Director: Fernando Pablo Mellibovsky Elstein

Data: 8 de febrer de 2019

Resum

Els perfils alars pateixen un greu augment d'arrosegament i pèrdua de sustentació quan operen a grans angles d'atac. El control actiu té un gran potencial de millorar l'eficiència aerodinàmica als perfils 'off-design' que operen aquestes condicions.En aquest estudi s'han dut a terme múltiples simulacions mitjançant el software CFD Nektar++ per a demostrar l'habilitat que té el *sweeping jet* per millorar les condicions a un Reynolds baix. El *sweeping jet* és un possible *output* d'un oscil· lador fluídic sense parts mòbils que és capaç d'aconseguir que el fluid que passa através d'ell oscil·li a la tovera d'una manera estable. Aquest dispositiu ja ha estat provat prèvia i reeixidament en perfils amb faldó (Flaps), amb la clara intenció de sostenir el fluxe fins a la vora final d'aquest (trailing edge). En aquest estudi, un únic jet en un perfil 2D NACA0012 s'ha parametritzat, amb certes variables com a graus de llibertat per tal d'estudiar-ne el seu efecte. En primer lloc s'ha treballat una malla estructurada la qual s'ha reestructurat posteriorment amb l'objectiu d'incloure el jet sobre del perfil. Les simulacions demostren com amb el perfil cru sense jet, a Re=1000 i un angle d'atac a 9^o, la capa límit es desprén al 35% de la corda aproximadament. Els principals paràmetres modificats i testejats del jet han estat: la posició, el coeficient de moment, l'amplitud d'oscil·lació, la freqüència i l'angle d'apertura de la sortida del jet. El *sweeping jet* s'ha estudiat en dues configuracions: la primera apuntant perpendicular a l'extradós i oscil·lant al plà XY, i la segona quasi-tangencialment a l'extradós, és a dir, que la seva direcció principal és similar a la direcció *stream-wise*. En base a aquests resultats, hem obtingut que el jet tangencial permet tenir un control sobre el fluxe fent-lo reenganxarse un altre cop al perfil i augmentant significativament la sustentació. També s'ha trobat una forta relació entre la posició del jet sobre el perfil amb la trajectòria del fluid, el qual és determinant per a les característiques aerodinàmiques del perfil alar. Finalment, s'ha dut a terme un estudi en quasi-3D degut a l'importància trobada en altres articles amb respecte a la distància d'amplada entre dos jets consecutius en un ala finita. Aprofitant la homogeneitat en la direcció Z del nostre estudi, s'ha utilitzat una expansió de Fourier unimodal de nombre d'ona variable en la direcció *span-wise* per tal d'estudiar l'evolució dels paràmetres en direcció Z, el qual fa reduir el temps d'obtenció de resultats. Això, a més, ha possibilitat als autors la capacitat d'estudi d'estabilitat de l'ala en funció de la seva amplada.

Title : Sweeping-jet active flow control actuation effects on boundary layer separation on airfoil

Authors: Luciano Colitti Garcia
Javier Mateu López

Advisor: Fernando Pablo Mellibovsky Elstein

Date: February 8, 2019

Overview

Airfoils incur large drag penalty and a drop of lift production when operated at high angles of attack. Active flow control has a potential for improving the aerodynamic efficiency of airfoils at off-design operating conditions. Several simulations with Nektar++ CFD have been performed with intent to show the ability of sweeping jet active flow control method to improve performances of an airfoil at low Reynolds conditions. A sweeping jet is an output of a fluidic oscillator with no mobile parts which is able to make the fluid that goes through it to oscillate at its nozzle in a very stable way. This device has been previously successfully tested on airfoils with a deflected flap, with the intention of attach the boundary layer until the trailing edge. In this study, single sweeping jet on a 2D NACA0012 airfoil has been mathematically parameterized, with multiple degrees of freedom whose effect on the solution has been studied. In order to do so, a structured mesh containing the airfoil has been firstly studied and then modified with the aim of placing the jet on the airfoil's upper surface. Baseline calculations show that at Re=1000 and with an angle of attack of 9^o, the boundary layer detaches at 35% of the chord approximately. This study focuses on the effects on the boundary layer of the parameters of the sweeping-jet: the position, momentum coefficient, oscillation amplitude, frequency and opening angle have been modified. The sweeping jet has been studied in two configurations: the first one pointing normal to the airfoil's upper surface and oscillating in the XY plane, and the second one near tangential to the upper surface of the airfoil, that is, the jet's principal direction is almost the stream-wise direction. It oscillates on z-axis, but due to the fact that most experiments have been carried out in 2D, the frequency behaviour will be simulated represented by making the output velocity oscillate on its magnitude. The tangential configuration has been found to give the sweeping jet the authority to control flow by reattaching the boundary layer and significantly increase the lift coefficient of the airfoil. Also, it has been found a strong relationship between the jet's position over the upper surface of the airfoil and the trajectory of the fluid, which is determinant on the aerodynamic characteristics of a wing. Finally, a quasi-3D study has been carried out, due to the importance found on previous studies of the span-wise distance between two consecutive jets on a finite wing. Taking advantage of the homogeneity of the z direction in this experiment, in order to analyze the stability to span-wise-dependent perturbations a unimodal Fourier expansion of varying wave-number has been used in the span-wise direction, which reduces the computational cost significantly. Also, this has allowed the authors to study the stability of the system depending on the span dimension.

CONTENTS

LIST OF FIGURES

LIST OF TABLES

Abbreviations

2D two dimensional

3D three dimensional

AFC Active flow control

AOA Angle of attack

BL Boundary layer

CFD Computational Fluid Dynamics

SWJ Sweeping jet

Nomenclature

A_{Cd} Amplitude of C_d

A_{Cl} Amplitude of C_l

α Angle of attack

β Wave number $2\pi/L_z$

c Chord

d 2D drag (force per unit span length)

C_d Drag coefficient

f_0 Vortex shedding frequency

b SWJ slot thickness

$\overline{v_j}$ SWJ output velocity

l 2D lift (force per unit span length)

C_l Lift coefficient

L_z Periodicity length

$\dot{m}_j$ SWJ mass flow

C_μ Momentum coefficient of the SWJ $\frac{\dot{m}_j \overline{v_j}}{\frac{1}{2}\rho_\infty U_\infty^2 c}$

M_z Number of Fourier modes

m_z Fourier mode

p Pressure

Re Reynolds number

ρ_∞ Upstream flow density

ρ_j SWJ output density

τ_j SWJ's period of oscillation

τ Wall shear stress

θ_m Maximum angle of the SWJ

u x-component velocity

U_∞ Upstream flow velocity

v y-component velocity

ς/c x normalized by chord and rotated

C_{l_v} Viscous lift coefficient

V_N Normal velocity

V_T Tangential velocity

w z-component velocity

x_j Jet position

ACKNOWLEDGEMENTS

First, we would like to express particular appreciation to our supervisor Fernando Mellibovsky, whose guidance throughout the entire project has been essential.

Also, we thank the UPC - Universitat Politècnica de Catalunya for the academic formation last four years in the Aerospace Engineering degree, and for the provided resources which have made possible this project: from the facilities at the EETAC to the computational Cluster they put at our disposal.

Finally, we acknowledge to all our companions at the university for their support during these past five months.

INTRODUCTION

Active and passive flow control

Active flow control methods have been used during the last decade in order to improve airfoils' efficiency in high-performances-required situations, such as take-off and landing. Several studies[1,2,4,5,6] have been carried out proving that AFC with fluidic actuators improve performances in several scenarios, such as lift increase or drag reduction on airfoils and finite wings, vertical tail lift enhancement or drag reduction on trucks and cars.

AFC methods consist on any device or actuator able to control flow actively, and allow the shift and/or adjustment of it at any time. On the other hand, passive flow control describes a flow control method that cannot be switched on or off or actively modified in any way, so its effects are permanent.

Passive flow control is usually based on small changes on geometry, while active flow control consists on any device whose objective is changing flow's natural behaviour along domain. While passive flow control may be effective on certain situations, and it doesn't require a momentum injection or any power consumption, appearing as an efficient way to improve performances, AFC has been shown to be a better option in most cases due to the following reasons: its ability of changing flow's behaviour is greater, and passive control may be totally ineffective, and also AFC methods can be turned off if they are not necessary.

The boundary layer detachment

Most times, the main objective of these actuators applied to airfoils is to prevent boundary layer's early detachment, which decreases lift and increases drag. This may occur at a large AOA or in situations where a high-lift device is deployed, such as flaps. Boundary layer detachment is produced when there is a presence of an adverse pressure gradient, which forces a counter-flow near the boundary (the downstream/upstream pressure gradient dp/dx is set by the outer flow and brought unchanged across the BL). In areas of widening space, due to the mass-conservation law, the velocity decreases causing an increase of pressure by the principle of Bernoulli. (See the figure 1).

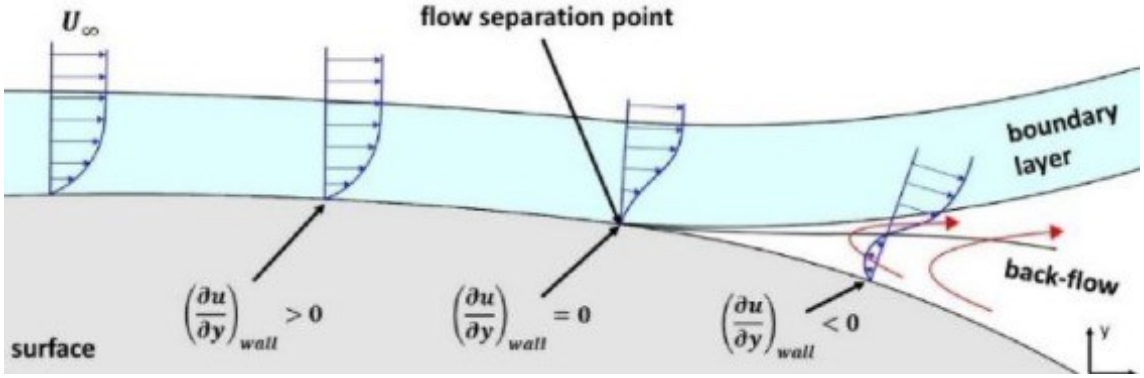

Figure 1: Graphical representation of BL's detachment[7]

The boundary layer detachment is widely studied due to the negative effects it has on the aerodynamic characteristics of airfoils, or the increase of drag on internal flows, where BL is usually detached when the section is increased. In the concrete scenario of BL detachment on the upper surface of airfoils, the recirculations downstream the separation point that are produced perform a high suction on the recirculated area, which increases the pressure (or form) drag by a simple sum of pressures. Also, the lift is affected negatively by decreasing its value, since is desirable to find high velocities in the upper surface (and then low pressures) and the detachment makes the flow decelerate upstream the separation point.

In order to prevent the separation, a non-zero-net-mass-flux momentum injection on the boundary layer upstream (or downstream) detachment is carried out most times, but zero-net-mass-flux devices such as synthetic jets have been proved to be effective too.

Fluidic actuators

The boundary layer detachment on airfoils has been studied by many authors since it represents a considerable decrease on performances, as explained earlier. Passive flow control methods have been found to be useful in this area, for example: the placing of a small wire on the surface before the detachment forces the transition of the boundary layer from laminar to turbulent, which delays the separation. Nevertheless, active flow control with fluidic actuators appears to be a more effective way to fight detachment. The possibility of injecting or subtracting fluid to the domain, or only changing its trajectory without changing the total amount of mass, is determinant to the flow's behaviour.

Fluidic actuators show a high potential to control flow and increase airfoils' performances. They are also very attractive due their reduced size. These actuators consist on any device which modifies flow through itself and makes it interact with the fluid domain.

While multiple articles[1,2] show the benefits of including fluidic actuators before a high-lift device (such as flaps), where boundary layer usually suffers a detachment, this study focuses on preventing the separation on airfoil intending to show the ability of actuators to provide a similar effect to the high-lift device inclusion without any actuator.

The aim of this project is to study the effects of a sweeping jet actuator on a NACA0012 airfoil at *ultra-low* Reynolds number, where incompressibility of the fluid is assumed. An increase of aerodynamic forces and a decrease of vorticity on the wake are expected.

Sweeping jet actuators (see the figure 2 for the conceptual design of it) have been widely studied by multiple authors[8,9]. Their design's simplicity makes SWJ a suitable option for commercial aircrafts. With a steady input of compressed air, the actuator gives an unsteady, oscillating response.

The working principle of a sweeping jet is based on the instability created inside of it. A fluid flow is produced by the "Supply" (figure 2). Any small perturbation that makes the fluid direction move laterally makes the flow go through the "Feedback path" (1) and travel backwards to meet again the principal flow. Also, in the same step, the "Interacting Region" appears by the suction of the opposite "Feedback path" (2). The appearance of flow proceeding from the Feedback path (1) makes the the principal flow displace towards the other way by simply pushing it and fills the opposite Feedback Path (2). The described process is a single oscillation of the sweeping jet actuator.

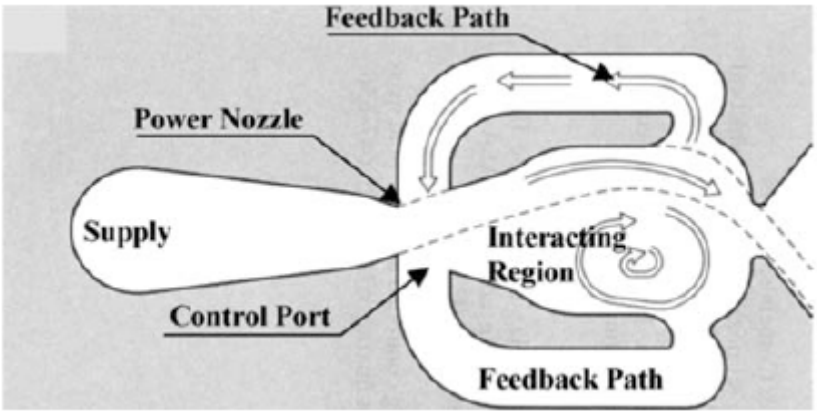

Figure 2: Conceptual design of sweeping jet actuator[10]

There is a strong relationship between actuators size and their ability to control flow.[1] It was found that sweeping jet actuators could control flow up to Mach number 0.1 at a Reynolds number up to 10^6 but jet exited nozzle at sonic conditions, so larger nozzles where needed to keep the momentum coefficient constant and reduce the jet's speed. The scenario was a NACA0012 with a deployed flap at 30^o where the boundary layer detached, and several sweeping-jets were installed before the flap, achieving a significant increase of C_l by preventing boundary layer detachment.

Sweeping-jets have been found to be effective too in scenarios with a strong pressure gradient, such as a ramp.[5] In this case, the boundary layer detached without any actuator when laminar flow arrived to a 20^o ramp. This study encouraged the idea of applying a sweeping jet on a simple airfoil because sweeping jets were found to be effective on a model with no mobile parts.

Finally, Woszildo[11] experimentally studied the effect of the inclusion of a SWJ on an airfoil. The study concluded explaining how and which parameters of a SWJ governed flow separation on an airfoil based on experimental results, concluding that the momentum coefficient had a strong relation with flow separation being the primary parameter, while the jet's deflection angle had a second order effect. Also, the jet's location has a strong effect on the flow's behaviour. The conclusions of this paper will be a guide for this project, which takes them into account when deciding how and which parameters modify.

To perform the study, numerical simulation is employed. Computational Fluid Dynamics softwares provide the ability of studying the behaviour of the fluid —and not just the final effect on the airfoil— all along the domain without the need of complex and expensive hardware. For the purpose of this project, it is essential to perfectly know flow's trajectory over the airfoil, since its modification is the primary objective of this project.

As one key point of this project is to determine the effect of the actuator on boundary layer by introducing a frequency (or just injecting a momentum) on the fluid domain, a turbulence-model-based CFD would be useless for the study, since it is desired to understand the interaction of a time-dependent jet with the two dimensional boundary layer that develops at laminar to transitional Reynolds number. In fact, the location, size and frequency of the turbulences will be studied along the project. Therefore, the selected sofware is Nektar++: a Spectral-hp element framework whose characteristics will be explained later.

CHAPTER 1. METHODOLOGY

1.1. Theoretical Background

1.1.1. Navier-Stokes equations approach

First and foremost, it is essential for this work to know that the fundamental equations are based on Navier-Stokes equations. Found and discovered by two physicists, Claude-Louis Navier and George Gabriel Stokes, in between 1827-1845, are a set of partial derived non-linear equations which describe the movement of a fluid. In general terms, those equations apply over terrestrial atmosphere, ocean currents, and doubtless for our concern, the flow around vehicles , projectiles and any of the phenomena that occur among almost any Newtonian fluids. Those equations have no analytic solution due to its complexity, in fact, it is one of the big non-solved problems in maths history. Consequently, for being able to solve any problem containing those, numerical methods have to be used.

Luckily, to compute and simulate, Nektar++ software has been used to achieve so. In this program, which is a little bit more conducted beneath, there are several solvers depending upon the type of simulation that wants to be undertaken. Nonetheless, for the develop of active flow control sweeping jet, the *IncompressibleFlowSolver* was used.

This solver makes some assumptions about the fluid properties and fits with the real conditions of the studied system.

1. Newtonian fluid: defined as any fluid whose viscosity is independent on the shear stresses that receives or the temperature. The viscosity is considered to be constant.
2. Incompressible: the density of the fluid is constant, which means that a differential of volume always contains the same differential of mass. This is assumable at low Reynolds regime. $\nabla \cdot u = 0$
3. Negligible thermal effects: the heat conduction between the walls and the fluid is not considered, and also the changes in the fluid temperature.
4. Bi-dimensional: on the most part of the study, the flow is considered to be *2D* and the fluid domain also.
5. No turbulence modelling: as explained in the introduction, the turbulence of the fluid is not modelled with well-known models such as Spalart-Allmaras, $K-\omega$, $K-\varepsilon$...
6. Gravity acceleration is neglected, and any other external forces such as electromagnetic force or inertial accelerations. $f = 0$

Then, the equations that govern the fluid are the following:

$$\frac{\partial u}{\partial t} + u \cdot \nabla u = -\nabla p + v\nabla^2 u + f \tag{1.1}$$

$$\nabla \cdot u = 0 \qquad\qquad f = 0 \tag{1.2}$$

where V is the velocity, p is the specific pressure (including density) and v the kinematic viscosity.

1.1.2. Boundary conditions

Once the fluid domain properties have been defined, is mandatory to present the boundary conditions of the problem. The used software Nektar++ includes several built-in options to define fluid's restrictions on the domain. The regions where there must be boundary conditions (boundary regions) are enumerated below, and their conditions are exposed:

1. **Inlet**: The x-component velocity u is set to the U_∞ value. The value imposed to u is 1. The international system is not used since there is no need to. The upstream velocity is set to 1, and the chord is also 1. Then, the time unit is defined as the time needed for a fluid particle to travel along the chord. Also, taking into account that the density is set to 1, the viscosity of the fluid is simply $\nu = 1/Re$. Finally, the lift and drag coefficients:
$$l = \frac{1}{2}\rho c U_\infty^2 C_l = \frac{1}{2}C_l \rightarrow C_l = 2l \tag{1.3}$$
$$d = \frac{1}{2}\rho c U_\infty^2 C_d = \frac{1}{2}C_d \rightarrow C_d = 2d \tag{1.4}$$

2. **Outlet**: Here, the Outflow Boundary Conditions are applied proposed by Nektar++ are applied. The most straightforward outflow condition is to specify fully developed conditions of $\nabla u^{n+1} \cdot n = 0$ and $p = 0$. However, when energetic vortices pass through an outflow region one can experience instabilities. This was studied by Dong, et al[17] , and in order to mitigate the instabilities it was suggested to impose a pressure Dirichlet outflow condition of the form
$$p^{n+1} = \nu \nabla u^{*,n+1} \cdot n - \frac{1}{2}|u^{*,n+1}| S_o (n \cdot u^{*,n+1}) + f_b^{n+1} \cdot n \tag{1.5}$$
And for the velocity:
$$\nabla u^{n+1} \cdot n = \frac{1}{\nu}[p^{n+1} n + \frac{1}{2}|u^{*,n+1}|^2 S_o (n \cdot u^{*,n+1}) - \nu(\nabla u^{*,n+1}) n] \tag{1.6}$$
This condition is specified on Nektar++ by using the USERDEFINEDTYPE tag: VAR="u" USERDEFINEDTYPE="HOutflow" VALUE="0".

3. **Upper and lower boundaries**: For these boundaries, the y-component velocity v has been set to zero, so there is no mass flux exchange with the non-controlled domain.

4. **Airfoil surface**: the no-slip condition has been applied. Since the airfoil is a solid wall and the fluid is considered viscous, the velocity of the fluid on the nearest points of the domain to the airfoil has been set to zero ($u = 0, v = 0$).Also, for this type of boundary conditions, Nektar++ recommends to set the conditions for the pressure and the velocity separately, as a conclusion of the work of Karniadakis, et al[16] , where the boundary condition for the pressure was defined by the equation 1.7. This is applied by defining pressure by: VAR="p" USERDEFINEDTYPE="H" VALUE="0"

on Nektar++ and there is no need to introduce the mentioned parameterization in the code.

$$\frac{\partial p^{n+1}}{\partial n} = -[\frac{\partial u^{n+1}}{\partial t} - \nu(\nabla \times \nabla \times u)^{*,n+1} + N^{*,n+1}] \cdot n \tag{1.7}$$

The following sketch shown in Figure 1.1 contains the initial approach of the study. The airfoil is oversized in order to have an insight of the whole control volume of the problem.

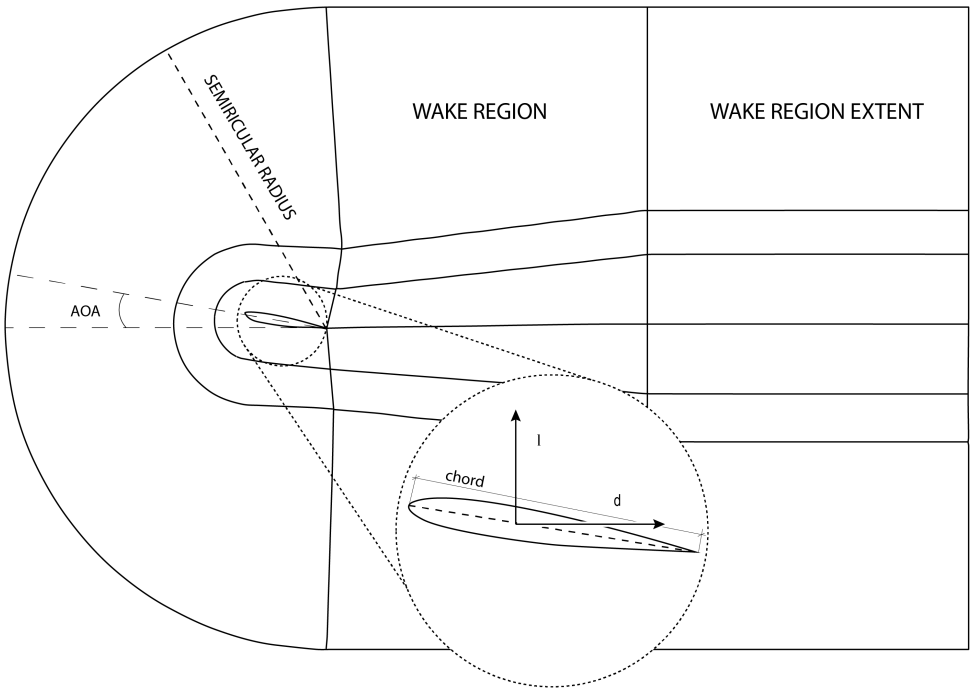

Figure 1.1: Sketch of the airfoil and the mesh

1.2. Spectral methods

Spectral methods[3] are a class of techniques used in applied mathematics and scientific computing to numerically solve certain differential equations, potentially involving the use of the high-order polynomials of Fourier series. The idea is to write the solution of the differential equation as a sum of certain ”basis functions” and then to choose the coefficients in the sum in order to satisfy the differential equation as well as possible.

Under lucky circumstances, spectral methods deliver a degree of accuracy that local methods cannot reach. For large-scale computations, this higher accuracy may be most important for permitting a coarser mesh, thus a smaller number of data values to store and operate with. Nowadays, within some branches of scientific world this method is considered a worthy contender among the better established finite difference and finite element methods. Nonetheless, they are still less well understood.

1.3. Finite element method

Finite element method also known as FEM, it's a numerical technique used to perform finite element analysis (FEA) of any given physical phenomenon. It was not until recently that this method has started to blip on the radar due to the increase in computer performances.

The principles of this method are to design a mesh that adopts the shape of the element of study. The structure of the mesh holds different geometrical shapes depending on the object, it can be one-dimensional rode, two-dimensional triangles or quadrilaterals, squared. Each of the dots that define these geometrical elements are called nodes and they are in charge of solving the numerical value all over the mesh. Most of these processes are described using partial differential equations (PDEs) which have been implemented in computers over the last decades and that's the reason why it can be said this method is in it's early beginnings.

At the end, each geometrical region it's a matrix of nodes that actually share some of them with the neighbour region. The combination of all of them give the final mesh result. Obviously, the accuracy of the calculation depends on the quantity of elements that are introduced in the mesh. The more elements there are, the smaller each one will be and the more accurate the results. Sadly, more elements also mean more computational time, for economy reasons therefore, the aim is to find a happy medium to balance the minimum elements to get the most accurate result for our problem.

There are several types of Finite Element Methods. In the case of the study Nektar (which is explained below) uses hp-FEM type. This class of FEM, is based on piecewise-polynomial approximations that employs elements of variable size, h and polynomial degree, p. One of the reasons for which this method is more appealing inside FEM is it's ability to converge exponentially in contrast to other FEM types that do it with an algebraic rate.

However, in the case of this study, what it can be found is an hybrid type of solver between Spectral and h type solver.

1.3.1. Spectral/hp method

The spectral/hp element method[19] combines the geometric flexibility of classical h-type finite element techniques with the desirable resolution properties of spectral methods. In this approach a polynomial expansion of order P is applied to every elemental domain of a coarse finite element type mesh. These techniques have been applied in many fundamental studies of fluid mechanics[12] and more recently have gained greater popularity in the modelling of wave-based phenomena such as computational electromagnetics[13] and shallow water problems[14] - particularly when applied within a Discontinuous Galerkin formulation.

In other words, even though both methods are rather similar, the main difference between these two is that spectral methods use basis functions that are different of zero all over the domain. On the other hand, FEM use basis functions nonzero but only on small subdomains. All in all, whilst finite element method uses a local approach, spectral methods use a global approach. The merge of these two lead to a great combination with their exponential convergence (for smooth transitions of the mesh, which is something that needs

to be stress about the mesh generation) and the good error properties of the spectral methods.

1.4. Gmsh

Gmsh[20] is an open-source 3D finite element mesh generator with a built-in CAD engine and post-processor. Gmsh is built around four modules: geometry, mesh, solver and post-processing. The specification of any input to these modules is done either interactively using the graphical user interface, in ASCII text files using Gmsh's own scripting language (.geo files), or using the C++, C, Python or Julia API.

Gmsh provide the following features to their users:

1. Quickly describe simple and/or "repetitive" geometries, thanks to user-defined macros, loops, conditionals. Defined in a simple text file that has been actually modified along the simulations depending on the geometry variations. It can be actually modified within any text file editor.

2. Parameterize these geometries. It is specially good Gmsh at this characteristic as it's capable of converting the text files into a structured 2D mesh exactly the same as the case of this study.

3. Generate 1D, 2D and 3D simplicial (i.e., using line segments, triangles and tetrahedrals) finite element meshes for CAD models in their native format. Filling out part of the previous statement, Gmsh can work either in 1D, 2D or 3D creating finite element mesh.

4. Specify target element sizes accurately. Gmsh provides several mechanisms to control the size of the elements in the final mesh: through interpolation from sizes specified at geometry points or using flexible mesh size fields.

5. Interact with external solvers through. This is exactly one of the remarkable features of interest as Nektar is the actual external solver that solves the Incompressible Navier Stokes equations.

These are some of the most noteworthy features of Gmsh that have been used while using it. One of the aforementioned is the structured mesh which is the case of our mesh.

Unstructured meshes are widely used in CFD world nowadays due to the fact that they adapt to complex geometries. Structured meshes are harder to handle when comes to geometry complexity. However Structured meshes have some advantages with respect to unstructured that bring higher possibilities to our problem.

- Higher degree of quality and control. Taking a longer time to build the structured mesh maybe saves some time afterwards. This is simply because structured meshes are scripted in such a way that become automatic so that you have whole control over it. It typically allows more control of interior node locations and sizes as interior node placement is directly linked to the user-defined exterior nodes.

- Better convergence. Usually structured grids are aligned in the flow direction leading to more accurate results and convergence of them in solvers like Nektar++.
- Storage and computation. Structured mesh solvers have a well-defined path of calculation unlike unstructured mesh that it's more flexible but requires of higher bandwith and cache to store for each node the values.

1.5. Nektar++

Nektar++[18] is a spectral/hp element framework designed to support the construction of efficient high-performance scalable solvers for a wide range of partial differential equations. Software is released as open-source under the MIT license. Although primarily driven by application-based research, it has been designed as a platform to support the development of novel numerical techniques in the area of high-order finite element methods.

Nektar is the core engine of this study as it is the one in charge of simulating the air behaviour around the airfoil with some inputs such as the conditions over the control volume or the meshed geometry of the profile.

As the air is consider to be incompressible, IncompressibleFlowSolver has been used along the whole research. As aforementioned, Nektar engine works by spectral methods, which are computationally less expensive than finite element methods, but become less accurate for problems with complex geometries and discontinuous coefficients.

In the case of NACA0012, it has no problem in order to compute an utter simulation as it is not a complex geometry. However, by using this method it certainly takes a longer time to conclude the simulation compared to other software such as the famous and well-known Ansys, which doesn't solve the turbulence itself but models it with some methods.

From all the solvers that Nektar++ facilitates to their customers it is of great importance to stress Fieldconvert and IncompressibleFlowSolver of Navier Stokes as the ones used. FieldConvert helps to prepare the file from .msh to xml.

1.6. Clufa UPC

Time of simulations is long enough to wait for results, therefore, UPC EETAC Cluster Clufa was used. It is basically a virtual computational cluster with several online nodes that can be accessed from everywhere as long as there is an internet connection spot. This virtual cluster consist of the following features:

1. Cluster EETAC-HA with 4 servers with a total of 32 cores and 208 Gb of RAM
2. Cluster CBL-HA with 3 servers with a total of 44 cores and 224 Gb of RAM

This powerful computational cluster is very useful not only due to its constant pace of work with the submitted jobs , but its capability to have several jobs running at the same time.

Another remarkable feature is that the computation results and simulations stay within this virtual machine, so, for the team work, it is very easy to access wherever you are.

Clufa has been if not the main, one of the most important computational sources together with Nektar to inquire the overall questions that made this study possible so we gratefully acknowledge EETAC for sharing their servers.

1.7. Post-processing

Once the simulations have arrived to their end, it is time to post-process the results with all the files that Nektar provides, such as fld and chk. Sometimes these simulations had been downloaded and checked to make sure they were running properly and had no issues, using the extra tool xmgrace for quick monitoring partial time series.

1.7.1. ParaView

ParaView is an open-source software, multi-platform data analysis and visualization application. It is widely used in either scientific and engineer communities to display some relevant data about any simulation it is being carried out. As soon as the software is launched, it can be seen all the options and possibilities it has. In the case of this paper in particularly, it has been mainly used to represent how fluid behaved over the NACA0012 airfoil with the three different cases described in the upcoming chapters.

Anyway, in order to have first insight, the interesting features for this study were to be able to display global and decomposed speeds (controlled by surface module in the left-handed side of the software), the actual position of BL detachment (by using wall shear stress from Nektar++ computations) and eventually, the streamlines of the air passing throughout the airfoil.

1.7.2. Matlab

Matlab is not one of the softwares which are used to compute any of the simulations but it is very handy in order to represent, obtain and retrieve all the information from Nektar. Basically, the values coming from each simulation sample need to be managed and organized to see how the simulation evolves over time in a quantitative form. Although displaying the movie of the airfoil along time in the ParaView viewer can give a consistent trail of what is happening, results and conclusion must be based upon values. Thus, several scripts have been written for each of the sections of the whole study, from the plots distributed along the report until the values of the tables or extra computations.

1.8. NACA0012 Mesh

Before stepping into the mesh study and modifications, it is good to know from where the work starts. The original mesh is shown in the figure 1.2. It is clearly divided in three big sections plus subdivisions.

Beginning from the farthest section with respect to the airfoil to the closest one:

1. Semi-circular region
   (a) Far field (represented in green color)
   (b) Mid field (represented in pink color)
   (c) Near field (represented in blue)
2. Wake region
3. Extended wake region

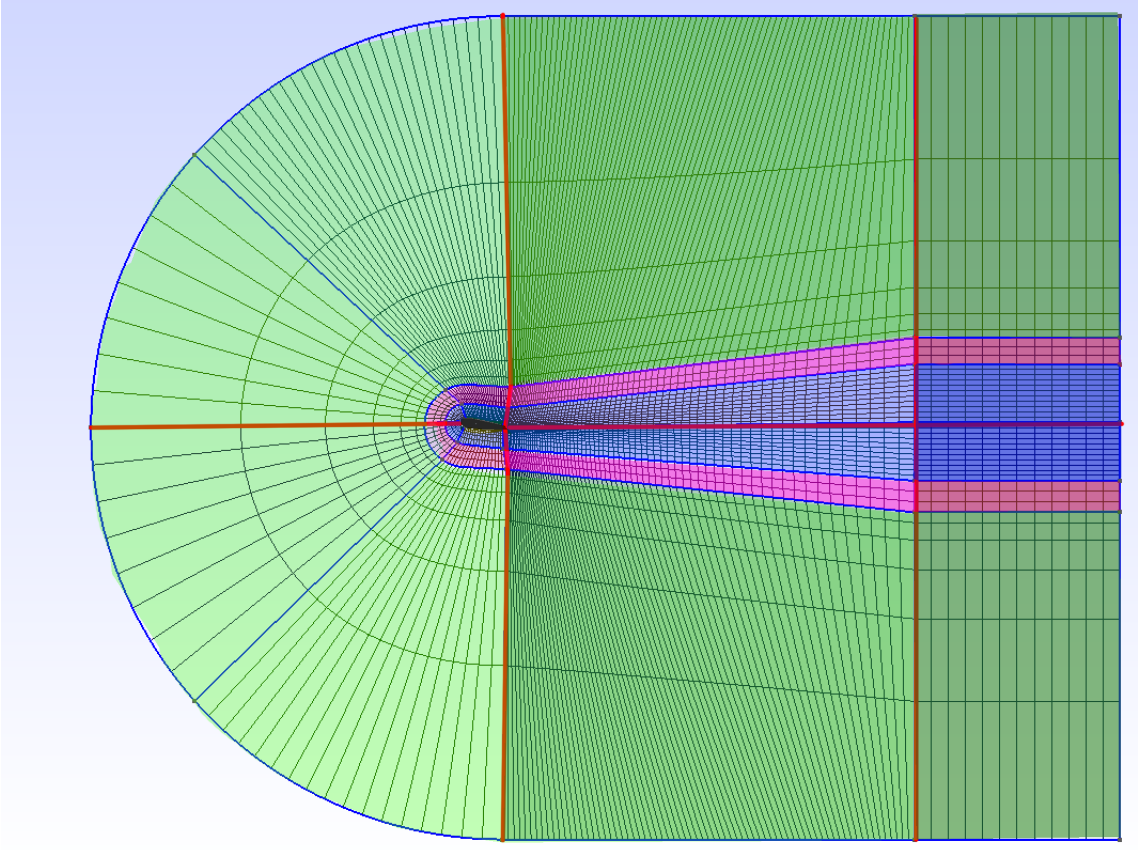

Figure 1.2: Full mesh and NACA0012 airfoil

Along the mesh and divided by vertical red lines, there are the three sections that range from a weaker to a darker green, being the inlet the first one, the wake the second one and fringe region the last one respectively.

Each section is divided in such a way to develop its function. For instance, the inlet is the first stage where airfoil interacts with air.

It splits in the leading edge towards upper and lower surfaces, lying flush against the airfoil in order to meet again afterwards in the trailing edge.

Second stage is the wake section. This is where flow around airfoil reunites in the trailing edge. On account of this air split and as consequence of generating some lift, there is some pressure difference which creates an oscillating wake behind.

Finally, the third stage. This is a purely section to see whether the stabilization of the wake improves in the simulations.

What is important to point out about the subdivisions is the capability of having control on element sizing. The airfoil that can hardly be seen, it's right between the semi-circular region and the wake region. The part of the mesh that is wrapping up the airfoil in blue color is the part with higher mesh density. Then there is the pink region that still has high density and, eventually, the green region that reduces rather a lot the density of the mesh compared to the blue one. All in all, the mesh density between near and mid field are the ones that should be more treated and observe as they bring the most valuable information.

In the figure 1.3 there is a zoomed figure of the initial mesh without any colouring:

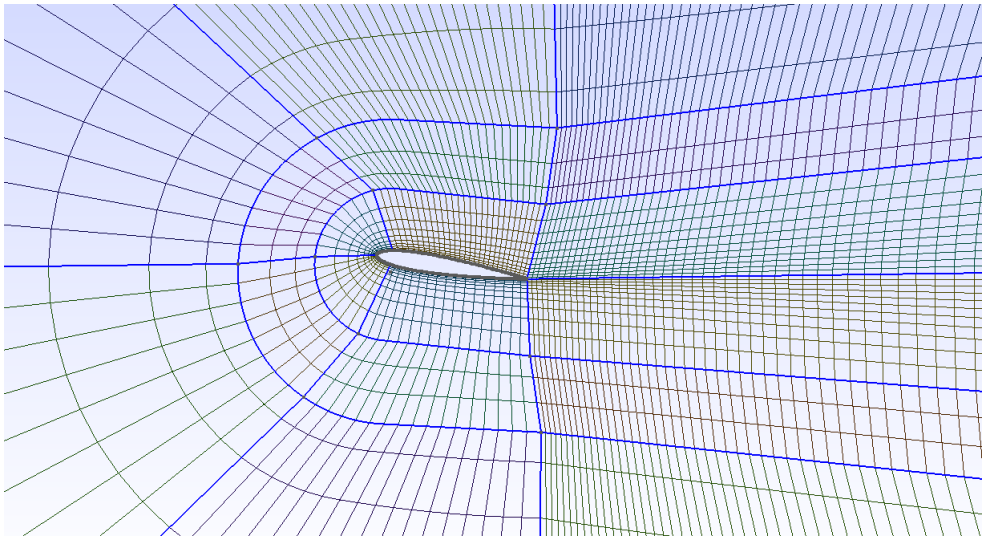

Figure 1.3: Zoom of NACA0012 airfoil

1.9. Mesh density convergence study

Before any problem could arise at the time of computing the aerodynamics of the wing, it was a sure thing that a mesh study had to be carried out. For this purpose, a NACA0012 template code provided by the teach was used and some major changes where made to arrange the excess lines.

This mesh study was conducted for two main-connected reasons:

1. On the one hand, it is useless to have a very tinny and narrow mesh between its points if the obtained result with higher-spaced mesh were nearly the same. It would only carry higher load to the CPU for no reason.

2. On the other hand, and as said before, it is obvious that the higher the number of mesh dots of calculation, the higher the time to obtain the results.

Thus, with that said, a guide with several steps was followed to determine the better mesh for the study. Those steps of increasing and decreasing are summarized below in the sequence of performed:

1. Control volume convergence study
2. Change of points along surface
3. Polynomial expansion dependence study
4. Time resolution dependence study

1.9.1. Control volume convergence study

NACA0012 airfoil has been programmed in such a way that by changing some of the inputs, the mesh and airfoil automatically adjusts. Thus by gathering the aforementioned statement about saving time plus understanding how the code is made, first step is to vary control volume according to its ratios in order to keep an structured mesh.

In the figure 1.4 it can be seen the difference in size of the control volume. From the first one with a size which is 5 times the chord value of the airfoil until the last picture with a control volume 16 times the chord size. The airfoil stays the same while the whole size

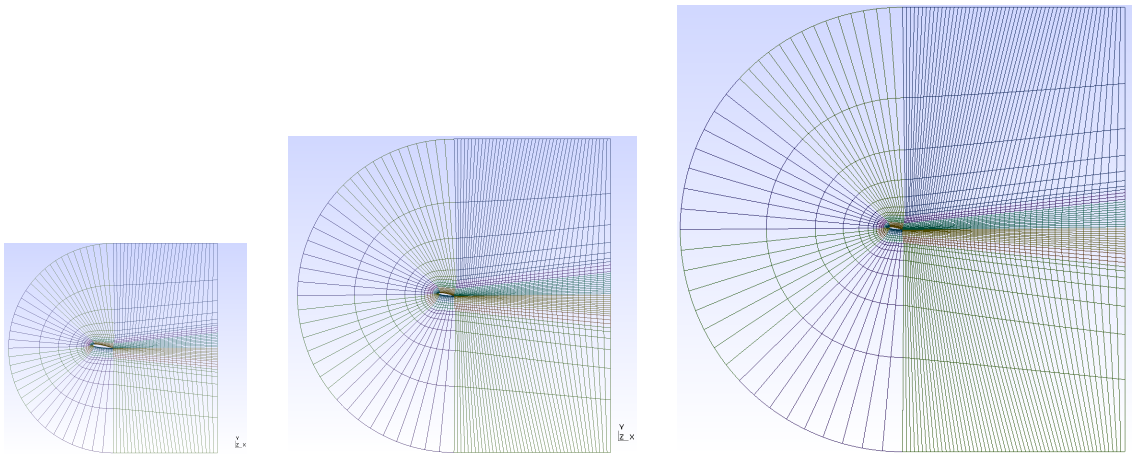

(a) With control volume $5 \cdot c$ (b) With control volume $10 \cdot c$ (c) With control volume $16 \cdot c$

Figure 1.4: Different radius in control volume variation

of the mesh varies according to the introduced number. Although the final results will be placed in a table at the end of this section, the values used have been:

1. Radius 5 times chord
2. Radius 8 times chord
3. Radius 10 times chord
4. Radius 12 times chord
5. Radius 14 times chord
6. Radius 16 times chord

Results are tight but as it was discussed above, the bigger the mesh is, the longer it takes to run the job and obtain any solution. The following table contains a brief summary of hours of simulations: Where CV size is as stated above, how many times bigger is the mesh

$CV\ \ size$	$C_l\ \ Mean$	$\varepsilon_{C_l}\ \ \%$	f_0	$\varepsilon_{f_0}\ \ \%$	A	$\varepsilon_A\ \ \%$
5·c	0.3773	0.85%	0.9009	1.26%	0.004858	3.48%
8·c	0.3749	0.20%	0.8945	0.53%	0.004974	1.18%
10·c	0.3743	0.07%	0.8913	0.17%	0.005012	0.43%
12·c	0.3741	000%	0.8898	0.00%	0.005033	0.00%

Table 1.1: Results of mesh size

with respect to the chord of the airfoil. The output of the *.fld file* that Nektar provides is a temporal signal (shown in the figure 1.5) with its respective frequency f_0 and its amplitude A (difference between the mean value and the peak). C_l Mean is the mean value obtained from the files of the simulation corresponding to the lift coefficient and finally $\varepsilon_{C_l}\ \ \%$ and $\varepsilon_A\ \ \%$ are the relative errors express in % of the lift coefficient and amplitude respectively. All of the relative errors are calculated according to to the best considered mesh due to its values, $12 \cdot c$.

The chosen mesh is the one containing $10 \cdot c$ because it's nearly as good as the best considered which is $12 \cdot c$ but reducing useless extra time or unnecessary extra mesh without compromising the values.

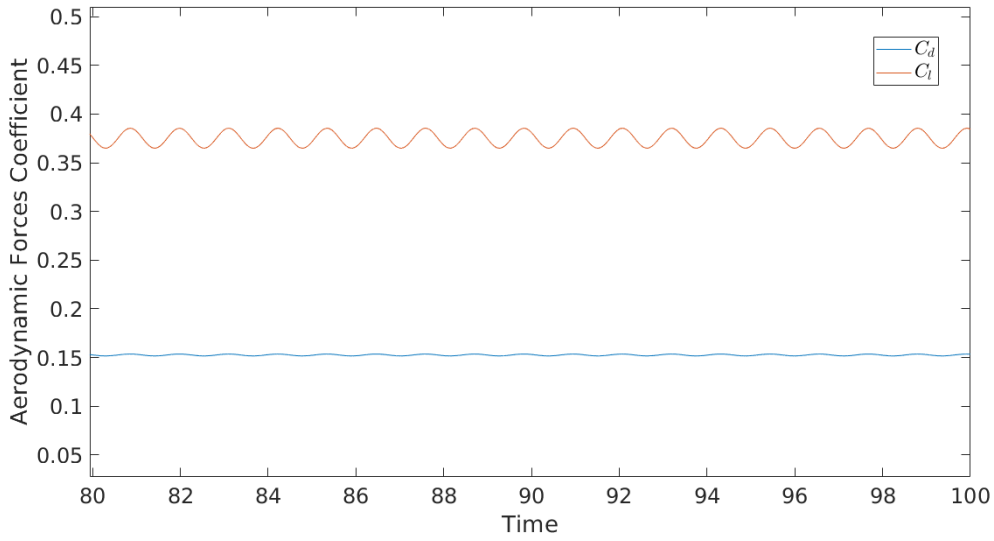

Figure 1.5: Example of output signal of the mesh study for $10 \cdot c$

1.9.1.1. Extended wake inclusion

Extended wake region (or also known as fringe region) is an added part of the mesh, rearward of the airfoil. The interest of this area is to move the outflow boundary condition as far downstream from the region of interest (airfoil) as required to avoid having a significant

impact on the accuracy of the computation. This section has been also complimenting the volume of the mesh to find the best combination among the attempts. Fringe region can already be seen in Figure 1.2 although it hasn't been used for all the mesh computations.

Next table is considering extended wake section, there are two tested sizes. It was not increased more as dimensions were already big enough and results started to stagnate:

$CV\ \ size$	Fringe r.	$C_l\ \ Mean$	$\varepsilon_{C_l}\ \%$	f_0	$\varepsilon_{f_0}\ \%$	A	$\varepsilon_A\ \%$
8·c	5·c	0.3758	0.38%	0.8928	0.36%	0.0051	1.18%
8·c	10·c	0.3759	0.42%	0.89448	0.54%	0.0051	0.97%
10·c	5·c	0.3751	0.19%	0.8913	0.18%	0.0051	0.84%
10·c	10·c	0.3752	0.22%	0.8928	0.36%	0.0051	0.61%
12·c	10·c	0.3748	0.12%	0.8913	0.18%	0.00514	0.26%
14·c	10·c	0.3745	0.05%	0.8894	0.04%	0.0051	0.09%
16·c	10·c	0.3744	0.00%	0.8897	0.00%	0.0051	0.00%

Table 1.2: Results mesh with extended wake added

All the indicated variables are the same as the previous table except the fringe r. which is the reward added region. Also, as now the study domain has increased with the extended wake, the calculus are referenced to the $16 \cdot c$ simulation with fringe r. of $10 \cdot c$.

1.9.2. Chord-wise resolution study

In second place, a variation in points was also necessary because most of the code is written related to them. The more the points are introduced, more definition of the airfoil, therefore, the rest of the mesh should be even more structured. The figure 1.6 shows it.

In this case, the challenge was to fill the airfoil with the lowest possible amount of points without affecting the correct develop of the problem. After several attempts and simulations, the two more attractive values for either the upper and lower surface where the following:

- Upper surface 15, lower surface 10
- Upper surface 24, lower surface 16

These values have been tested and combined among the previous results of the control volume to find out whether it could bring some differences and unforeseen results or nothing at all. The table 1.3 shows the final values.

$CV\ \ size$	Fringe r.	$C_l\ \ Mean$	$\varepsilon_{C_l}\ \%$	f_0	$\varepsilon_{f_0}\ \%$	A	$\varepsilon_A\ \%$
8·c	10·c	0.3760	0.03%	0.8928	0.18%	0.0051	0.28%
10·c	10·c	0.3753	0.04%	0.8917	0.13%	0.00511	0.30%
12·c	10·c	0.3749	0.03%	0.8913	0.00%	0.0051	0.20%

Table 1.3: Results mesh with points variation along surface

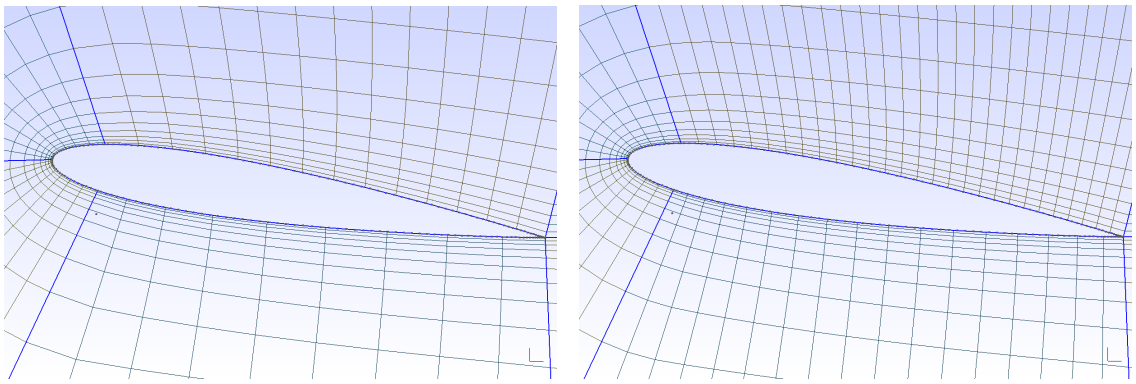

(a) NACA0012 with 15 points over surface and 10 in the lower surface

(b) naca0012 with 24 points over surface and 16 in the lower surface

Figure 1.6: Different radius in control volume variation

1.9.3. Polynomial expansion dependence study

Switching to the conditions file, there is a section inside that fills each generated cell of the mesh with even more lines in either vertical and horizontal directions. Nodes of computation will increase to a greater extent, depending on the introduced number for each zone that was described in this chapter above. In our case, the following polynomial expansions where tried:

1. Far-Field (FF)
2. Upper-Mid Field Wake (UMFW)
3. Mid-Field Except Upper-Wake (MFEUW)
4. Upper-Near Field (UNF)
5. Lower-Near Field (LNF)
6. Wake (W)

Each of these parts of the mesh are composites and are defined individually in order to have more control over them. In fact, as it goes along, new composites are defined according to the new surfaces resulting from the jet incorporation.

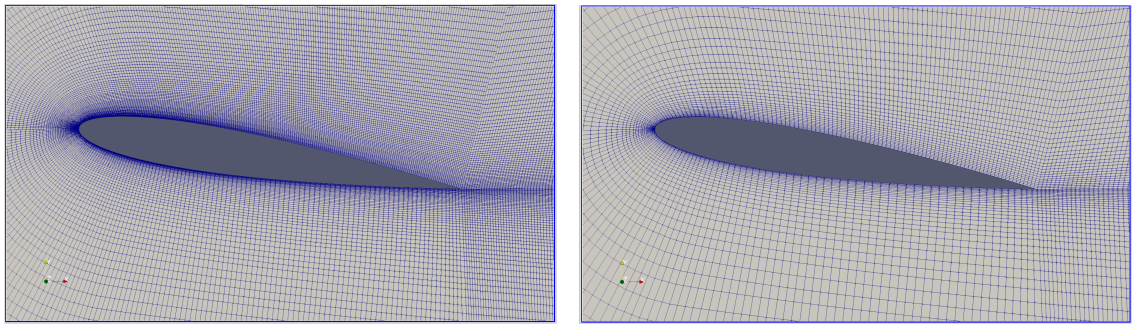

(a) High meshed example of expansions

(b) Lower meshed example of expansions

Figure 1.7: Difference between the expansions

The figure 1.7 show the previous and the subsequent, after passing through the expansions. As it can be clearly seen, all the squares of the mesh have been multiplied as many times as the number introduced for each specific case.

Switching to a numerical summary, and keeping the previous chapter results, the mesh used has been the one with 10 times the chord either in fringe region and mesh size. The forthcoming table retrieves the sixth defined zones in the numerated list above with the respective tested values for each one. The rest of the parameters are likewise used as the ones of the sections 1.9.1. and 1.9.2..

FF	*UMFW*	*MFEUW*	*UNF*	*LNF*	*W*	C_l *Mean*	ε_{C_l} %	f_0	ε_{f_0} %	A	ε_A %
3	3	3	6	4	4	0.3724	0.73%	0.8881	0.53%	0.0048	5.14%
4	5	4	6	4	4	0.3725	0.73%	0.8881	0.53%	0.0048	4.99%
3	4	4	6	5	5	0.3740	0.32%	0.8913	0.18%	0.0049	2.56%
4	4	4	6	6	6	0.3748	0.11%	0.8913	0.18%	0.0051	0.83%
4	5	5	7	6	6	0.3747	0.13%	0.8913	0.18%	0.0051	0.94%

Table 1.4: Results of expansions dependence

1.9.4. Time resolution dependence study

Last parameter that was suppose to alter or vary mesh convergence was the time step. The Time Step is the difference in time between two consecutive iterations: in the time-discretisation, it's the differential of time applied.

The main two reasons for which time step is important to our simulations are the following:

- Larger time steps introduce inaccuracies, exactly as it happens with space discretisation, time is continuous and the discretisation of the time derivative term only tends to be exact if when the time step tends to zero.
- Numerical methods can be unstable and this is the case of time discretisation when the time step is not taken small enough for methods that are only conditionally stable.

	CV size	Fringe r.	C_l *Mean*	ε_{C_l} %	f_0	ε_{f_0} %	A	ε_A %
ts=0.001	10·c	10·c	0.3758	0.15%	0.8929	0.00%	0.0051	0.35%
ts=0.0005	10·c	10·c	0.3755	0.07%	0.8928	0.00%	0.0051	0.26%

Table 1.5: Results of time resolution dependence

CHAPTER 2. RESULTS AND DISCUSSION

2.1. Baseline

This section's aim is to determine the natural flow behaviour around a NACA0012 airfoil at Re=1000 and AOA=9^o. It's very important to precisely analyze the flow's behaviour in order to compare the future actuated simulations with this ones. The expectations are to find a massively detached boundary layer, and then a low C_l and big C_d, driving into low aerodynamic efficiency. Concretely, this section focuses on finding:

- Flow's topology
- The boundary layer's detachment position over the airfoil's upper surface
- The vortex-shedding frequency (if it exists).
- The airfoil's performances in terms of global quantities such as the aerodynamic characteristics of the airfoil at the studied Reynolds without activating the sweeping jet.

These parameters will be the reference in order to place the jet and to determine its frequency.

Post-processing results with Paraview and Matlab show that at Re=1000 and with an angle of attack of 9^o, the boundary layer detaches at the 34% of the chord (figure 2.1, wall shear stress over ς/c: x normalized by chord and rotated) approximately, where the wall shear stress τ on the upper surface is cancelled.

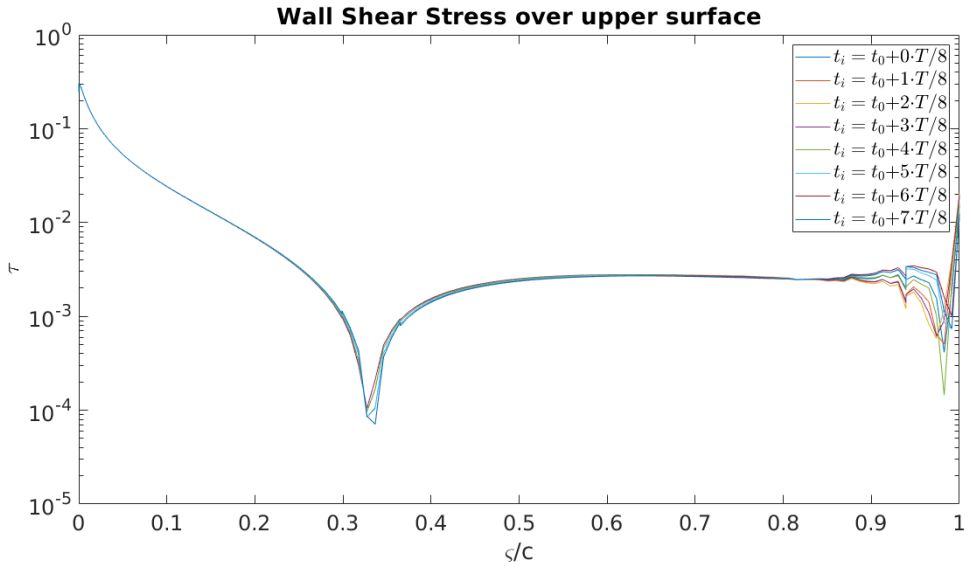

Figure 2.1: Wall shear stress along chord

Several time instants have been selected to compute the shear stress over the upper surface. As it is explained in the following paragraphs, the signal is not stationary and

the time-series of the aerodynamic characteristics is oscillatory with a certain frequency. Then, a cycle has been selected and subdivided into eight equal parts, where the shear stress has been computed. $t_i = t_0 + k \cdot T/n$, with $k = 0, 1, 2, ..., n-1$ being T the period and n the number of subdivisions.

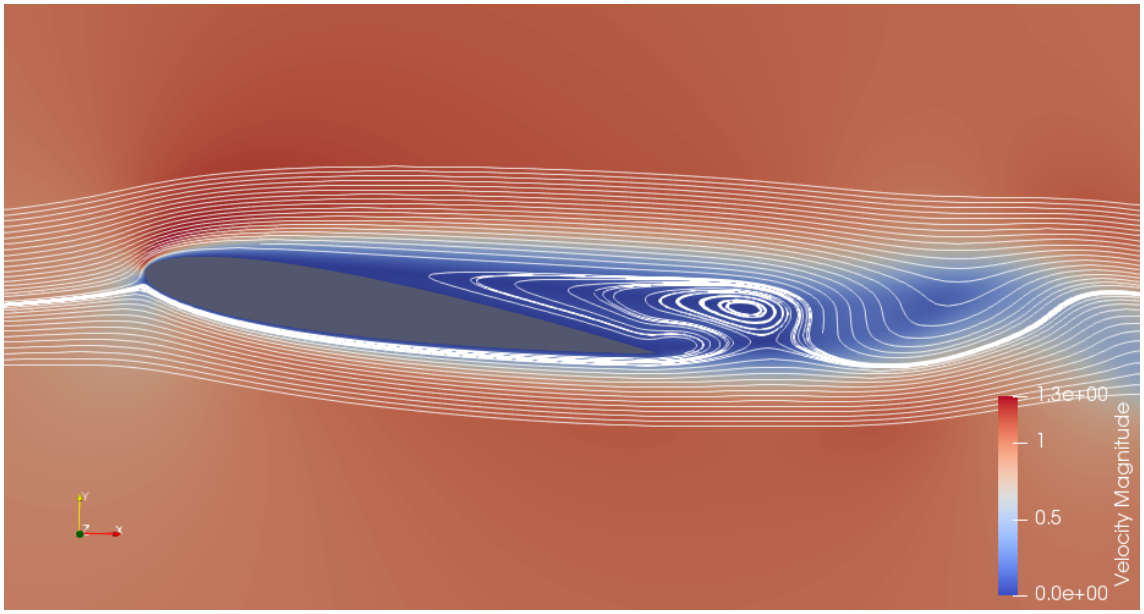

Figure 2.2: Streamlines and Velocity contour

The figure 2.2 shows the big recirculations produced downstream the separation point. Notice that the contour plots the absolute velocity magnitude, which is lower on the upper surface than in the lower surface excepting very near the leading edge. This is causing very low performances of the airfoil by the decrease of lift and increase of drag.

In order to determine the vortex shedding frequency, a Fourier transform is applied to the lift signal. The first peak corresponds to the dominant frequency of the system (due to the vortex shedding) and also the 0 frequency value gives the mean of the signal. From this data the average C_l and C_d can be extracted (by Fourier transforming each signal) and also the vortex shedding frequency. First, the transient part of the signal must be deleted in order to obtain more reliable results, and finally an integer number of cycles is selected from the signal. This is not required to perform the Fourier transform, but is very advisable in order to get better accuracy for relatively short time series.

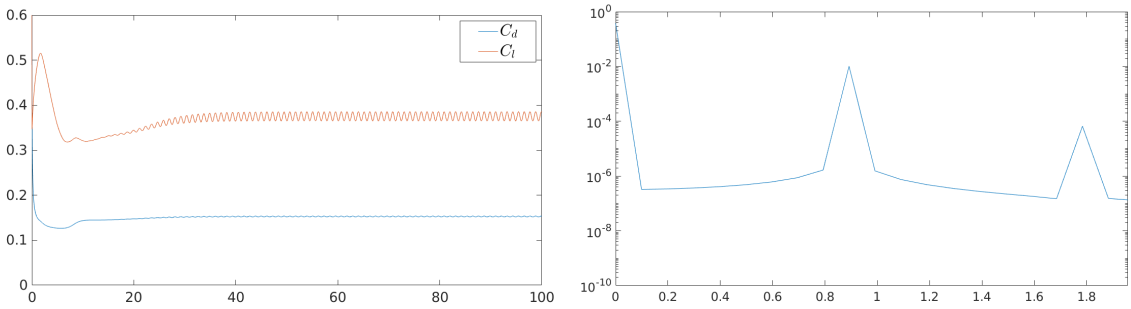

(a) Time-series of forces coefficient(lift and drag)

(b) Frequency signal (lift coefficient)

Figure 2.3: Lift and drag signals

Figure 2.3 shows the lift and drag signals analyzed both in time and frequency domains. The temporal signal shows that the response stabilizes at approximately 50 time units, which is useful to know in order to analyze the signal in frequency, and also for future calculations. Also, the first peak in frequency corresponds to the vortex shedding frequency. This will be used in future calculations.

f_0 [U/L]	0.892
Stabilization time [L/U]	50
C_l	0.3752
C_{lp}	0.3725
C_{lv}	0.0028
C_d	0.1527
C_{dp}	0.0774
C_{dv}	0.0753
A_{Cl}	$5.110 \cdot 10^{-3}$
A_{Cd}	$4.828 \cdot 10^{-4}$

Table 2.1: Baseline results

The signals shown in the figure 2.3(a) has been analyzed and by the Fourier transform the values shown in the table 2.1 have been extracted.

The figure 2.4 shows a vorticity contour in the near-wake. The distance between vortices is roughly U_∞ / f_0, which is an indication that vortices are advected with the mean flow velocity.

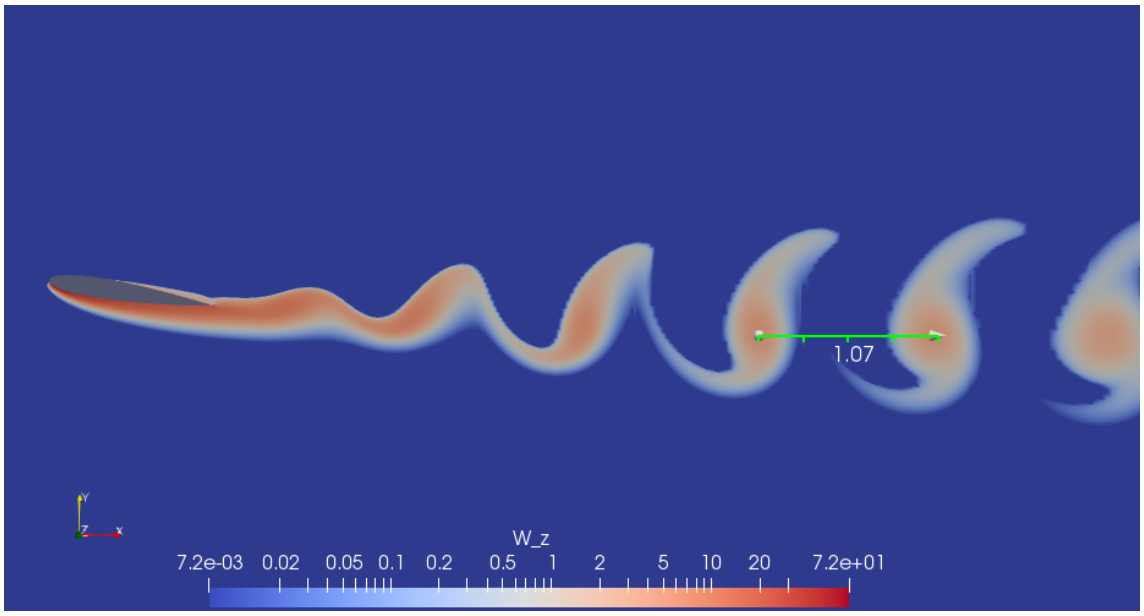

Figure 2.4: Vorticity Contour

2.2. Stream-wise normal sweeping jet

2.2.1. Experiment description

A single sweeping jet is installed on the airfoil's upper surface, with the nozzle pointing in the normal direction to the airfoil on the jet's position (see the sketch in figure 2.5). As a two-dimensional approach, the plane where the jet oscillates is the XY.

This is not the typical sweeping jet configuration, as the jet's direction is perpendicular to the streamwise direction over the upper surface.

The below figure represents how the jet would be located (notice that the jet is oversized to be able to see it clearly). However, the jet has been simulated by imposing a velocity boundary condition instead of designing and implementing a real jet cavity.

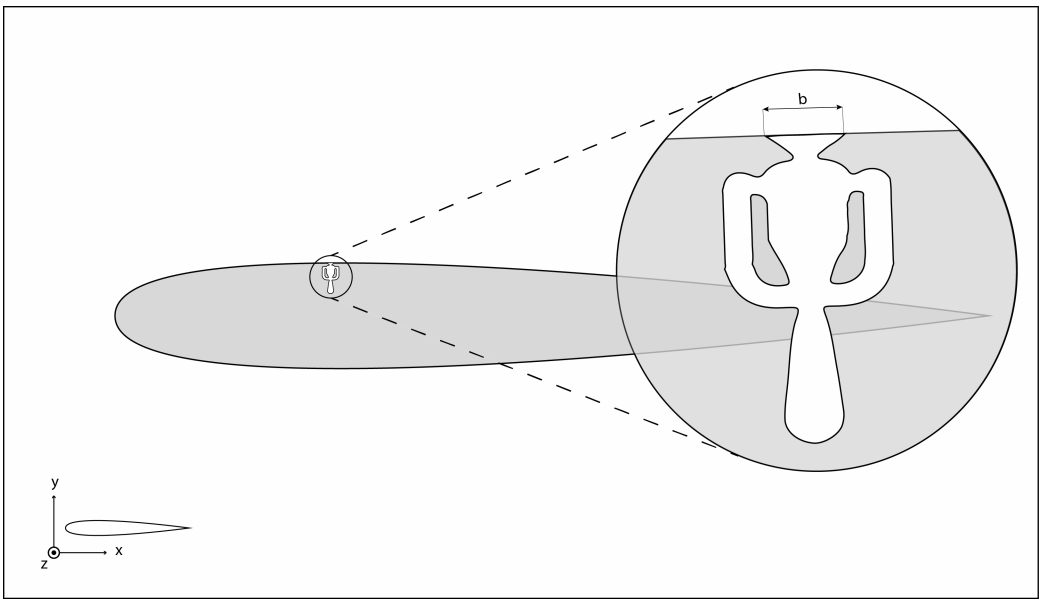

Figure 2.5: Jet positioning sketch

2.2.2. Mesh configuration

As discussed above, the geometry of the airfoil hasn't been modified nor adapted to add a jet slot. This doesn't mean that the mesh doesn't need a refinement to accurately capture the jet dynamics over the airfoil (indeed, it does: see the figure 2.6). That's the reason why a narrow refined region has been included over the jet cavity and extended up to the far field to preserve the structured mesh.

Starting from the airfoil surface, in the jet opening mesh, both lines holding the structure move apart gradually at a constant pace to balance the mid field and far field regions. Just above the jet, there is the closest part of the region along the new vertical grid to find the most accurate values. On top, in the far field region there is quite more space between node lines as the solutions don't need to be as precise.

The figure below shows the updated mesh to simulate the sweeping jet.

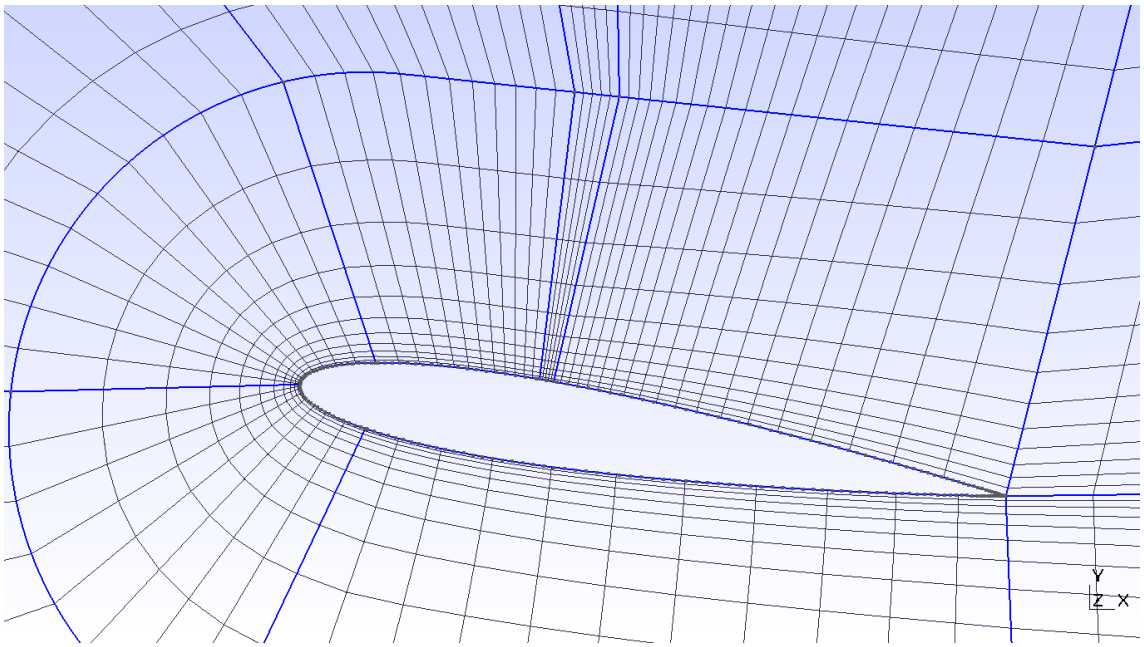

Figure 2.6: Updated mesh for sweeping jet

2.2.3. Jet parameterisation

The jet output has been described in previous sections in a qualitative way: its movement is oscillatory with a non-zero net mass flux. This subsection explains how the jet has been modelled as a time dependent velocity Dirichlet boundary condition and high order homogeneous Neumann boundary condition for pressure. Time dependency is related to the jet angle in this configuration of the jet: the angle varies with time described by a cosine. The output mass flow is kept constant.

Beginning with the SWJ parameterisation, the jet's momentum coefficient is defined as:

$$C_\mu = \frac{\dot{m}_j \overline{v_j}}{\frac{1}{2}\rho_\infty U_\infty^2 c} = \frac{\rho_j \overline{v_j}^2 b}{\frac{1}{2}\rho_\infty U_\infty^2 c} \tag{2.1}$$

Assuming incompressibility of the fluid in all domain ρ_j=ρ_∞, the jet characteristic velocity $\overline{v_j}$ is defined as:

$$\overline{v_j} = \sqrt{\frac{C_\mu {U_\infty}^2 c}{2b}} \tag{2.2}$$

On the other hand, jet's nozzle is composed by two solid walls with no-slip condition. A parabolic profile is used assuming the jet as developing within a channel prior to being released through the actuator port. The final polinomial with 3 degrees of freedom $v(x) = Ax^2 + Bx + C$ is defined by the three following conditions:

$$\begin{aligned} \frac{1}{b}\int_0^b v(x)dx &= \overline{v_j} \\ v(b) &= 0 \\ v'\left(\frac{b}{2}\right) &= 0 \end{aligned} \tag{2.3}$$

Solving the system,

$$A = \frac{-6\overline{v_j}}{b^2} \qquad B = -Ab \qquad C = 0$$

The fact that mass flux is constant implies that normal velocity will remain constant and there will be a time-dependent tangential velocity.

$$V_N(x) = Ax^2 + Bx + C \tag{2.4}$$

$$V_T(x,t) = V_N(x)tg(\theta(t)) \tag{2.5}$$

$$\theta(t) = \theta_m cos(wt) \tag{2.6}$$

Finally, taking into account that the jet is not located on the origin but in a point x_0 on airfoil, which has also a non-zero inclination β and also an angle of attack α (see the figure 2.7), the local vertical *v* and horizontal *u* velocities are described by:

$$\begin{bmatrix} v \\ u \end{bmatrix} = \begin{bmatrix} cos(\beta+\alpha) & -sin(\beta+\alpha) \\ sin(\beta+\alpha) & cos(\beta+\alpha) \end{bmatrix} \begin{bmatrix} v_N(x-x_0) \\ v_T(x-x_0) \end{bmatrix} \tag{2.7}$$

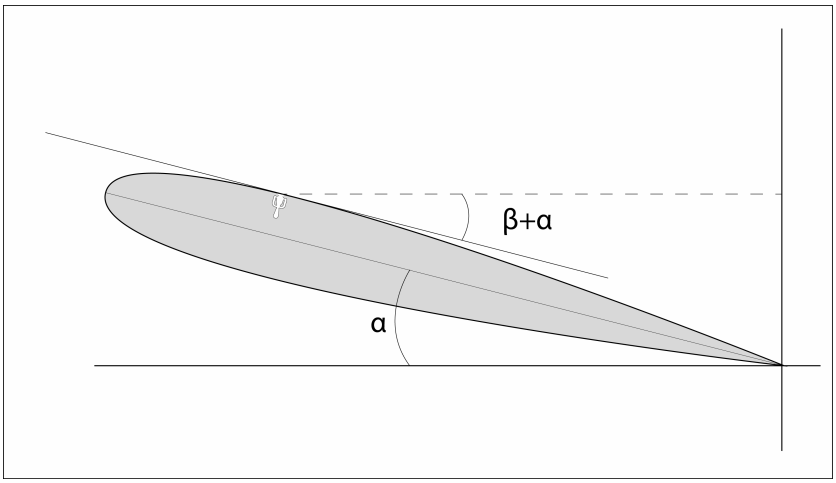

Figure 2.7: Jet orientation sketch

2.2.4. Results and discussion

The studied parameters of the sweeping jet are: its position over the airfoil, the jet's momentum coefficient and the jet's frequency.

As a first approach, the chosen frequency of the jet is the natural frequency of the system (see table 2.1). In the same way as the baseline has been studied, from the temporal signal, the mean, amplitude and frequency has been extracted.

2.2.4.1. Lift coefficient

The figure 2.8 shows how close are the results when obtaining the Fourier transform of the several . t positionsThis is necesjesary in order to get reliable results when the Fourier Transform is applied to the temporal signal, in order to obtain the mean value of the signal, its frequency and amplitude.

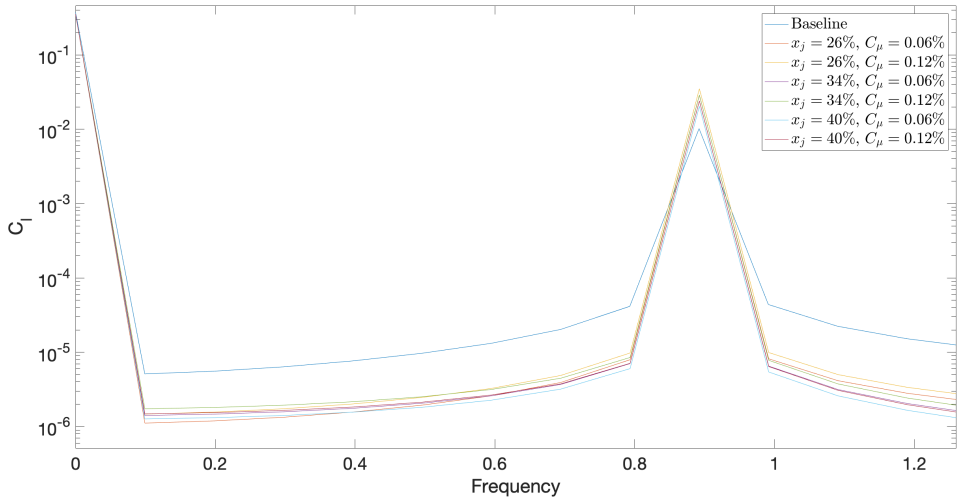

Figure 2.8: Fourier transform of C_l at $f = f_0$

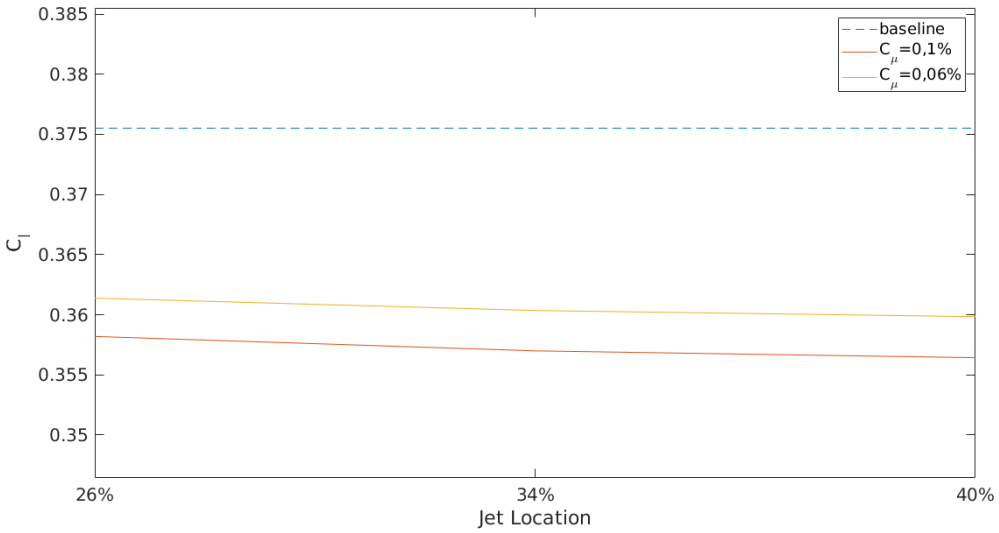

Figure 2.9: At $f = f_0$, mean C_l vs jet locations.

Unfortunately, the mean value of C_l decreases when the jet is activated, and its tendency when changing its position along chord does not seem to improve (see figure 2.9).

One of the parameters aforementioned that also could improve the simulations is frequency. In the following figure 2.10, there is a change compared to the same simulations but two times the vortex shedding frequency. Baseline in this case (standing still exactly as it was in figure 2.8), remains above of the several jet locations simulations. Nonetheless,

in figure 2.11 an improvement can be seen as the jet location is moved backwards. In any case, still far away from any desire or interesting result.

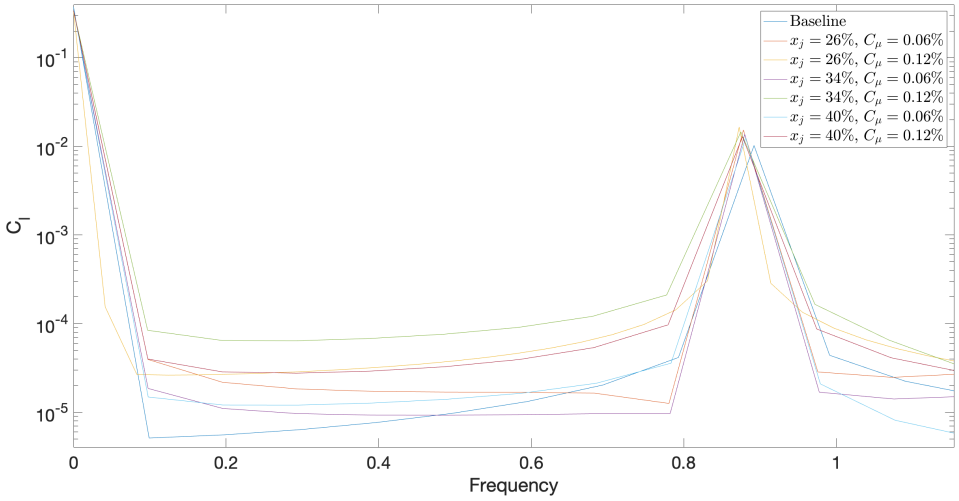

Figure 2.10: Fourier transform of C_l at $f = 2f_0$

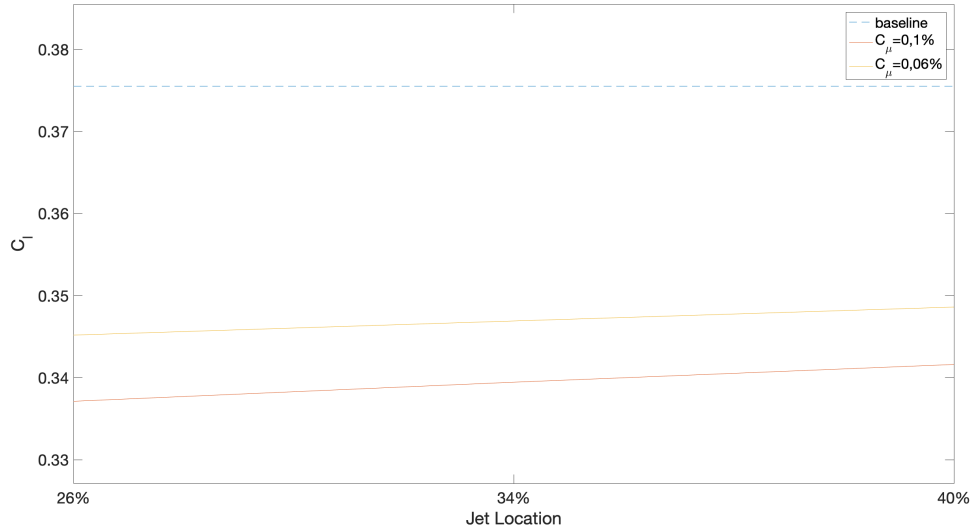

Figure 2.11: At $f = 2f_0$, mean C_l vs jet locations.

Nonetheless, to make sure that vertical jet is not likely to improve terms of lift, three new positions after the boundary detachment were tested. Although increasing the frequency twice as much as the first simulation hasn't improve anything at all , it is interesting to see that the slope tendency is to increase at a good rate. This is a preamble to introduce higher frequencies to try to overcome the baseline results.

Focusing mainly in $C_\mu = 0.06\%$ the figure 2.12 shows how lift looks like according to the new x_j positions along the airfoil and different harmonics of the frequency used throughout the whole study:

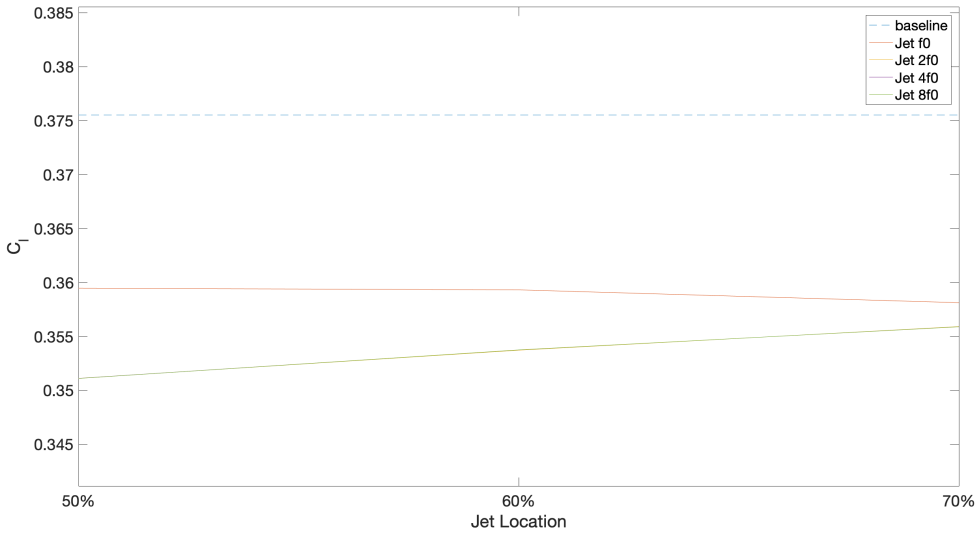

Figure 2.12: Mean C_l vs jet locations. and different frequencies

It is actually quite hard to distinguish the lift evolution between the jet within $2 \cdot f_0$ and $4 \cdot f_0$ frequencies as they are nearly overlapped. Thus, this is a bad outcome to one of the questions about vertical jet, as the overall simulations do not perform good. It seems that the lower simulations ($4 \cdot f_0$ and $8 \cdot f_0$) of the above figure do enhance referring to the previous jet locations in terms of slope but still not reaching the baseline results. By looking at the values ranging among jet simulations,they are clearly lower than further positions, therefore, vertical jet can be discarded referring to lift performance.

2.2.4.2. Drag coefficient

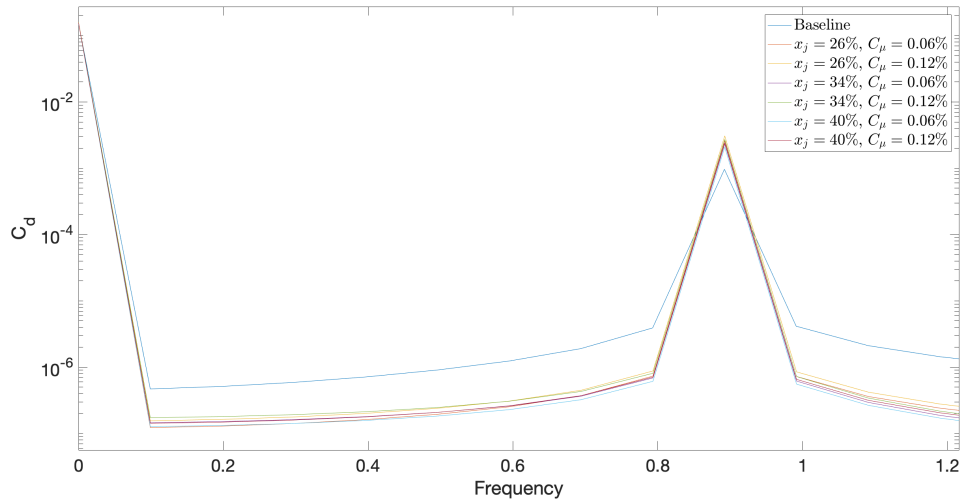

Figure 2.13: Fourier transform of C_d at $f = f_0$, C_d vs Time for different C_μ and jet locations.

Stepping into drag coefficient, things start to change a bit. Firstly, by looking the figure 2.13, the drag seems to be way higher than the baseline, thus not an option for the improvement.

In the second place, it can be observed that the tendency in this case 2.14 is diminishing exactly as lift, but this is a different situation as drag needs to lower in order to improve the airfoil condition. Beginning with 25% and progressing towards 40% it already can be seen how the further back the jet location is set, the lower the drag coefficient value. To that end, new jet positions were tested to see whether the drag keeps reducing or stagnates around baseline.

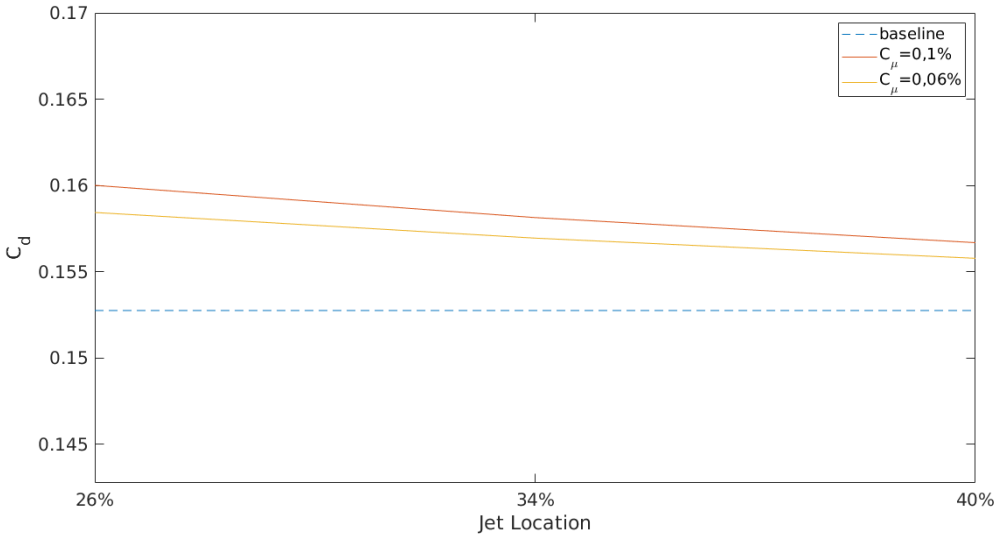

Figure 2.14: At $f = f_0$, mean C_d vs jet locations.

The plot in the figure 2.15 contains the final simulations with also the same frequencies that were used with the lift results above.

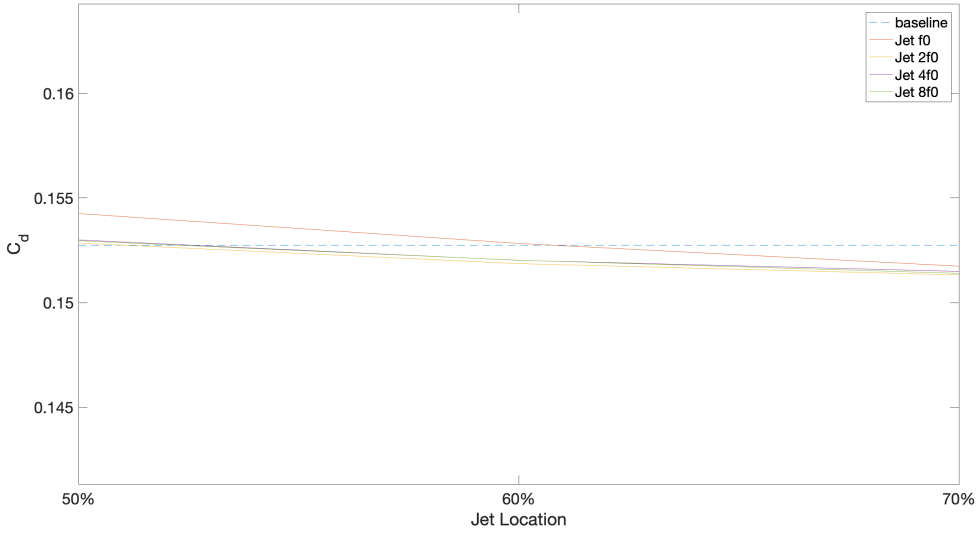

Figure 2.15: Mean C_d vs jet locations. and frequencies

Taking the baseline as the main reference for the study, it can be seen how further back jet positions are preferred rather than positions close to the boundary layer detachment. Moreover, lift is also performing better even though is still not good as the baseline.

Retrieving all the simulations and results so far, the vertical jet it's clearly one possibility to reduce drag but probably it won't be worth using it as lift enhancer.

However, as drag improvement is insignificantly low, it's probably not worth price improvement. It's a sure thing that installing this blow devices in each wing, requires re-designing part of the upper surface and having several bleed air pipes. This would probably cause an economic impact and not to add that it would need some dates for regular revisions as this is suppose to trade flaps for sweeping jet. It would actually become a serious safety device in the airplane due to the risk of stall or miss take off.

The table below summarizes the vertical jet with the obtained data:

	$\overline{C_l}$	$\overline{C_{lv}}$	$\overline{C_{lp}}$	$\overline{C_d}$	$\overline{C_{dv}}$	$\overline{C_{dp}}$	$\overline{E}$
Baseline	0.3755	0.0028	0.3727	0.1527	0.0753	0.0774	2.47
Jet @26%	0.3614	0.0022	0.3592	0.1584	0.0764	0.0820	2.28
Jet @34%	0.3604	0.0023	0.3581	0.1569	0.07662	0.0803	2.30
Jet @40%	0.3598	0.0023	0.3575	0.1557	0.07666	0.0791	2.31
Jet @50%	0.3595	0.0024	0.3571	0.1542	0.0765	0.0777	2.33
Jet @60%	0.3593	0.0024	0.3569	0.1528	0.0762	0.0766	2.35
Jet @70%	0.3581	0.0024	0.3556	0.1517	0.0759	0.0758	2.36

Table 2.2: Vertical jet results at $f = f_0$

	$\overline{C_l}$	$\overline{C_{lv}}$	$\overline{C_{lp}}$	$\overline{C_d}$	$\overline{C_{dv}}$	$\overline{C_{dp}}$	$\overline{E}$
Baseline	0.3755	0.0027	0.3727	0.1527	0.0753	0.0774	2.45
Jet @26%	0.3452	0.00198	0.3432	0.1557	0.0759	0.0798	2.21
Jet @34%	0.3469	0.0020	0.3448	0.1546	0.0762	0.0784	2,24
Jet @40%	0.3486	0.0021	0.3464	0.1538	0.0763	0.0775	2,26
Jet @50%	0.3511	0.0022	0.3488	0.1528	0.0763	0.0765	2.29
Jet @60%	0.3537	0.0023	0.3513	0.1518	0.0761	0.0757	2,33
Jet @70%	0.3559	0.0024	0.3534	0.1513	0.0759	0.0755	2,35

Table 2.3: Vertical jet results at $f = 2f_0$

The shadowed rows are the ones corresponding to the baseline to reference our simulations. The blue highlighted cells are the ones owning the highest lift and lowest drag.

By looking at the tables it can be considered that the amount of reduced drag is tiny, and adding the downside of the lift coefficient, the vertical jet can be disregarded. Moreover, the last column shows the Efficiency of each jet that compared to the baseline are appreciably worse. Surprisingly, no matter where the jet is located and what is the frequency at which the jet is oscillating, the rearmost jet set at 70 % of the chord, is the one working better in terms of drag coefficient. However, switching to lift coefficient, the frequencies f_0 to $2 \cdot f_0$ do not coincide in order. Whilst for f_0 (table 2.2) the greater lift coefficient is produced closer to the leading edge, for $2 \cdot f_0$ (table 2.3) the higher lift coefficient values are found closer to trailing edge. It's not a trivial result as firstly, it was thought that jet could improve the airfoil performance around the boundary layer detachment of the baseline for the given angle of attack. Regardless of these differences of drag and lift coefficients, baseline is still on top of the results.

To contrast the conclusions shown in the tables 2.2 and 2.3, there are the snapshots contained in figure 2.16 showing how the streamlines spread with the influence of the jet depending on its position. The first three correspond to f_0 and the last three to $2 \cdot f_0$ (indicated in each caption).

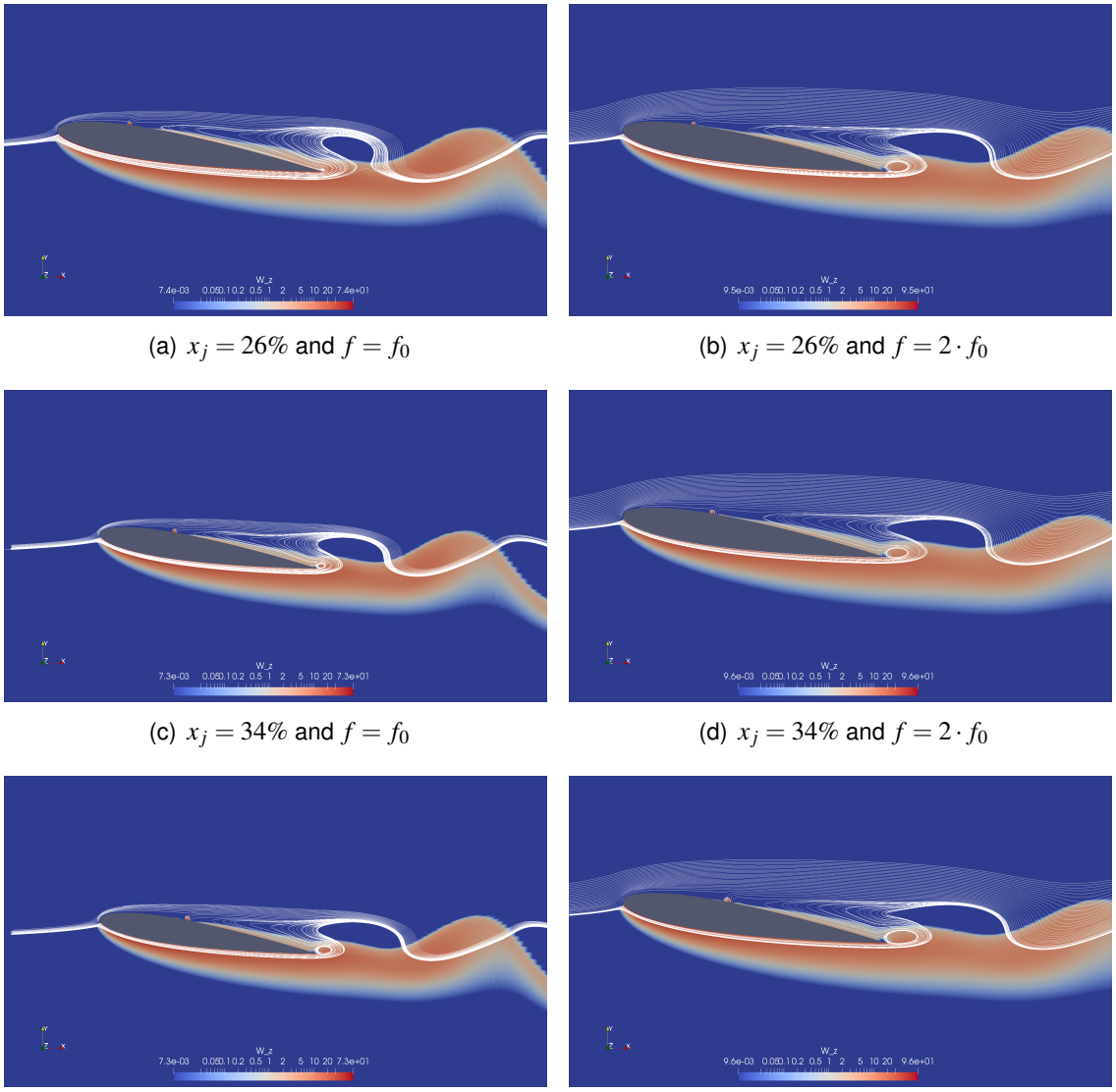

(a) $x_j = 26\%$ and $f = f_0$

(b) $x_j = 26\%$ and $f = 2 \cdot f_0$

(c) $x_j = 34\%$ and $f = f_0$

(d) $x_j = 34\%$ and $f = 2 \cdot f_0$

(e) $x_j = 40\%$ and $f = f_0$

(f) $x_j = 40\%$ and $f = 2 \cdot f_0$

Figure 2.16: Vorticity contours and streamlines for the

All of cases share a common problem related with boundary layer detachment, the re-circulations. As a consequence of the disturbance introduced by the jet, there is an early boundary layer detachment that makes the fluid re-circulate meaning that it becomes turbulent and worsens the whole aerodynamics. Originally there was already a boundary layer detachment that, thereafter was thought to be reduced or suppressed with the inclusion of the jet. Unfortunately, it hasn't reduced any of it, in fact, it has increased the re-circulations.

In view of that and of the research on several papers mentioned along this study, the jet was change to sweep instead of upwards, towards the right, tangential over the upper surface, trying to delay or keep as long as possible the boundary layer attached.

2.3. Stream-wise sweeping jet

2.3.1. Experiment description

A single jet is located on the upper-surface of the airfoil, as in the previous subsection. The main difference is its orientation. While the previous one's direction was normal to the airfoil, this new configuration describes a jet quasi-tangential to the airfoil. As shown in the image 2.17, the jet's primary direction is on the XY plane and oscillates on Z direction. The expectations are to improve vertical jet's results, reattaching the boundary layer until near the trailing edge.

Taking into account the fact that this is a 2D simulation and the jet oscillates on a non-represented dimension, there will be two cases to study. The first one will represent the XY projection of the jet, which is a constant jet. Its contribution will be a constant momentum injection on boundary layer expecting to reattach it. The second one will vary its mass flux in order to test the effect of introducing a frequency, even if it is not done in the exact way that would be done in real experiment conditions. The jet will be parameterized following a sinusoidal time-dependence, introducing the desired frequency on the boundary layer.

In this case, a change in airfoil's geometry is needed in order to introduce the jet opening.

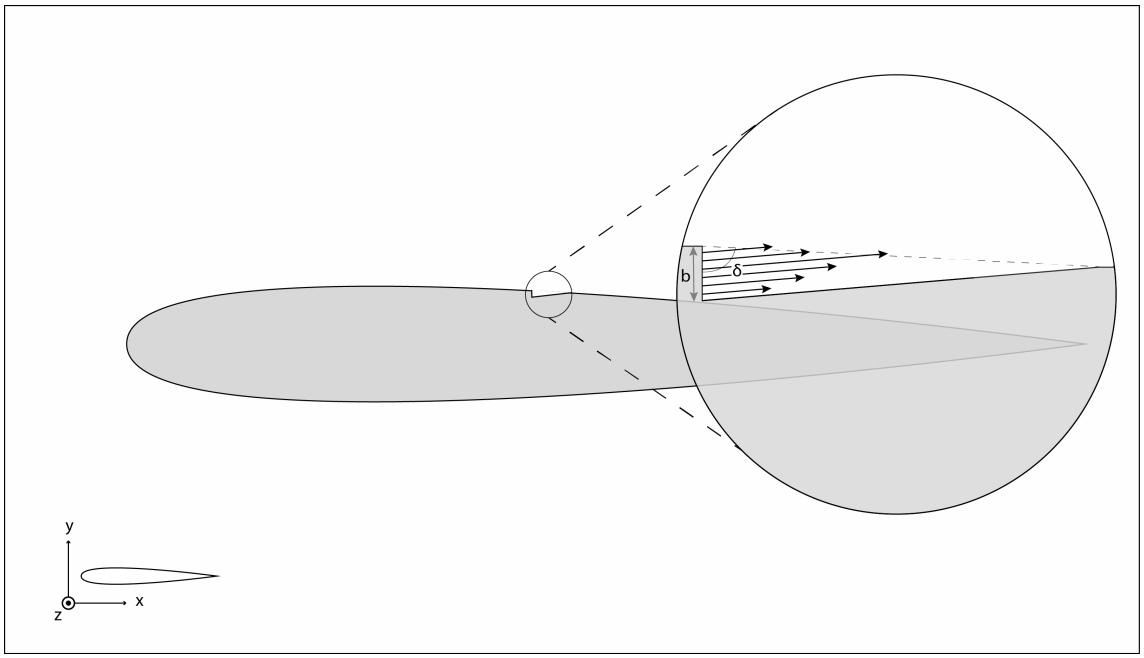

Figure 2.17: Jet positioning sketch

2.3.2. Mesh configuration

With the new jet configuration, the mesh has to include a small, high-order meshed surface near the jet slot. In order to satisfy the transfinite algorithm (which is the algorithm used by Gmsh in order to create structured meshes), a new quadrilateral surface has been included to be meshed (see figure A.4). Also, this little quadrilateral represents the real slot for the jet, which gives more reliability to the obtained results.

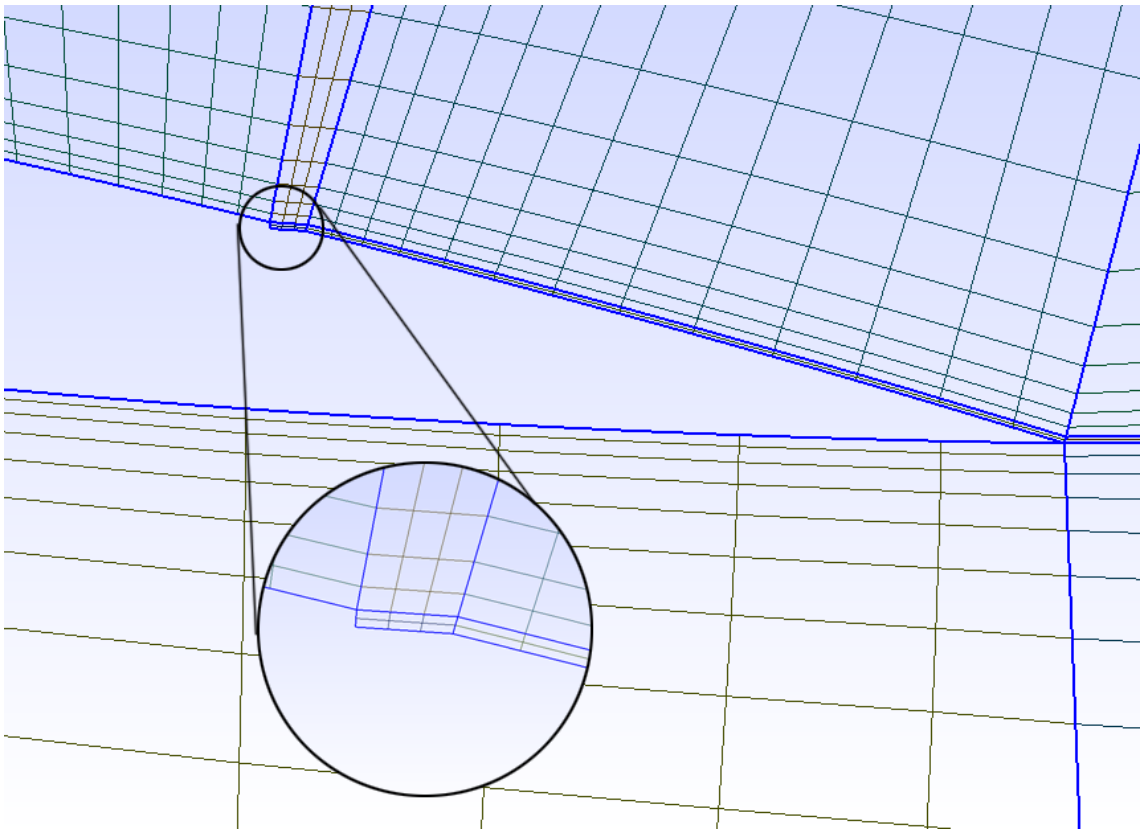

Figure 2.18: Updated mesh for sweeping jet (1)

Also, the mesh has been refined along the upper surface of the airfoil until the trailing edge. This is necessary because the mentioned quadrilateral imposes the mesh to have a new quadrilateral section, since the mesh elements cannot be triangles in this kind of structured mesh. The fact that the mesh has very small elements near the surface is also positive in terms of results reliability, because the boundary layer must be studied carefully and in this area will be high velocities (and then high Reynolds, with smaller turbulent structures) due to the proximity to the jet's nozzle.

2.3.3. Jet parameterisation

Being the velocity of the jet a time-dependent expression, τ_j is defined as the period of oscillation of the SWJ and as the momentum coefficient is variable, the term I_j defines the jet's intensity. Its expression is shown in the equation 2.8. Then, the momentum coefficient is defined as:

$$C_\mu = \frac{\overline{I_j}}{\frac{1}{2}\rho_\infty U_\infty^2 c} = \frac{\frac{1}{\tau_j}\rho_j b \int_0^{\tau_j} u_j^2(t)dt}{\frac{1}{2}\rho_\infty U_\infty^2 c} \tag{2.8}$$

The jet's output velocity u_j is defined as a position-averaged velocity (note that the velocity also depends on the x-coordinate due to the parabolic velocity profile) u_0 plus an amplitude term $u_1 cos(\omega t)$

$$u_j(t) = u_o + u_1 cos(\omega t) \tag{2.9}$$

Performing the integral and making the same assumptions as in the previous sections, the average velocity $\overline{u_o}$ is a function of the momentum coefficient and the amplitude term, too.

$$\overline{u_o} = \frac{3}{2}\sqrt{\frac{c_\mu}{b(2+a)}} \tag{2.10}$$

Being now $\overline{u_0} = u_0/U_\infty$ (and then $u_0 = \overline{u_0} \cdot U_\infty$), $\overline{u_1} = u_1/U_\infty$, and $a = u_1/u_0$. In the studied case, with $U_\infty = 1$, the over-lined parameters (which means their value over the upstream velocity value, then, non-dimensional velocity) coincide with the absolute value of them, but it may be useful for future calculations.

In order to simplify the process, now the parabola defining the velocities profile will be unitary and finally multiplied by u_0. The three conditions imposed to the parabola are now:

$$\begin{aligned} v(x_0) &= 0 \\ v(x_1) &= 0 \\ v\left(\frac{x_0+x_1}{2}\right) &= 1 \end{aligned} \tag{2.11}$$

Where x_0 and x_1 are the geometrical boundaries of the jet slot. It's important to mention that this coordinates are expressed in the global coordinates reference, having their origin at the trailing edge of the airfoil and the x-axis coinciding with the chord at AOA=0º. Performing the required computations and being $v(x) = Ax^2 + Bx + C$,

$$\begin{aligned} A &= \frac{-10x_o^3 + x_0^2 + 2x_0^2x_1 + 2x_0x_1 + 6x_0x_1^2 + 2x_1^3 + x_1^2}{4(x_0 - x_1)} \\ B &= \frac{A(x_1^2 - x_0^2)}{x_0 - x_1} \\ C &= -Ax_0^2 - Bx_0 \end{aligned}$$

Finally, with time and position dependence fully described,

$$u_j(x,t) = (Ax^2 + Bx + C)(u_0 + u_1 cos(\omega t)) \tag{2.12}$$

2.3.4. Results and discussion

As in the previous section, the sweeping jet has many parameters which may have an important effect on the behaviour of the fluid. The first studied parameter is the jet's position on the airfoil. This "stream-wise" jet is assumed to act increasing flow's momentum on boundary layer, preventing its detachment or retarding it. Therefore, the first attempts have been carried out locating the sweeping jet near BL's detachment, either upstream and downstream.

2.3.4.1. SWJ with constant net mass flux

First, the amplitude of oscillation is set to zero in order to determine the effect of adding momentum in the boundary layer, without the intention of modify the natural frequency of the system. The momentum coefficient of the jet is set to 6%.

The output signal showing the evolution of Lift and Drag with time, and its Fourier transform, show that the sweeping jet has the ability of modify flow's behaviour, since its natural frequency has been completely suppressed (see fig. 2.19: the Fourier transform of the signal has no peaks, which are visible on the baseline's signal). It's important to stress that the baseline in this case has the slit of the jet but it's deactivated (as it would be active only during certain phases of the flight).

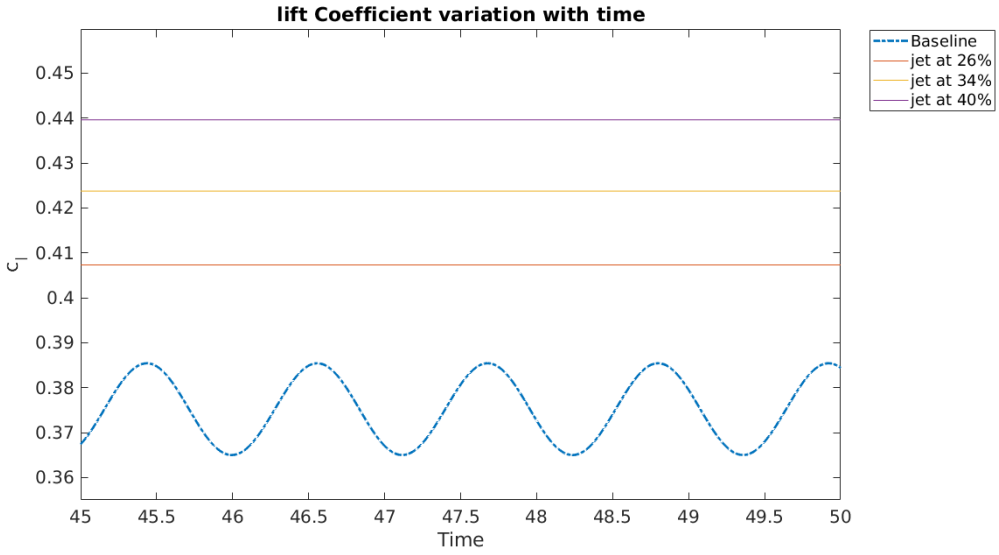

(a) Temporal signal (lift)

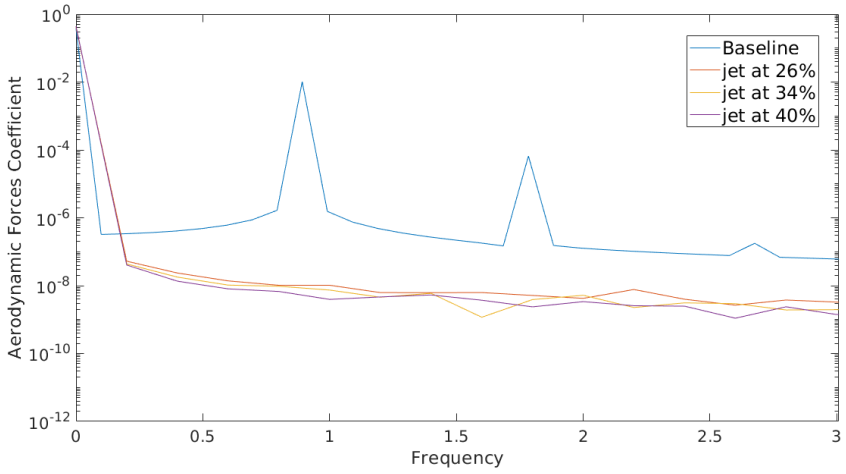

(b) Frequency signal (lift)

Figure 2.19: Lift and drag signals

A near-stationary response has been obtained. This makes easier to understand the flow's behaviour drawing pressure and velocity contours, which will not vary over time. Also, the lift coefficient has increased its mean value between a 10% and a 18% approximately.

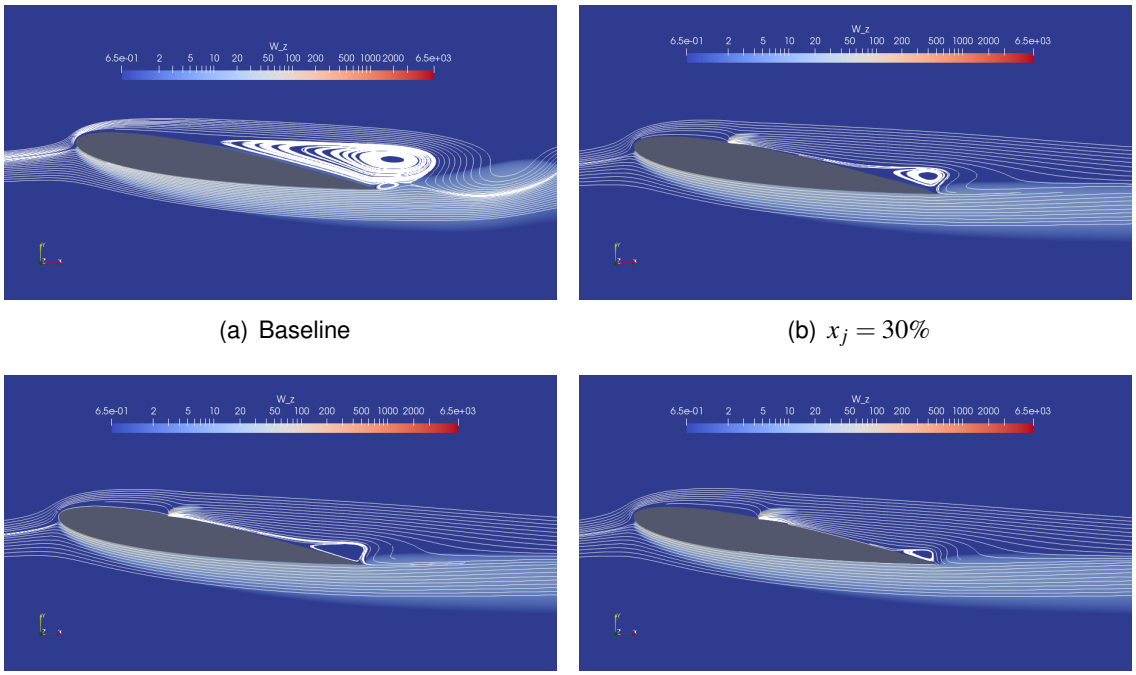

(a) Baseline

(b) $x_j = 30\%$

(c) $x_j = 35\%$

(d) $x_j = 40\%$

Figure 2.20: Vorticity contours and streamlines

The visible recirculations on the Baseline have been reduced and retarded on their position, this is visible in the figure 2.20. The appearance of a big momentum on the upper surface makes the boundary layer stronger in terms of attachment. This is also visible when plotting wall shear stress over the airfoil (Fig 2.21). It is important to point out that the baseline boundary layer separation happens at around the 34% of the chord.

Figure 2.21 shows also that BL's detachment is produced near the trailing edge when the jet is activated. This encourages the authors to perform more experiments with this configuration of the sweeping jet. Also, a huge increase of wall shear stress near the jet has been found. This may imply a viscous drag increase, which is hard to deal with.

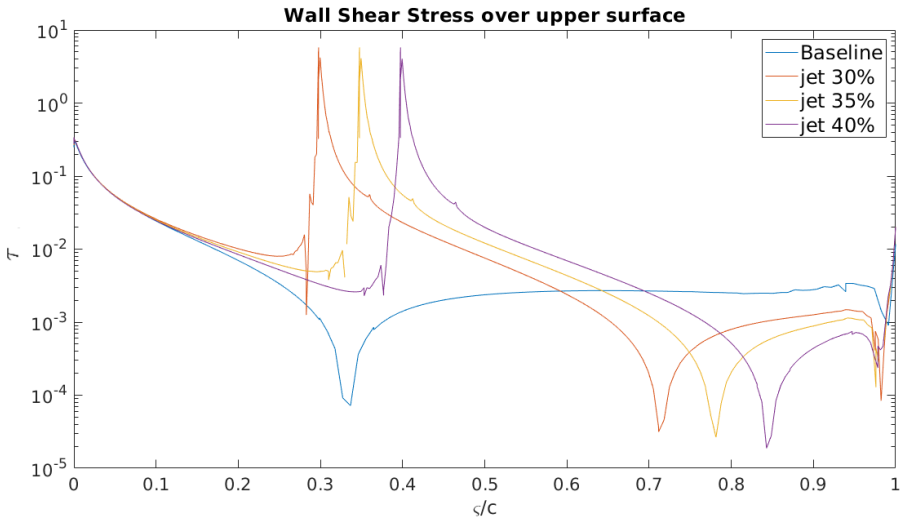

Figure 2.21: Wall shear stress for different locations of the jet

Finally, Fig. 2.22 shows the decrease of pressure coefficient on the upper surface, which increases lift by suction. Surprisingly, the pressure coefficient decreases before the jet and increases after it. The sweeping jet was expected to modify the results in the opposite way: it's well known that an increase of velocity entails a pressure decrease, which would imply a suction peak before the jet.

The fact that an increase of lift is produced before the sweeping implies that the positioning of the jet near the trailing edge may have huge benefits in terms of lift increase.

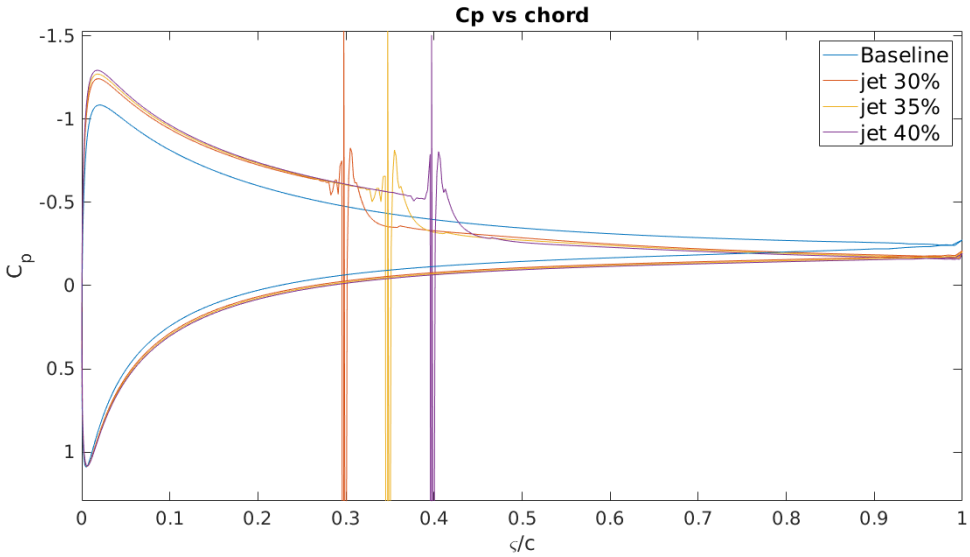

Figure 2.22: Pressure Coefficient over upper and lower surfaces along chord

Concluding on the study of the jet effects on lift for the mentioned positions, is remarkable that pressure lift slightly increases as the jet is moved backwards, and viscous lift remains almost constant. As shown in table 2.1, viscous lift constitutes approximately a 0.7% of the global lift. This doesn't change when the jet is activated, where viscous lift represents between a 0.03% and a 0.5% of the total lift, depending on the jet's position.

The drag coefficient variation with the sweeping jet actuator has been studied too. Previous simulations without the effect of the sweeping jet have been performed, obtaining the drag coefficient values shown in the table 2.1. Neither viscous and pressure drag are negligible, since each of them constitute approximately a 50% of the drag.

A relevant decrease of pressure drag has been found when the sweeping jet is activated, in every jet position. This may be caused by the fact that the jet has the authority to reattach the boundary layer to the airfoil until near the trailing edge (see figures 2.20 and 2.21).

On the other hand, viscous drag has suffered a big increase, possibly due to the fact that a high-velocity flux has been generated near the upper surface. The velocity of the sweeping jet on its output is approximately 4 times the upstream velocity, in order to satisfy the momentum coefficient requirements with such a small nozzle of the jet.

Due to the increase of viscous drag, the overall drag has increased by approximately a 24% independently of the jet's position. The figure 2.23 shows how it slightly varies.

This configuration of the sweeping jet has made lift and drag increase due to the explained factors. A crucial parameter which must be taken into account is the aerodynamic efficiency $E = C_l/C_d$.

The sweeping jet has not been able to improve the aerodynamic efficiency of the wing section with this configuration of the jet (table 2.4), but figures 2.23 and 2.24 show that there is a positive evolution of the efficiency retarding the SWJ's location.

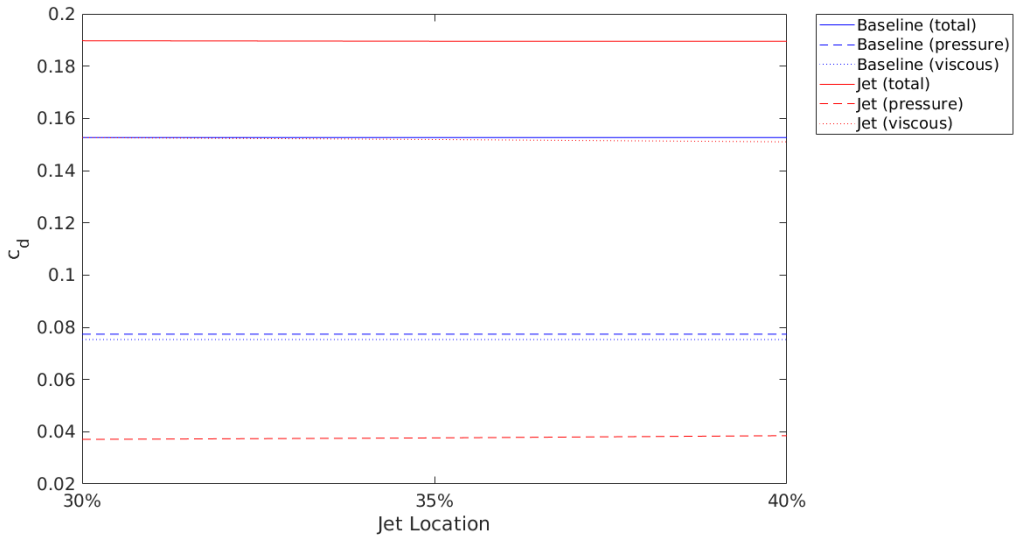

Figure 2.23: Total, viscous and pressure drag

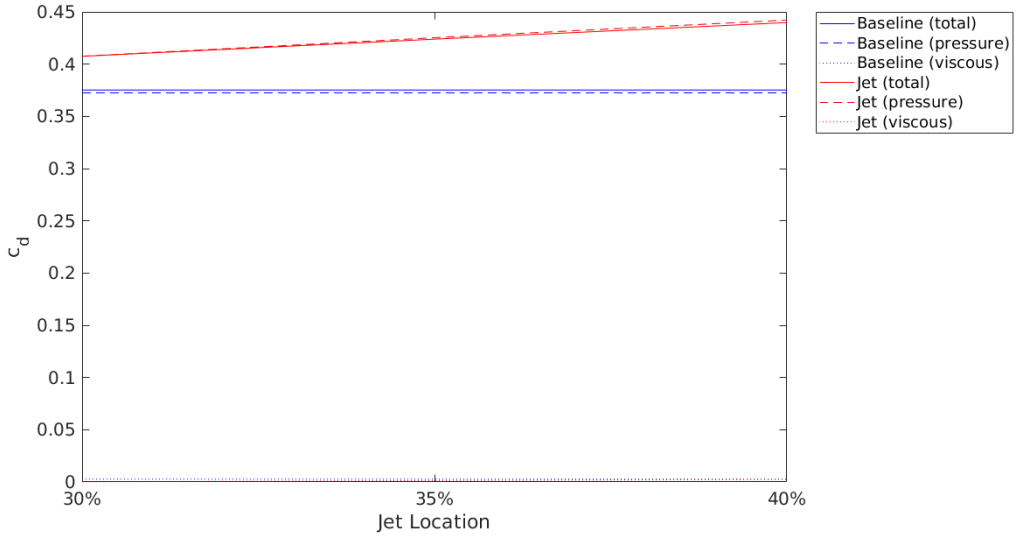

Figure 2.24: Total, viscous and pressure lift

	$\overline{C_l}$	$\overline{C_{lp}}$	$\overline{C_{l_v}}$	$\overline{C_d}$	$\overline{C_{dp}}$	$\overline{C_{dv}}$	$\overline{E}$	BL's sep.[%c]
Baseline	0.3752	0.3725	$2.77{\cdot}10^{-3}$	0.1527	0.0773	0.0753	2.4583	34
Jet @30%	0.4075	0.4076	$-1.37{\cdot}10^{-4}$	0.1897	0.0371	0.1526	2.1486	71
Jet @35%	0.4239	0.4253	$-1.36{\cdot}10^{-3}$	0.1895	0.0376	0.1519	2.2374	78
Jet @40%	0.4398	0.4422	$-2.38{\cdot}10^{-3}$	0.1895	0.0385	0.1510	2.3216	84

Table 2.4: Tangential jet results

The section 2.2.4. shows that there is a relationship between the frequency of the jet and the drag coefficient, concretely finding that a frequency two times the one of the vortex shedding decreases drag, which is one of the problems found on the new jet configuration.

Also, the fact that latter positions of the sweeping jet significantly increases lift encourages the study to perform simulations with a non-stationary sweeping jet located between the 60% and the 85% of the chord.

2.3.4.2. SWJ with variable net mass flux

a Momentum coefficient and jet position study

In order to introduce a frequency in the domain, the jet is defined to vary its mass flux by a time-dependent cosine. This is the main reason why this configuration of the sweeping jet has been parameterized in a different way as the previous one (section 2.2.4.).

Also, location has been moved to 60% and 85% of the chord, because of the increasing trend found in the previous subsection.

The amplitude of the oscillating sweeping jet has been set to a 30% of its mean value, and its frequency is equal to the vortex shedding frequency. Also, the simulations have been performed using different momentum coefficients of the jet: C_μ=4% and $C_\mu = 7\%$.

Now, the temporal signal of lift and drag is not stationary (as in the baseline), so the discrete Fourier transform has been applied again in order to obtain the mean values of the studied parameters, and also the output frequency and amplitude. The figure 2.25 shows the mentioned phenomenon. From a converged solution of the Baseline, several simulations with an activated sweeping jet have been carried out, showing that the oscillating behaviour of the output signal may be worth studying.

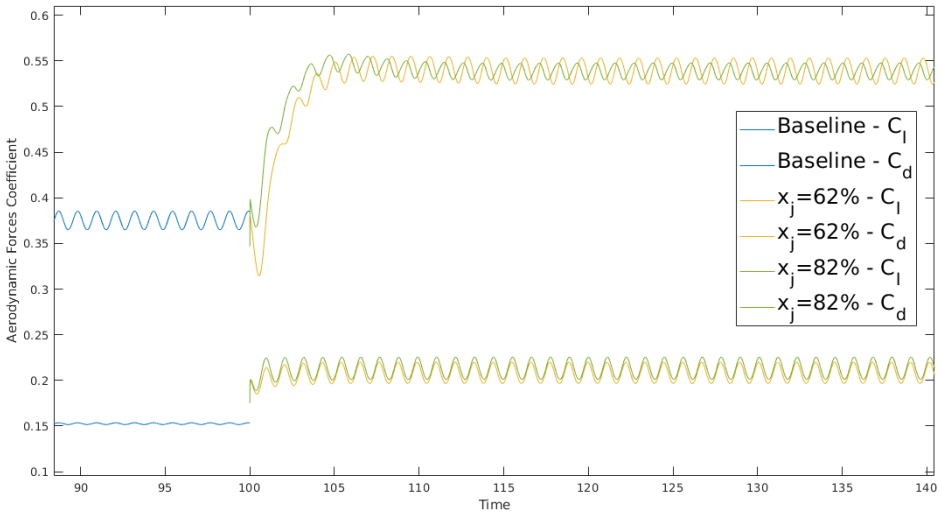

Figure 2.25: Two examples of how the output signal has increased its amplitude

The lift and drag coefficients and the aerodynamic efficiency obtained on the mentioned simulations are plotted in figures 2.26, 2.28 and 2.30 showing their variation with the jet location, with the different tested momentum coefficients. In this case, the time-averaged lift and drag coefficients have been computed, despite the huge amplitude of the output signal. The differences between maximums and minimums will be shown later.

Positive results in terms of lift coefficient increase have been found for both momentum coefficients of the SWJ, finding a local maximum on the 73% of the chord for a $C_\mu = 7\%$, and on the 78% of the chord for a $C_\mu = 4\%$ (see Figure 2.26).

Note that, as happens in the Baseline, the lift coefficient is dominated by the pressure terms. The viscous lift is near zero, as shown in figure 2.27 (the continuous line represents

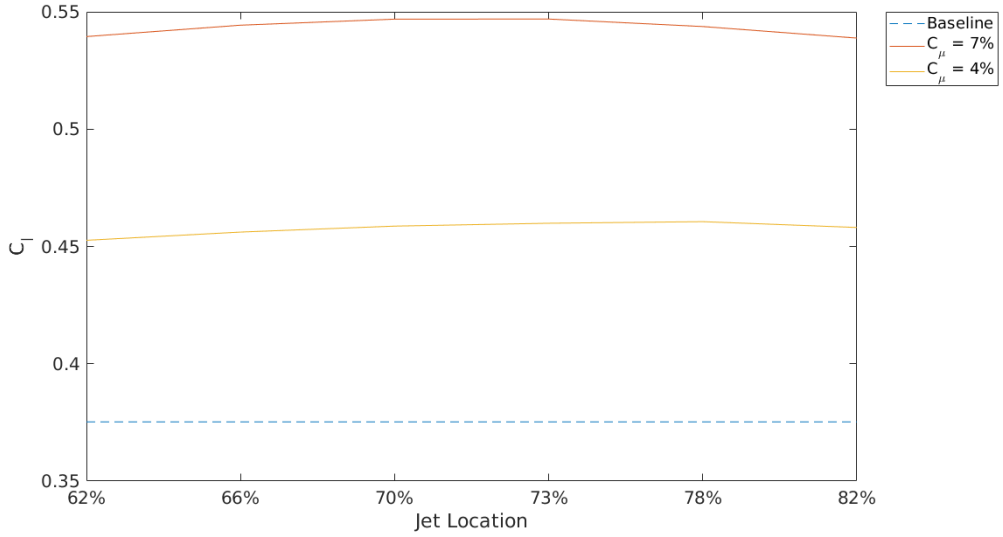

Figure 2.26: C_l variation with the jet position

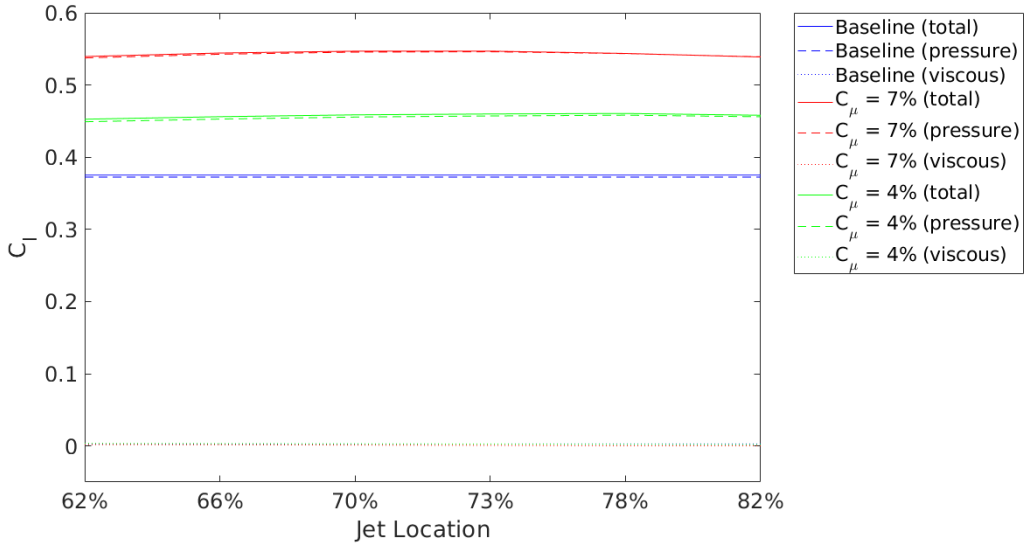

Figure 2.27: Pressure and viscous C_l variation with the jet position

the total lift, the dashed represents the pressure lift, and the dotted line represents the viscous lift).

On the other hand, the drag has undesirably increased its value in every simulation. Although this study focuses on increase lift, the appearance of extra drag may be limiting in many situations (for example, take-off). The figure 2.28 shows how drag is increased with both momentum coefficients and on every location of the jet.

The drag was expected to decrease when activating the jet, since it may reduce (or even suppress) the BL's detachment on the upper surface. Actually, this has happened. The figure 2.29 shows separately the viscous and pressure drag, evidencing the fact that there is actually a drag reduction due to the explained reason, but high velocities near the airfoil surface (at the nozzle of the jet) have increased the viscous drag, driving the total drag to

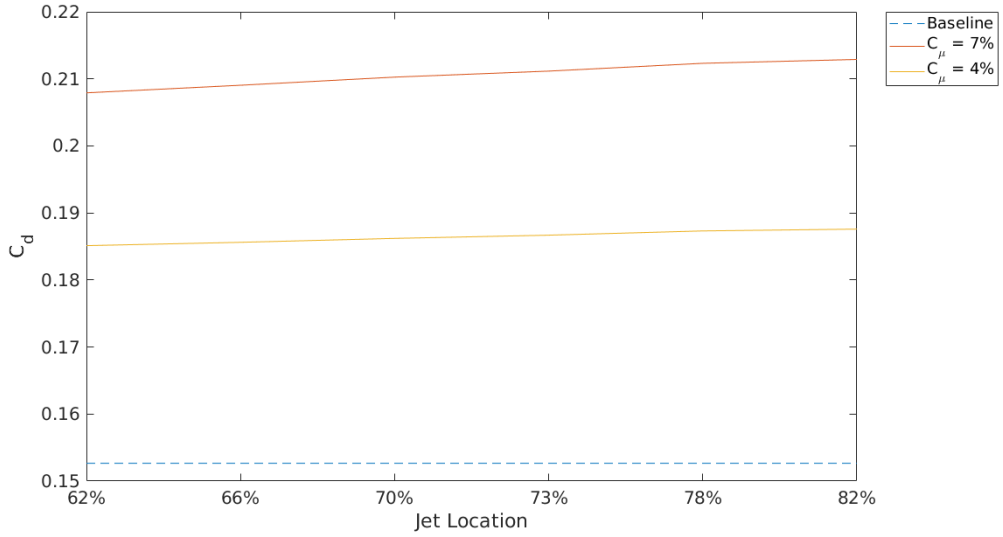

Figure 2.28: C_d variation with the jet position

an increase which obviously depends on the jet momentum coefficient.

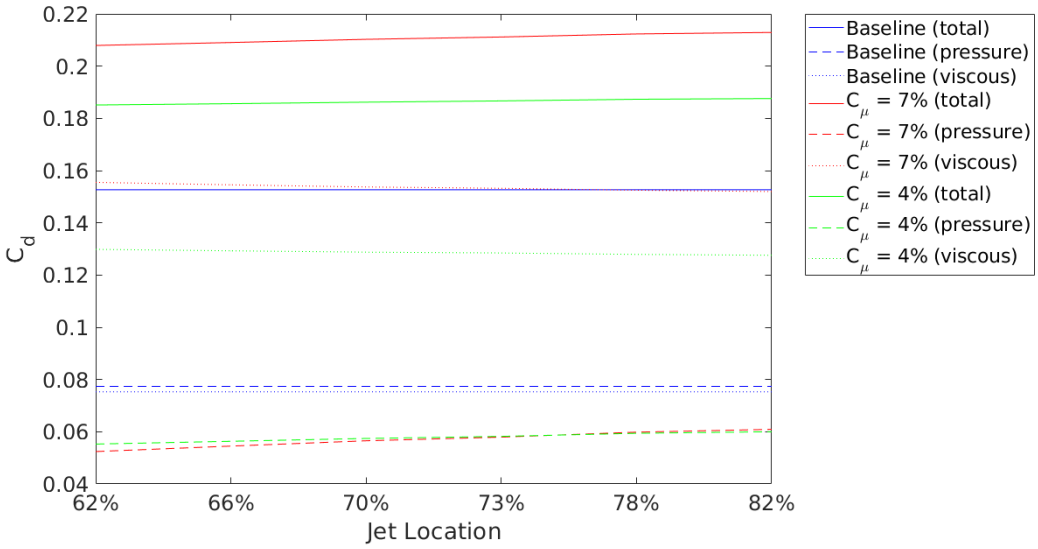

Figure 2.29: Pressure and viscous C_d variation with the jet position

Lift and drag coefficients increase have been found in subsection 2.3.4.1. too, where a constant net mass flux of the sweeping jet was supposed. But, relating this two parameters, the previous section concluded on a decrease of the aerodynamic efficiency ($E = C_l/C_d$)), mostly due to the little increase of the lift coefficient with a huge increase of C_d (as in this case, due to the viscous term). The retardation of the jet over the chord has increased significantly the C_l, remaining the drag coefficient almost the same as in the previous section, making the aerodynamic efficiency increase significantly, until finding higher efficiencies comparing with the baseline. This is shown in the figure 2.30

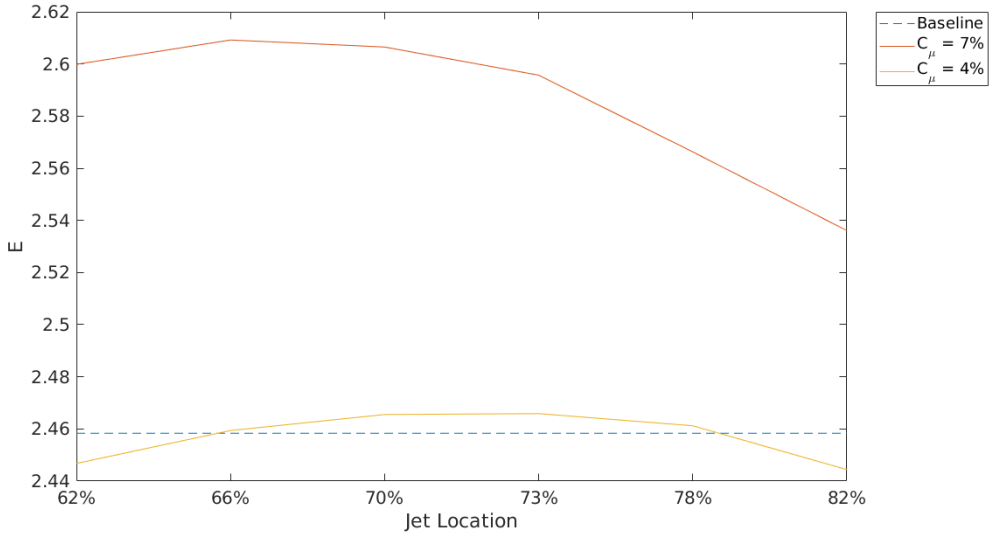

Figure 2.30: Aerodynamic efficiency variation with the jet position

Lift and drag coefficients have been considered to give important information considering only their mean values, but this study tries to explain the reason of the increase (or decrease) of them. The wall shear stress over the upper surface of the wing gives a lot of information of the flow's behaviour, and the pressure coefficient distribution along chord does too.

In order to determine the wall shear stress over the upper surface, the mean value has been found to give less information than the needed. Then, the wall shear stress has been extracted from two points: where the C_l is minimum and when it's maximum over time. The figure 2.31 shows how, depending on time, the flow detaches or not after the sweeping jet. The main reason is that with a variable net mass flux the jet may not be able to reattach the flow near the trailing edge, letting the flow to detach by second time.

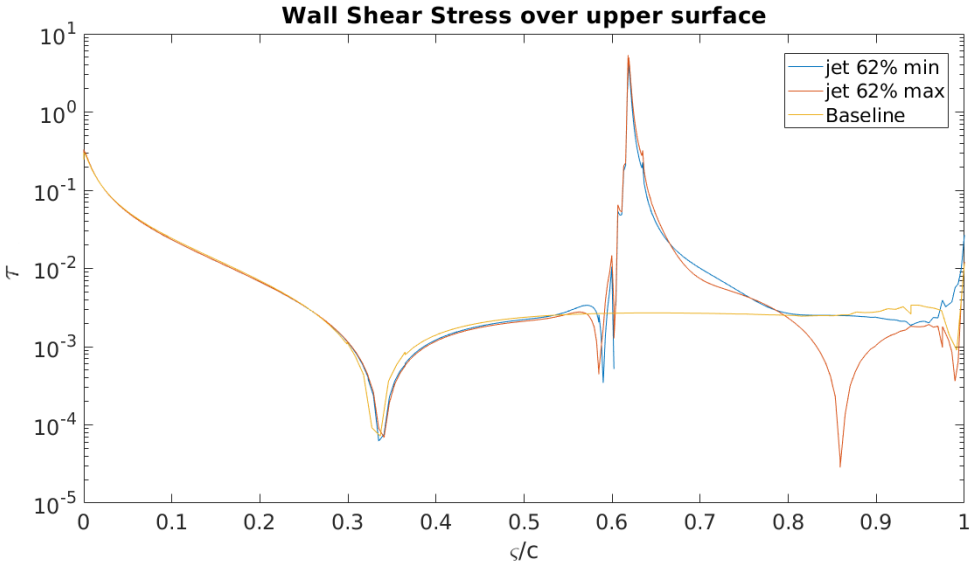

Figure 2.31: Wall shear stress for a $x_j = 62\%$, as an example ($C_\mu = 4\%$).

Due to the explained phenomenon, the wall shear stress over the upper surface has been

studied for both momentum coefficients and all the studied possible positions of the SWJ for the instant when the flow may be detached.

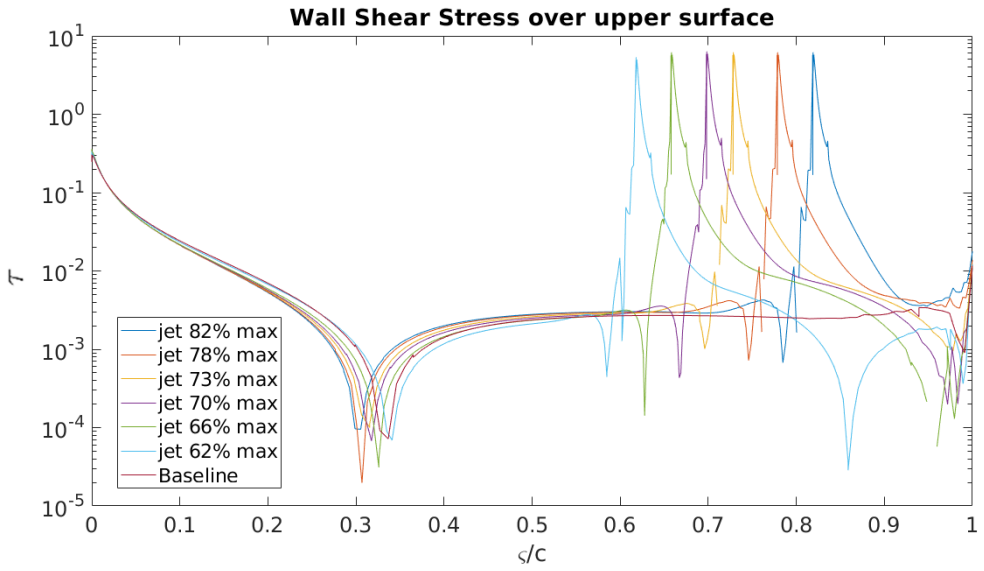

Figure 2.32: Wall shear stress on the upper surface ($C_\mu = 4\%$).

The figures 2.32 and 2.33 make the evidence noticed in the previous section that there is actually a detachment of the BL before the jet, and approximately at the same point that with no sweeping jet. The main difference between both momentum coefficients is the behaviour of the flow after the jet, being the jet with $C_\mu = 7\%$ able keep the flow attached until the trailing edge, while the jet with $C_\mu = 4\%$ is not, and the flow detaches by a second time.

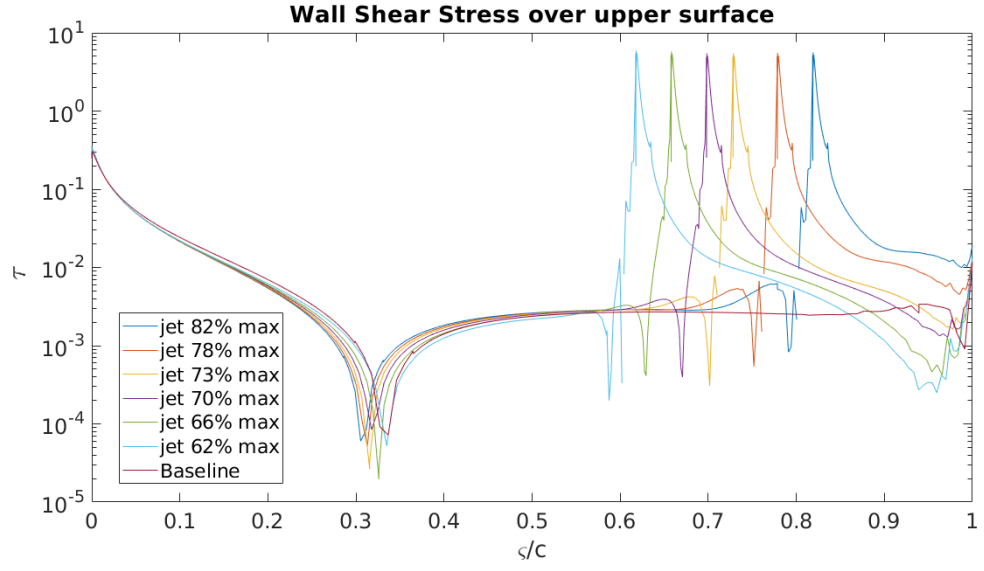

Figure 2.33: Wall shear stress on the upper surface ($C_\mu = 7\%$).

Stepping into the pressure coefficient distribution along chord, the difference between maximum and minimum lift coefficient is not as visible as in the wall shear stress. The main difference is that the lift coefficient is maximum when higher over-pressures are obtained on the lower surface of the airfoil (see figure 2.34). The cause could be the lack of recirculations from the trailing edge when the jet is activated, driving into lower velocities on the lower surface.

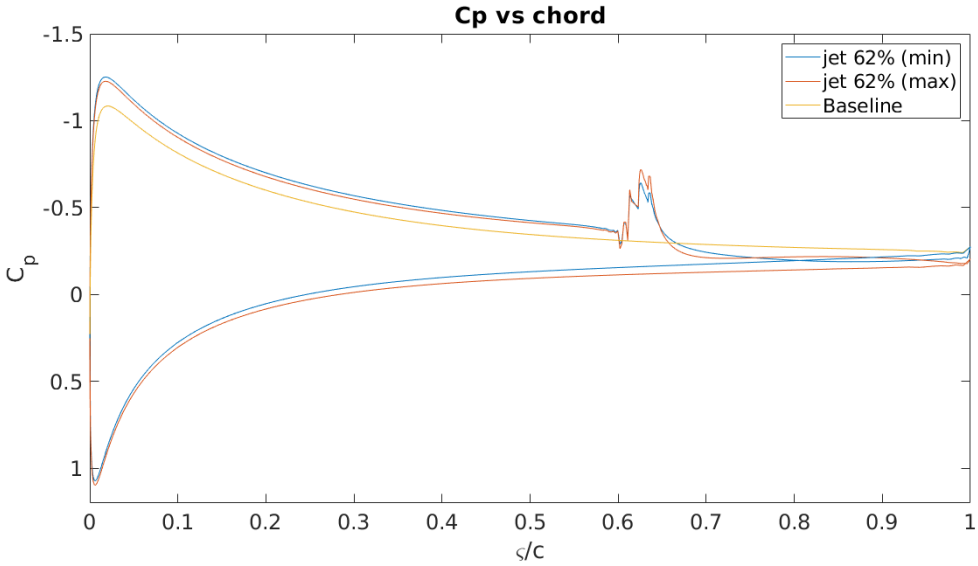

Figure 2.34: Pressure distribution along chord, for a x_j=62%, as an example.

In this case, the time-averaged pressure distribution over chord for the different simulations has been computed, and plotted in figures 2.35 and 2.36.

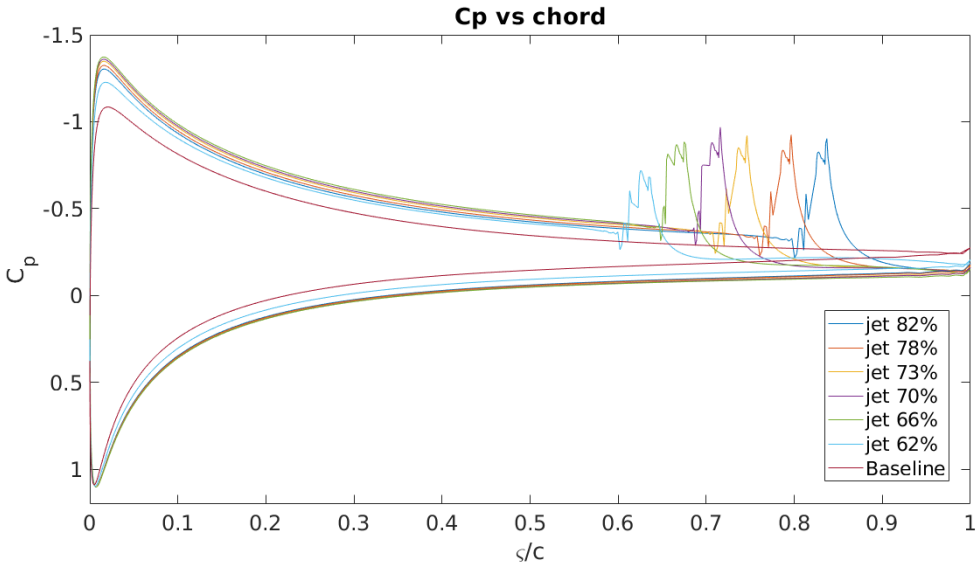

Figure 2.35: Pressure coefficient distribution over chord ($C_\mu = 4\%$).

For every simulation, the pressure distribution experiments changes both on the upper and lower surfaces: in the upper surface the pressure is reduced, increasing suction, and in

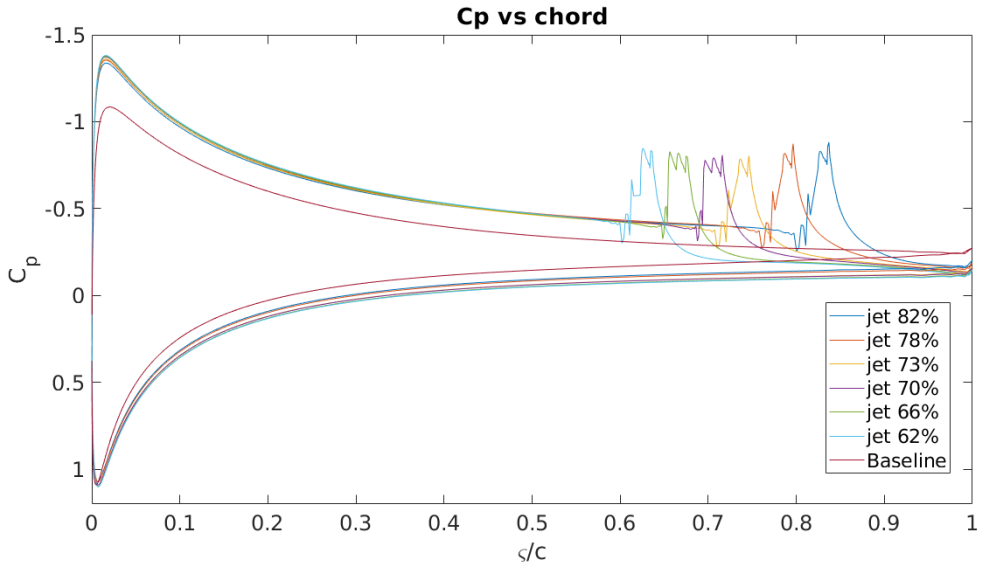

Figure 2.36: Pressure coefficient distribution over chord ($C_\mu = 7\%$).

the lower surface the pressure is increased enhancing the over-pressure and increasing lift too. Downstream from the jet, the suction is reduced with respect to baseline.

Although the explained experiments are not stationary, the streamlines help to understand the numerical result. Streamlines are very helpful when the flow is stationary because they coincide with trajectory lines. In this case, the streamlines are not showing flow's trajectory, while they should be integrated in time. Nevertheless, the vortices produced over the upper surface and on the wake are shown in the plots.

The figure 2.37 shows, for a given position of the jet and a $C_\mu = 7\%$, the difference between the streamlines when the lift coefficient is maximum and when it is minimum. There is an appreciable difference between them near the trailing edge, showing that the vortex is in the opposite position of the oscillation. In both cases, the flow is reattached before the jet.

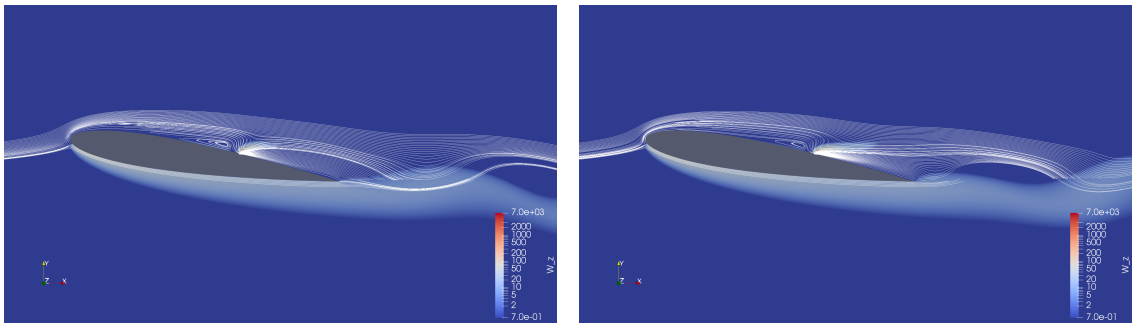

(a) $x_j = 62\%$ and maximum C_L (b) $x_j = 62\%$ and minimum C_L

Figure 2.37: Vorticity contours and streamlines ($C_\mu = 7\%$)

Due to the fact that the study is mostly interested in the flow reattachment and vortices appearance, the streamlines will be averaged. They are plotted in the figure 2.38.

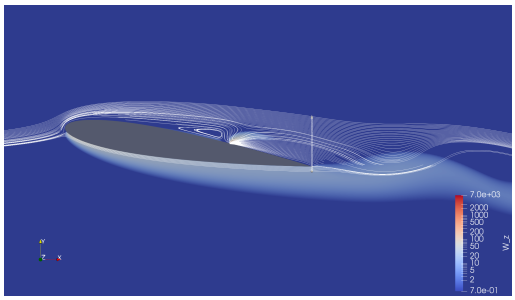

(a) $x_j = 66\%$

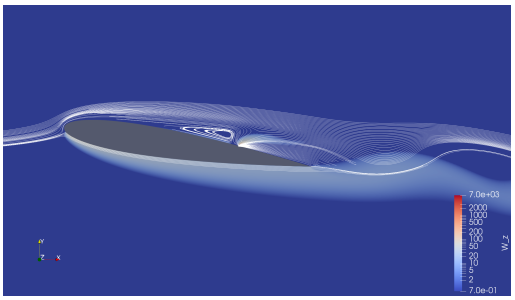

(b) $x_j = 70\%$

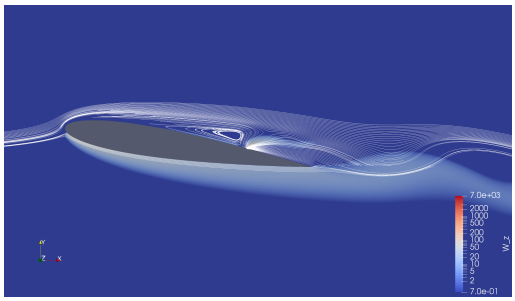

(c) $x_j = 73\%$

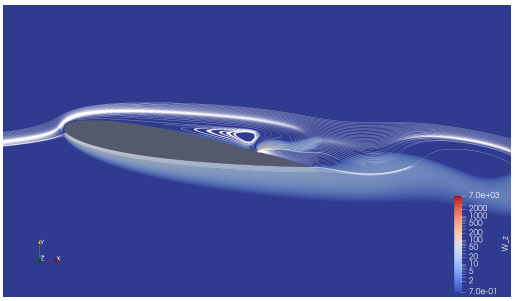

(d) $x_j = 78\%$

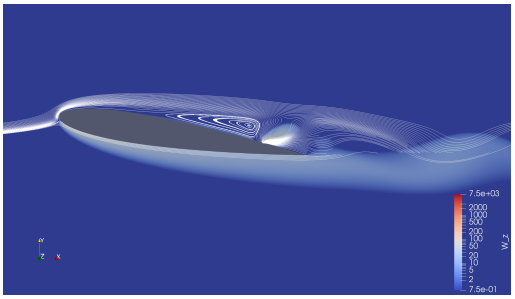

(e) $x_j = 82\%$

Figure 2.38: Vorticity contours and streamlines for $C_\mu = 7\%$

From the simulated cases, $c_\mu = 4\%$ was also interesting as it means lower momentum quantity, thus, less energy required and therefore less money. The results obtained can be observe in the composed Figure 2.39 with all of the jet positions tested.

The same as observed for the case of $c_\mu = 7\%$, it can be seen how the farthest the jet position from the leading edge, the bigger the re-circulations become before the jet. Nonetheless, there is still a re-attachment of the flow thanks to the jet. Likewise, it's also surprising that even though there is a flow detachment before the jet, the produced lift is higher, specially for the locations of the jet at $x_j = 73\%$ and $x_j = 78\%$ for $c_\mu = 4\%$ and $x_j = 70\%$ and $x_j = 73\%$ for $c_\mu = 7\%$. These values are collected in the Table 2.5 and 2.6 highlighted in cyan color.

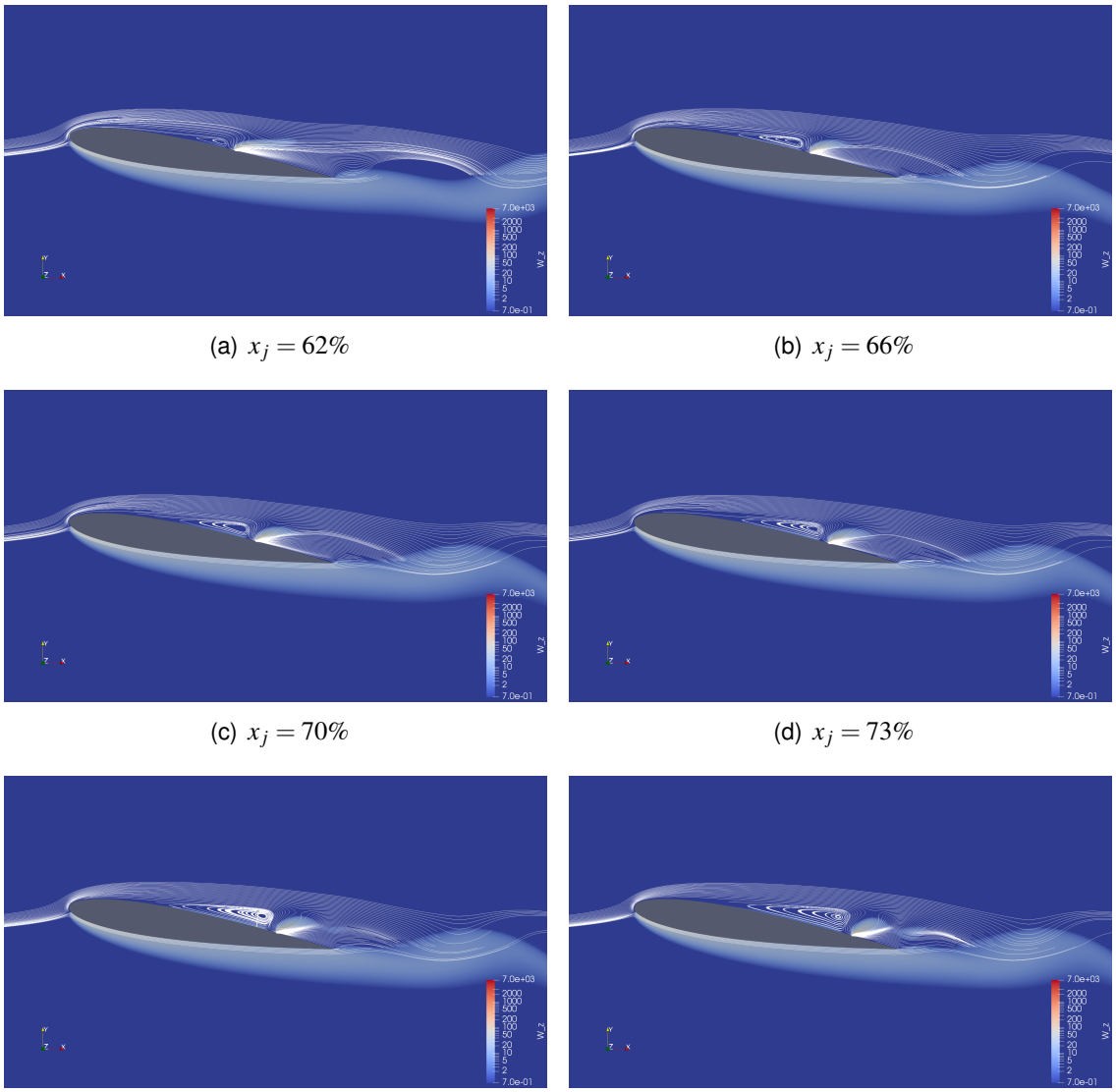

(a) $x_j = 62\%$ (b) $x_j = 66\%$

(c) $x_j = 70\%$ (d) $x_j = 73\%$

(e) $x_j = 78\%$ (f) $x_j = 82\%$

Figure 2.39: Vorticity contours and streamlines for $C_\mu = 4\%$

Table 2.5 retrieves all the aerodynamic parameters of the simulations regarding $c_\mu = 4\%$. It can be observe that the values reaching the highest lift, are the ones corresponding to the jet situated between 73% and 78% of the chord. Drag, instead has the lower values (which are still higher than the one from baseline) in positions 62% and 66%. The higher efficiency then for the case of $c_\mu = 4\%$ is found in between 70% and 73% because the difference with respect to baseline is higher in lift than in drag so higher efficiency is closest to farther positions of the leading edge.

The global values of $\overline{C_l}$ and $\overline{C_d}$, are decomposed in two columns formed $\overline{C_{lv}}$, $\overline{C_{lp}}$, $\overline{C_{dv}}$ and $\overline{C_{dp}}$. It's important to stress that the contribution of pressure is the one holding the highest importance in the case of lift coefficient . On the other hand, viscous lift isn't as important. In drag coefficient, instead, is the one providing almost the 70% of the final value.

	$\overline{C_l}$	$\overline{C_{lv}}$	$\overline{C_{lp}}$	$\overline{C_d}$	$\overline{C_{dv}}$	$\overline{C_{dp}}$	$\overline{E}$
Baseline	0.3755	0.0028	0.3728	0.1527	0.0754	0.0774	2.4584
$x_j = 62\%$	0.4526	0.0035	0.4491	0.1851	0.1298	0.0553	2.4450
$x_j = 66\%$	0.4561	0.0033	0.4528	0.1856	0.1293	0.0563	2.4574
$x_j = 70\%$	0.4587	0.0030	0.4556	0.1862	0.1288	0.0574	2.4633
$x_j = 73\%$	0.4599	0.0028	0.4571	0.1867	0.1285	0.0582	2.4635
$x_j = 78\%$	0.4606	0.0024	0.4582	0.1873	0.1279	0.0594	2.4588
$x_j = 82\%$	0.4581	0.0020	0.4561	0.1876	0.1276	0.0600	2.4420

Table 2.5: Aerodynamic characteristic for $c_\mu = 4\%$

	$\overline{C_l}$	$\overline{C_{lv}}$	$\overline{C_{lp}}$	$\overline{C_d}$	$\overline{C_{dv}}$	$\overline{C_{dp}}$	$\overline{E}$
Baseline	0.3755	0.0028	0.3728	0.1527	0.0754	0.0774	2.4584
$x_j = 62\%$	0.5395	0.0020	0.5375	0.2079	0.1555	0.0524	2.5946
$x_j = 66\%$	0.5443	0.0017	0.5426	0.2090	0.1545	0.0545	2.6037
$x_j = 70\%$	0.5469	0.0013	0.5456	0.2103	0.1537	0.0565	2.6010
$x_j = 73\%$	0.5469	0.0008	0.5461	0.2112	0.1532	0.0579	2.5902
$x_j = 78\%$	0.5437	0.0002	0.5435	0.2123	0.1525	0.0598	2.5609
$x_j = 82\%$	0.5388	0.0003	0.5391	0.2129	0.1520	0.0609	2.5308

Table 2.6: Aerodynamic characteristic for $c_\mu = 7\%$

In the case of $c_\mu = 7\%$, the highest lift coefficients are found between 70% and 73%. Hence this means that increasing the momentum coefficient causes the jet to find its higher lift coefficient in the center of the airfoil upper surface instead than closer to the trailing edge. Drag maintains his lower values at jet locations of 62% and 66% but with higher values (higher difference with baseline). As now the highest lift results are nearest to the drag ones, the higher efficiencies are between 66% and 73%.

2.3.4.3. Amplitude and frequency study

The parameters defining the oscillation of the sweeping jet are basically the amplitude and the frequency. Their non-negligible effect on the flow's behaviour has been demonstrated in section 2.2.4.. Next step for the stream-wise jet is to vary the amplitude and frequency to complete all the modifiable features it has. It is important to know that a simple parameter as frequency can interact with the fluid in its surroundings to improve the behaviour it has and might remain attached along the airfoil.

Amplitude is another key parameter to enhance the overall performance of the aerodynamics. It's basically the difference in speed between the characteristic average jet velocity and the maximum velocity in %. This can be useful depending on the phase of the flight or maybe to any other situation such as the MTOW or the length of the runway.

For this purpose, several simulations with variations in amplitude and frequency have been carried out taking as a reference the best configuration found of the sweeping jet in the previous subsection, which determined that a $C_m u = 7\%$ located in the 73% of the chord achieved an increase of near a 50% of the lift.

a Frequency

Since section 2.2.4. found that sub- and super-harmonics of the natural frequency of the systems f_0 had a determining effect on the drag, multiple studies varying the jet's output frequency have been carried out.

As in the previous sections, the averaged lift and drag coefficients has been computed taking into account that the output signal is not stationary. From a frequency a quarter than f_0 to four times f_0, the lift and drag coefficients are plotted in the figures 2.40 and 2.41. The results with f_0 are the ones concluding the previous subsection.

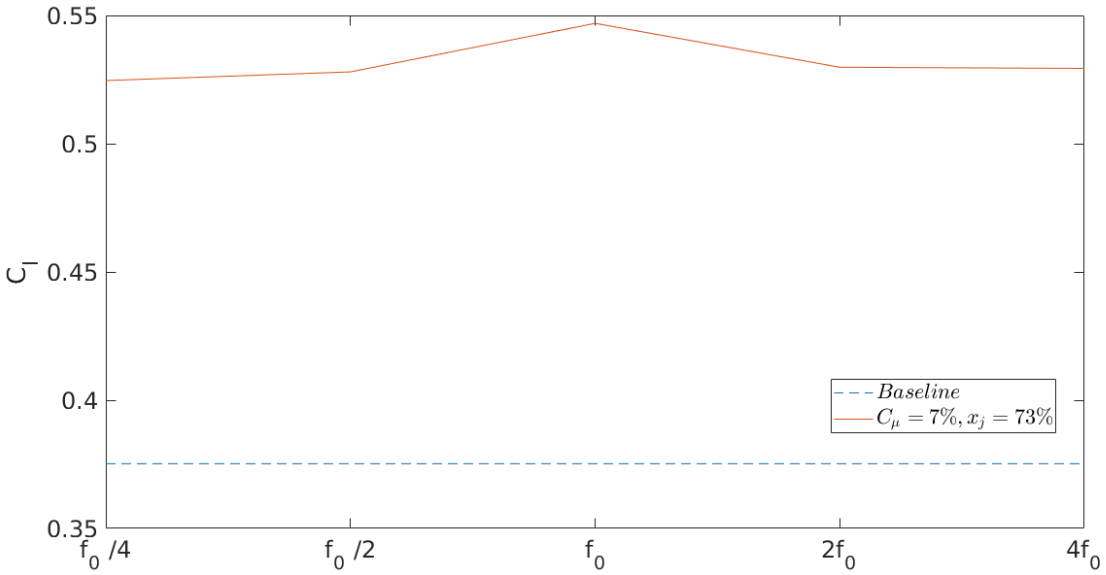

Figure 2.40: C_l variation with the frequency of the SWJ

While the lift coefficient achieves its maximum value at the nominal frequency, there is a significant drag reduction when the frequency is increased (figure 2.41), which is the same

effect found on the section 2.2.4.. Nevertheless, this is not enough to decrease the drag in comparison with the baseline.

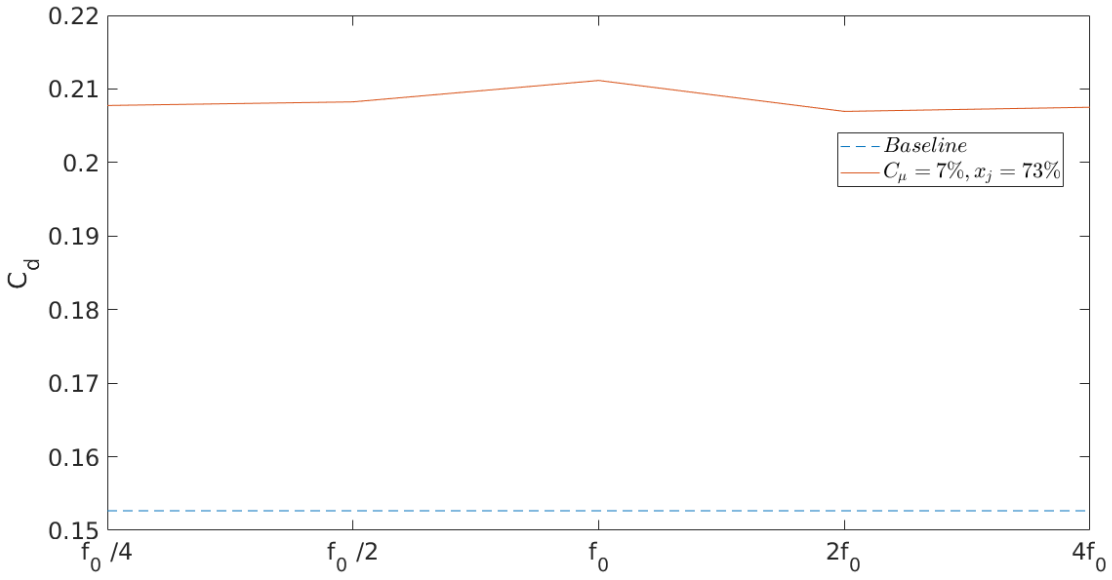

Figure 2.41: C_d variation with the frequency of the SWJ

In conclusion with the frequency study, the aerodynamic efficiency has its peak at the nominal frequency, showing that the achieved drag reductions with sub- and super-harmonics of the nominal frequency are not as significant as the lift coefficient losses, as shown in the figure 2.42.

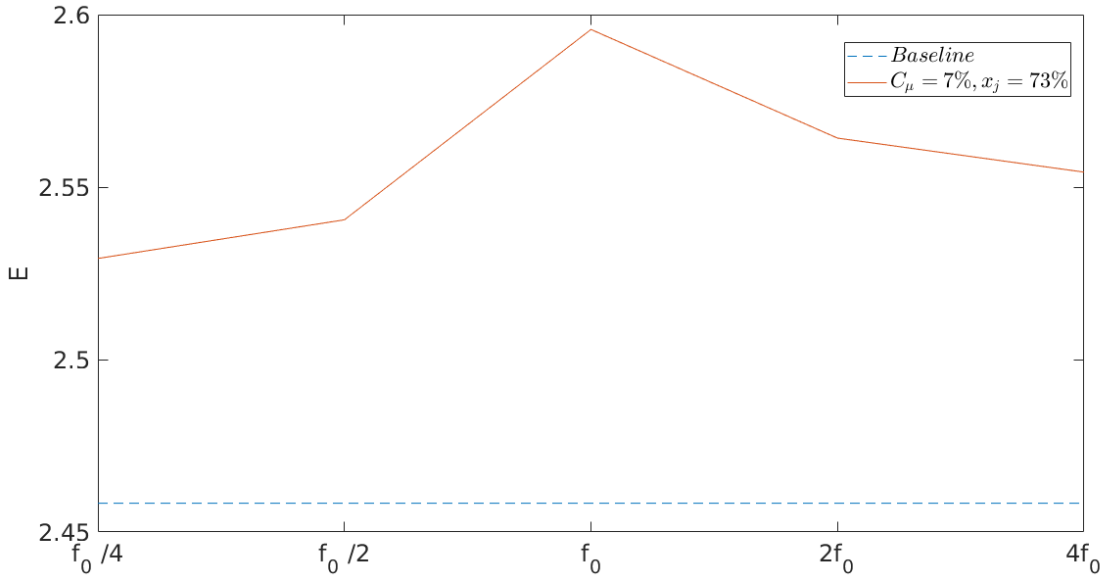

Figure 2.42: E variation with the frequency of the SWJ

b Amplitude

In the same way as in the frequency study, the jet's position has been set to a 73% of the chord, and the momentum coefficient is a 7%.

The amplitude of the oscillation of the output velocity has been modified in order to study its effect on the aerodynamic coefficients of the airfoil, from the nominal amplitude which was set to a 30%. Also, a zero amplitude (constant net mass flux) has been tested as in the previous section (2.3.4.1.), since this experiment has only been carried out with a $x_j = 30, 35, 40\%$.

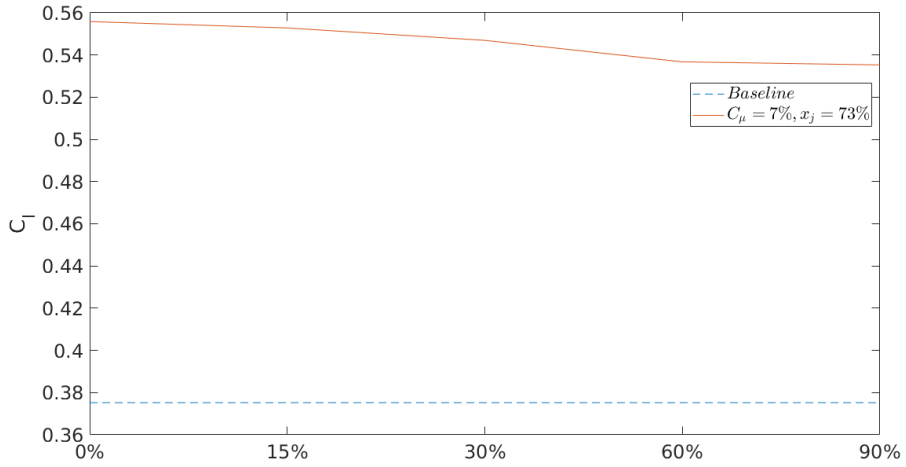

Figure 2.43: C_l variation with the amplitude of the SWJ

The lift coefficient maximizes its value when the output velocity of the sweeping jet is constant, that is, with constant net mass flux. It's important to mention that the plotted values in the figure 2.43 are the time-averaged values of lift coefficient. The output (temporal) signal of lift coefficient shows how on non-constant net mass flux there are peaks with higher C_l (see figure 2.44), which are produced when the boundary layer is not detached.

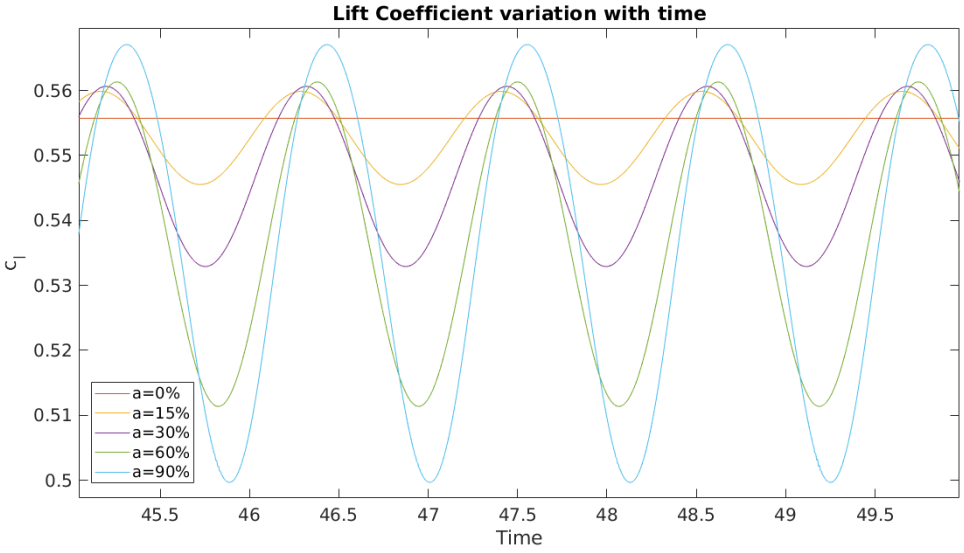

Figure 2.44: C_l variation with time

On the other hand, the figures 2.45 and 2.46 make the evidence that the maximum-lift coefficient configuration does not coincide with the optimal in terms of aerodynamic efficiency. The drag coefficient decreases significantly when increasing the amplitude of the jet, while the decrease of the lift coefficient is not so remarkable, making the aerodynamic

efficiency greater as the amplitude increases. Finally, the tables b and b expose the final quantitative results of the amplitude and frequency study.

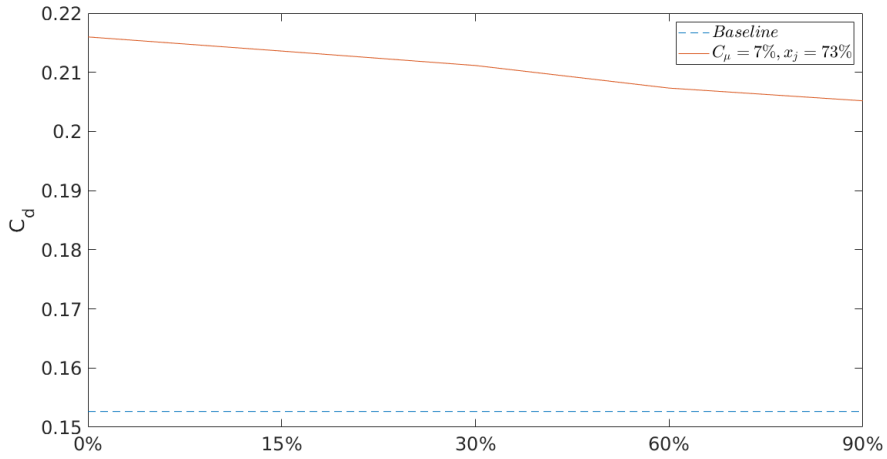

Figure 2.45: C_d variation with the amplitude of the SWJ

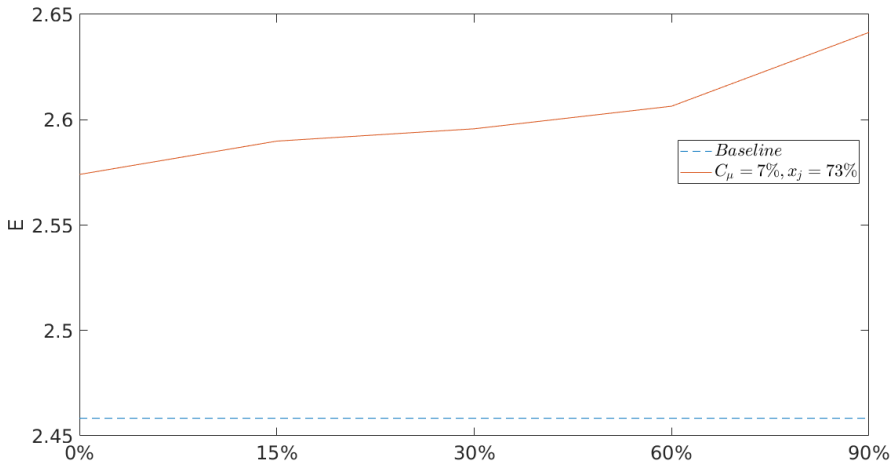

Figure 2.46: E variation with the amplitude of the SWJ

	Baseline	A=0%	A=15%	A=30%	A=60%	A=90%
$\overline{C_l}$	0.3752	0.5558	0.5528	0.5469	0.5368	0.5353
$\overline{C_d}$	0.1527	0.2160	0.2136	0.2112	0.2073	0.2052
$\overline{E}$	2.4583	2.5740	2.5898	2.5957	2.6064	2.6414

Table 2.7: Aerodynamic characteristics with the variation of amplitude

	Baseline	$f = f_0/4$	$f = f_0/2$	$f = f_0$	$f = 2f_0$	$f = 4f_0$
$\overline{C_l}$	0.3752	0.5246	0.5280	0.5469	0.5298	0.5294
$\overline{C_d}$	0.1527	0.2078	0.2082	0.2112	0.2069	0.2075
$\overline{E}$	2.4583	2.5293	2.5405	2.5957	2.5642	2.5543

Table 2.8: Aerodynamic characteristics with the variation of frequency

2.4. Quasi-3D study

2.4.1. Experiment description

The objective of this section is to analyze the three dimensionality that might be expected in for the baseline case. On a finite wing, multiple sweeping jets must be installed in the span-wise direction, ensuring that the 2D effect found on the previous section remains similar in 3D, as shown in the figure 2.47. It has been found that there is a strong relationship between the distance separating consecutive jets and their ability to control flow.[2]

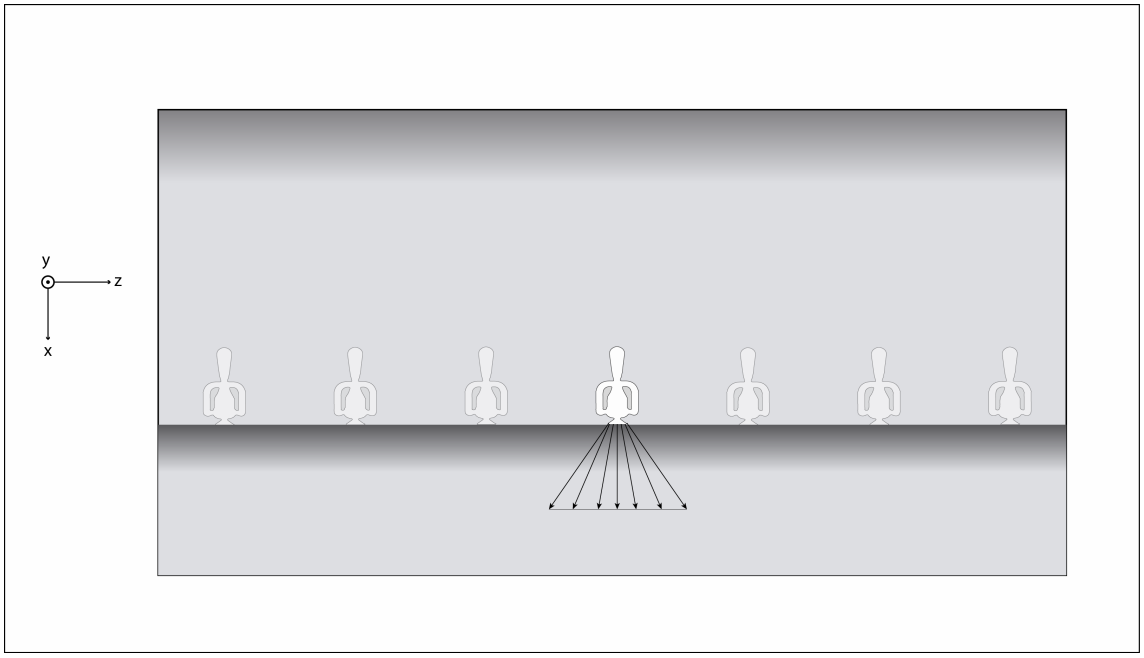

Figure 2.47: Jet positioning sketch

The 3D simulations with CFD are extremely costly in computational time, since the mesh elements is multiplied by the number of elements in the span-wise direction. For example, the 2D simulations performed in this project have required a computational time of 10h each. Setting the z-direction resolution the tenth of the x-direction's, if a span of 1 chord was chosen, the number of points along z direction would be the order of 10^2, increasing the computation time from 10h to 10^3h (more than 40 days), which cannot be assumed in this study.

Nevertheless, when in a three-dimensional domain one direction is homogeneous and the boundary conditions are periodic, a *"quasi-3D"* (or*"2.5D"*) can be applied. In this case, the homogeneous direction (z) is represented by a Fourier expansion. All field variables can be expanded in terms of a Fourier basis $e^{i\beta m_z}$ with M_z Fourier modes.[15] The variables can be represented as follows:

$$\begin{bmatrix} u(x,y,z,t) \\ v(x,y,z,t) \\ w(x,y,z,t) \\ p(x,y,z,t) \end{bmatrix} = \sum_{m_z=0}^{M_z-1} \begin{bmatrix} u_{m_z}(x,y,t) \\ v_{m_z}(x,y,t) \\ w_{m_z}(x,y,t) \\ p_{m_z}(x,y,t) \end{bmatrix} e^{i\beta m_z z} \tag{2.13}$$

This method decreases the computational time, and is accurate enough for the purpose of this study. Fourier expansions of sufficient resolution can be as accurate as needed for a problem that has a periodic direction. In the case of infinite wing approximation is usually a fairly good approximation for BL's detachment related phenomena.

Moreover, Nektar++ allows the user to extract the energy of the Fourier modes m_z and study their evolution with time. Concretely, if four Fourier modes are used (± 0, ± 1), the mode 0 represents the 2D solution (simply substituting $m_z = 0$ in the equation 2.13) and the mode 1 represents a crude description of the 3D dependence of the solution. It provides the means to compute the instabilities exactly if the linear stability of a 2D flow is considered.

This is very useful for the purpose of this study: the stability of the z-direction can be assessed by studying the Fourier mode 1 variation with time. A small (compared to the *2D*) impulse is set as an initial condition for w, and u, v, p initial conditions are extracted from a converged solution of a *2D* simulation. For a given L_z, the energy in transient solution of the Fourier mode 1 will increase or decrease showing the stability of the system at the given L_z.

In this regard, several computations varying L_z will be carried out in order to asses the stability of the three-dimensional solution. An unstable solution proposes that the perturbation in the z-direction grows with a wave number $\beta = 2\pi/L_z$, and β is directly related to the optimal span-wise spacing of the actuators: the z-component of the sweeping-jet is expected to interact with the growing perturbation mitigating it.

Summarizing, this section is actually a preliminary study of a $3D$ simulation: the distance between consecutive jets is studied, but the resulting aerodynamic characteristics of a $3D$ wing is not studied.

2.4.2. Simulations and results

The three-dimensional component, as explained previously, may grow in certain conditions: it depends on the distance between the vertical planes where the periodic boundary conditions are applied. The wave number of a perturbation which may grow is expected to be in proportion to the diameter of naturally shed two dimensional vortices of the studied airfoil, whose size is approximately a 15% of the chord. Several L_z will be tested, and the time-series of the modal energy will be analyzed.

The results from the mentioned calculations show that, as expected, the energy of the Mode 1 tends to stabilize with time (the stabilization time depends on the value of L_z). The interval of interest corresponds to that of the leading linear instability exponential growth or decay, i.e. after the initial transients and before nonlinear saturation due to modes interaction.

The calculations having very small L_z have not experimented a growth in the energy of the mode 1, due to the fact that the perturbation is not able to grow in that small domain (see the figure 2.48: $L_z = 0.01, 0.05$). When the span becomes greater, the energy of the mode 1 grows before stabilize: the figure 2.48 ($L_z = 0.1$), shows a quasi-linear growth for $100.05 < t < 100.2$. The first growing wave number has been found, being $\beta = 2\pi/L_z = 20\pi$.

The tendency of the growth of the mode 1 energy is to grow slower. In fact, what the images show is the transient part of the signal, which is already present due to the elevated stabilization time with a bigger L_z.

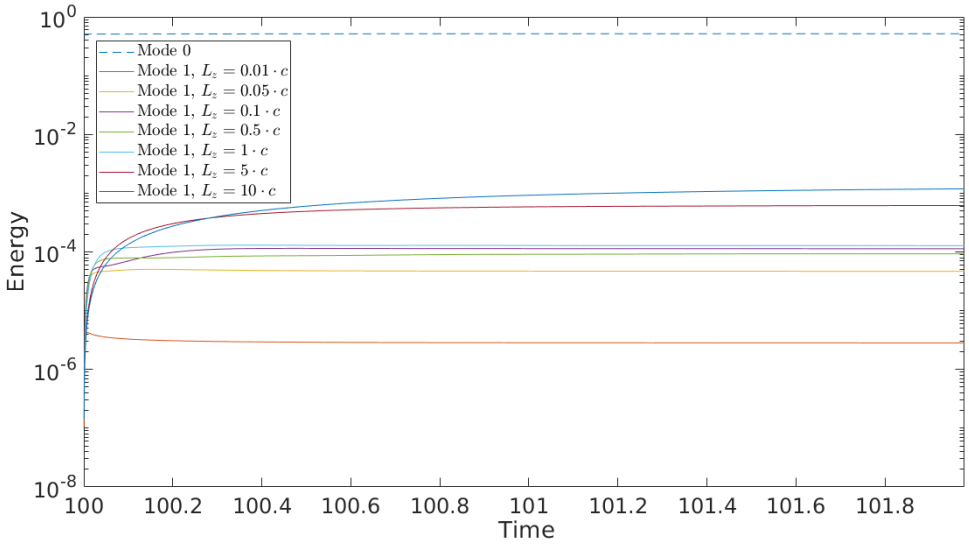

Figure 2.48: Modal energy time-series for several L_z

There is an unsuspected quick grow of the modal energy, a very fast transient, for the mode 1. Probably it's due to instabilities on the boundary regions, such as the inlet or the outlet, because there are no evidences of perturbations near the airfoil. The extremely quick growth of all tried span-wise perturbations is unexpected, probably due to the boundary conditions treatment when switching from 2D to quasi-3D. This results are not completely trusted, and they are left also for future work.

Concluding, the flux appears to be bi-dimensional for a L_z lower than 10% of the chord, and strong $3D$ effects appear when L_z is greater. Then, the minimum distance between consecutive SWJ devices should be the 10% or less of the chord, in order to maintain the studied behaviour of the flow in the previous sections, when only a $2D$ flow was studied.

CONCLUSIONS AND FUTURE WORK

The sweeping jet has been found to be effective as an active flow control method being applied to an airfoil without an hyper sustentation device, such as flaps. Other studies showed the benefits of including a sweeping jet on an airfoil before a flap, where the boundary layer detached, and this study has concluded on the idea that a sweeping jet is effective when applied to an airfoil at high angle of attack.

The first configuration of the jet, located on the upper surface of the airfoil and pointing upwards in the Y direction has been found to reduce drag in some conditions, setting a frequency double the natural vortex shedding frequency. Concretely, a frequency two times the vortex shedding frequency has made the drag coefficient reduce slightly, but in detriment of the lift coefficient which has been also reduced. The cause is the separation of the boundary layer: although the momentum coefficient of the sweeping jet has been set between a 0.06% and a 0.12%, it has been enough to cause the boundary layer to detach. Probably, it would have worked better with a zero net mass flux device, preventing boundary layer's separation but introducing the desired frequency.

The second configuration of the sweeping jet, pointing approximately tangential to the airfoil on the upper surface, has achieved the desired effect, which is the increase of the lift coefficient.

First, a constant net mass flux device, located near the boundary layer's detachment has been considered, and as the simulations have been performed in 2D, the oscillation of the jet has not been represented. In this case, the jet does not actually sweep, but injects a certain momentum to the boundary layer, which is also desirable. In this simulations, the lift coefficient has increased by a 15% approximately, but increasing the drag coefficient such that the aerodynamic efficiency has not been improved or it has even decreased. The wall shear stress plotted over the upper surface shows that the jet has been able to retard the boundary layer's separation, but not suppress it. Also, the pressure distribution over the airfoil has shown that the augment of suction on the upper surface has appeared before the jet, which has encouraged the idea of retarding the position of the jet until near the trailing edge.

Then, the second group of simulations have been carried out locating the sweeping jet between the 62% and the 82% of the chord, achieving the best results in terms of lift coefficient increase and also in aerodynamic efficiency. Also, a variation of the net mass flux has been simulated in order to introduce a frequency in the domain, with the hope of reduce the drag coefficient as happened with the first configuration of the sweeping jet.

The streamlines show that the sweeping jet located after the boundary layer's detachment has been able to reattach the flow at the jet's location, producing small recirculations before the BL's separation and the location of the jet.

Also, it has been found that the lower surface of the airfoil has experimented an increase of the pressure, hence it also contributes to the overall lift.

The best location of the sweeping jet has been found to depend on the momentum coefficient of it. A higher momentum coefficient makes a bigger pressure gradient, being able to reattach boundary layer from a further distance. This makes that the optimal position of the sweeping jet in order to achieve an optimal lift coefficient directly depends on the jet's

momentum coefficient.

Finally, an study of the amplitude and frequency of the mass flux variation of the sweeping jet has been carried out, finding that the zero-amplitude (constant net mass flux) SWJ gives the higher lift coefficient to the airfoil. Moreover, this is the most realistic scenario since the studied device has a constant net mass flux.

In these simulations, an increase near a 50% of the lift coefficient has been achieved, but also increasing the drag coefficient by approximately a 30%. This results are considered very positive since, as it has been explained in the introduction, the objective of this project is to find that the inclusion of a sweeping jet on the airfoil may have similar benefits as the inclusion of a hyper sustentation device, which also increases drag. It's important to mention that in actuations such as landing (where the flaps are activated in order to increase the lift coefficient) the drag is also increased and even considered a benefit.

Despite this, as future work, the drag reduction may be a good point where to focus. The drag coefficient has been found to be highly increased by the viscous terms, due to the high velocities near the surface generated by the sweeping jet. On the other hand, the pressure drag has decreased by a 50% approximately by eliminating the boundary layer's detachment, which produces low pressures near the trailing edge driving into drag augments.

Then, another field to investigate is the momentum coefficient of the sweeping jet. Probably, a momentum coefficient decrease would imply viscous drag reduction, and if similar results in lift coefficient were found with lower momentum coefficients, the drag would decrease (by the viscous part) and then the aerodynamic efficiency would increase making the sweeping jet a suitable option for take-off too. Also, a decrease of the momentum coefficient might be necessary at higher Reynolds number: with the considered jet slot size, the velocity at the nozzle of the jet is near four times the up-stream velocity. Considering this fact at higher Reynolds numbers, the jet speed could approach sonic conditions.

Finally, it has been proven that the distance between the boundary layer's detachment and the jet's location is crucial, at a given momentum coefficient. The jet must be able to reattach the boundary layer, and there is a "maximum" distance between both points, coinciding the maximum distance with the optimal. Since the BL's detachment, at a given Reynolds and Mach, depends on the angle of attack, the optimal position for the jet does too: obviously, the optimal location found in this project corresponds to the studied angle of attack: 9^o. Then, the $C_l(\alpha)$ curve should be parameterized for every jet's location, or even be considered as $C_l(\alpha, x_j)$. This may imply a big deal when installing the sweeping jet on a wing, since its location on the upper surface is determinant on the performances of an aircraft, but taking into account that the sweeping jet should only be activated in actuations such as take-off and landing, the operational angle of attack on these actuation should be considered in order to allocate the jet for each aircraft.

Concluding on the $3D$ study, the results show that instabilities in the z-direction grow when L_z is greater than a 10% of the chord, meaning that the flux is near bi-dimensional at lower values of L_z, that is, shorter distance between the applied periodic boundary conditions. Extrapolating this to the aim of the study, it can be concluded that the minimum distance between consecutive devices should be smaller than a 10% of the chord at the given conditions.

BIBLIOGRAPHY

[1] LaTunia, P. M., Koklu, M. “Active Flow Control Using Sweeping Jet Actuators on a Semi-Span Wing Model”. *54th AIAA Aerospace Sciences Meeting*. AIAA SciTech Forum, (AIAA 2016-1817). 3, 4, 5

[2] Andino, M. Y., Lin, J. C., Washburn, A. E., Whalen, E. A., Graff, E. C., and Wygnanski, I. J. “Flow Separation Control on a Full-Scale Vertical Tail Model using Sweeping Jet Actuators”. *53rd AIAA Aerospace Sciences Meeting*. Reston, Virginia, Jan. 2015 3, 4, 56

[3] Claudio G Canuto, M. Yousuff Hussaini, Alfio Quarteroni, Thomas A. Zang - Spectral methods evolution to complex geometries and applications to fluid dynamics (2007, Springer) 9

[4] LaTunia, P. M., Koklu, M. “Active Flow Separation Control on a NACA 0015 Wing using Fluidic Actuators”. *7th AIAA Flow Control Conference*. Atlanta, GA. 16-20 June 2014 3

[5] Koklu, M, Owens, L. R. “Flow Separation Control Over a Ramp Using Sweeping Jet Actuators”. *7th AIAA Flow Control Conference*. Atlanta, GA. 16-20 June 2014 3, 5

[6] Minelli, G., et al. “DEVELOPMENT OF ACTIVE FLOW CONTROL FOR TRUCKS”. *3rd Thermal and Fluids Engineering Conference (TFEC)*. Fort Lauderdale, FL, USA. March 4–7, 2018. 3

[7] Ghouila-Houri, C., et al. “High temperature gradient calorimetric wall shear stress micro-sensor for flow separation detection” *University Lille, CNRS* 9 August 2017. ix, 3

[8] Vatsa, V. N., Koklu, M.,Wygnanski, I. L. “Numerical Simulation of Fluidic Actuators for Flow Control Applications”. *6th AIAA Flow Control Conference*. New Orleans, Louisiana. 25-28 June 2012 4

[9] Koklu, M., LaTunia, P. M. “Sweeping Jet Actuator in a Quiescent Environment”. *43rd Fluid Dynamics Conference*. San Diego, CA. 24-27 June, 2013. 4

[10] Raman, G., Raghu, S., “Cavity Resonance Suppression Using Miniature Fluidic Oscillators”. *AIAA Journal*, **42**(12), December 2004, pp. 2608-2611. ix, 5

[11] Woszidlo, R., Wygnanski, I. “Parameters Governing Separation Control with Sweeping Jet Actuators”. *29th AIAA Applied Aerodynamics Conference*. Honolulu, Hawaii. 27-30 June 2011. 5

[12] SJ Sherwin and G Em Karniadakis. “Tetrahedral finite elements: Algorithms and flow simulations.” *Journal of Computational Physics*, 124(1):14–45, 1996.

[13] Jan S Hesthaven and Tim Warburton. “Nodal high-order methods on unstructured grids: I. time-domain solution of maxwell’s equations.” *Journal of Computational Physics*, 181(1):186–221, 2002. 10

[14] P-E Bernard, J-F Remacle, Richard Comblen, Vincent Legat, and Koen Hillewaert. “High-order discontinuous galerkin schemes on general 2d manifolds applied to the shallow water equations.” *Journal of Computational Physics*, 228(17):6514–6535, 2009. 10

[15] Karniadakis, G. E. “Spectral element-Fourier methods for incompressible turbulent flows”. *Computer methods in applied mechanics and engineering*. Princeton, U.S.A, 1989. 10

[16] G. E. Karniadakis, M. Israeli, and S. A. Orszag. “High-order splitting methods for the incompressible Navier–Stokes equations”. 97(2):414–443, 1991. 56

[17] S. Dong, G. E. Karniadakis, and C. Chryssostomidis. “A robust and accurate outflow boundary condition for incompressible flow simulations on severely-truncated unbounded domains.” *Journal of Computational Physics*, 261:95–136, 2014. 8

[18] https://www.nektar.info/ 8

[19] Nektar++: Spectral/hp Element Framework Department of Aeronautics, Imperial College London, UK Scientific Computing and Imaging Institute, University of Utah, USA 12

[20] http://gmsh.info/ 10

APÈNDIXS

APPENDIX A. JET MESH ADAPTATION

A.1. Initial mesh development

In the beginning of this project, there was only a bare NACA012 airfoil that had to be recoded to mainstream the jet slot either in a normal stream-wise position and stream-wise/horizontal position. Both position needed lot of changes as the mesh follows a logical structured composition. Unlike typical unstructured mesh that have a more triangular mesh, this mesh has to keep all the proportions.

To achieve so, there was a background study on how was coded and how worked. As it is not the main conducting topic of the project, there's only the following list that the code follows to display the airfoil with its mesh:

1. Definition of the initial conditions and surfaces.

   (a) Firstly as all the codes, there is a definition of the size and proportions of the jet.

```
//+++++++++++++++++++++++++++++++++++++++++++++++++++++++++++//
// GEOMETRY PARAMETERS
//+++++++++++++++++++++++++++++++++++++++++++++++++++++++++++//

// CASE
aoa=9*Pi/180; // working AoA (guides wake direction)

// AIRFOIL
c=1; // chord
t=0.12; // max thickness (in % of chord)
m=0.00; // max camber (in % of chord)
p=0.4; // max camber position (in % of chord)
tetype=0; // trailing edge type: 0: sharp; 1: blunt (not implemented);
N=101; // number of points defining airfoil
```

   As seen above, there is the angle of attack definition (which keeps constant at 9 degrees along the whole study as mentioned), the chord size, the maximum thickness,camber and camber position in %. Finally there is also the number of the points that are actually defining this jet. The definition of the jet it's done through a fifth degree polynomial with the x axis acting as a mirror to fulfill the contour of the airfoil.

   Besides the jet, there are two other type of definitions of the code.

   (b) The mesh boundaries, that as the word itself says, it bound the limits of the control volume. It is defined with respect to the chord so it readjusts automatically each time there is a change in it. There is the near-wall, the midfield, the wake and the fringe sections. Those are referred to the chord and to the angle of attack in order to vary the size with more ease. In the following lines of code there is the parameters that were used initially for the first simulations.

   For example by looking at the wake it can be seen the angles to have a consistent mesh taking into account the airfoil position angle of attack.

```
// NEARWALL (defined as orthogonal distance from airfoil surface)
//Rnf=2*c; // radius
//tnwle=0.2*c; // near wall region thickness at leading edge (in chord
lengths)
//eu=1.0; au=1.0; // tu=tnwle*(1+au*(x/c)^eu) [au<0 for tangency with wake]
//el=1.0; al=1.0; // tl=tnwle*(1+al*(x/c)^el) [au<0 for tangncy with wake]
Rnf=0.5*c; anf=2*aoa/3;

// MIDFIELD (defined as orthogonal distance from airfoil surface)
Rmf=1.0*c; amf=aoa/3;

// WAKE
daoau=(2*aoa/3);//*Pi/180; // upper wake opening angle (angle_upper=aoa
+daoau)
daoauu=(3*aoa/4);//*Pi/180; // upper upper wake opening angle
(angle_upper=aoa+daoau)
daoal=(aoa/2);//*Pi/180; // lower wake opening angle (angle_lower=aoa-
daoal)
daoall=(2*aoa/3);//*Pi/180; // lower lower wake opening angle
(angle_lower=aoa-daoal)

// BOUNDARY
a=10*c;//10*c; // upstream dimensions from trailing edge (in chord lengths)
b=10*c;//10*c; // downstream dimensions from trailing edge (in chord
lengths)
NP=101; // number of points defining semi-circle
fr=-2*c; // fringe region length (<0 for no fringe region)
ajint=3*Pi/4;
```

(c) The mesh parameters. These are defined to determine how the user wants to determine the relations of mesh inside each surface. There are three main types, 0. equispaced, 1. progression and 2. bump.

Equispaced is as easy as it sound, all the mesh lines are equidistant among them. Progression means that when moving towards the chosen zone, the lines start to get narrow among them to stress a particular zone that should have more going on than others. Finally , bumps is the same as progression but instead of one side, in both directions.

```
// NEARFIELD REGION
ibuanf=ibuas;//1; // 0: equispaced; 1: Progression; 2: Bump
kbuanf=kbuas;//1.02; // Progression/Bump parameter
ibufnf=0; // 0: equispaced; 1: Progression; 2: Bump
kbufnf=1.00; // Progression/Bump parameter
iblanf=0;//1; // 0: equispaced; 1: Progression; 2: Bump
kblanf=0.00; // Progression/Bump parameter
iblfnf=0; // 0: equispaced; 1: Progression; 2: Bump
kblfnf=1.00; // Progression/Bump parameter

Puanf=Ph; // target polynomial order for upper nearfield +1 (=NUMMODES)
kutenf=1.0333; // wall-normal target progression ratio (virtual)
xfirstu=4e-4; // upper trailing edge first point distance
Pufnf=Ph;
```

2. Equations and math relations. Once all initial parameters are fixed, there is a section inside of the code that uses all kind of mathematical equations and little functions to construct and draw in some way the mesh. All these mathematical calculations have been written for each surface as depending on the position there ought be a certain shape. For instance, by looking at the farfield, midfield and nearfield in the beginning, there is a big semicircle where the air comes through. Those specific areas are defined with the respective mathematical solution.

3. Composition of transfinite lines Likewise a building is constructed, there is this part of the code where all the parameters are tide up and need to be organized. This is where the transfinite lines are involved.

   These lines are the individual lines that bound each of the surfaces implied defined using the fore results and computations regarding the initial data and math sections.

4. Composition of the line loops Once these transfinite lines are already defined and recognized by the code, a line loop is generated. Line loops are basically the union of all those individual lines, depending on which surface it's being defined. Thus, finally each line loop takes the shape of the sections of the defined surfaces.

5. Composition of the plane surfaces Having the line loops generated, it is possible to now create the plane surfaces that will define not only the contour but the surfaces throughout the whole mesh.

6. Composition of the physical surfaces Finally there is the physical surface step where the surfaces are actually converted to physical surfaces which later on will be used to impose the conditions, expansions, etc. required to obtain the most satisfying results of the simulations.

A.2. Normal stream wise jet mesh adaptation

Once the initial mesh was created and structured the upcoming step was to simulate it as shown in chapter 1 to compute the optimal mesh for the whole study. This was a very important step due to the saves on time and computer resources. Additionally , it is always nicer to have a bigger mesh with lot more points as it will result on a more reliable simulation. However maybe the savings on time are way more clever than having the best mesh (with not much of a difference).

Starting with this normal stream wise jet, there was a big modification in the upper side of the airfoil and in the respective above surfaces. As aforementioned, the jet implementation cannot only be found in the near field region as that would break the structure among the other surfaces. Thus, two lines were generated that go across from upper airfoil surface until the end of far field region. To accomplish this, some new math formulation was generated to subsequently define them as transfinite lines. In this step it was important to divide the upper side of the mesh: the near upper field, the mid upper field and the far upper field into nine new surfaces to be able not only to take into account the thinner mesh required for the jet but the jet's slot over the airfoil surface.

The following figure includes the lines of the code where the jet's location is defined. To generate the beginning and the end of the jet position new points had to be located. These points are the result of mathematical intersections and taking always into consideration the angle of the attack in which the airfoil is.

```
xuj0 = -c+xj-ytj*Sin(thj); yuj0 = ycj+ytj*Cos(thj);
xuj = xte0+(xuj0-xte0)*Cos(aoa)+(yuj0-yte0)*Sin(aoa);
yuj = yte0-(xuj0-xte0)*Sin(aoa)+(yuj0-yte0)*Cos(aoa);
ujP=newp; Point(ujP)={xuj,yuj,0}; // PUNTO CENTRAL DEL JET
Printf("aaaaaaaaa %g %g",xuj,yuj);
xuj0f = -c+xjf-ytjf*Sin(thjf); yuj0f = ycjf+ytjf*Cos(thjf);
xujf = xte0+(xuj0f-xte0)*Cos(aoa)+(yuj0f-yte0)*Sin(aoa);
yujf = yte0-(xuj0f-xte0)*Sin(aoa)+(yuj0f-yte0)*Cos(aoa);
ujPf=newp; Point(ujPf)={xujf,yujf,0}; // PUNTO ANTERIOR DEL JET

xuj0a = -c+xja-ytja*Sin(thja); yuj0a = ycja+ytja*Cos(thja);
xuja = xte0+(xuj0a-xte0)*Cos(aoa)+(yuj0a-yte0)*Sin(aoa);
yuja = yte0-(xuj0a-xte0)*Sin(aoa)+(yuj0a-yte0)*Cos(aoa);
ujPa=newp; Point(ujPa)={xuja,yuja,0}; // PUNTO POSTERIOR DEL JET

xlj0 = -c+xj+ytj*Sin(thj); ylj0 = ycj-ytj*Cos(thj);
xlj = xte0+(xlj0-xte0)*Cos(aoa)+(ylj0-yte0)*Sin(aoa);
ylj = yte0-(xlj0-xte0)*Sin(aoa)+(ylj0-yte0)*Cos(aoa);
ljP=newp; Point(ljP)={xlj,ylj,0}; // PUNTO DEL JET INFERIOR


dycdxte = 2*m/(p-1); dytdxte = 5*t*(a0/2+a1+2*a2+3*a3+4*a4);
dycdxle = 2*m/p; thnfle=Atan(dycdxle)+Pi/2;
```

Figure A.1: Location of the jet code

There are 4 points defined in the figure , the central jet point, the fore jet point, the after point and the below jet point. Once all the points are defined, this points are saved to used them for the surfaces.

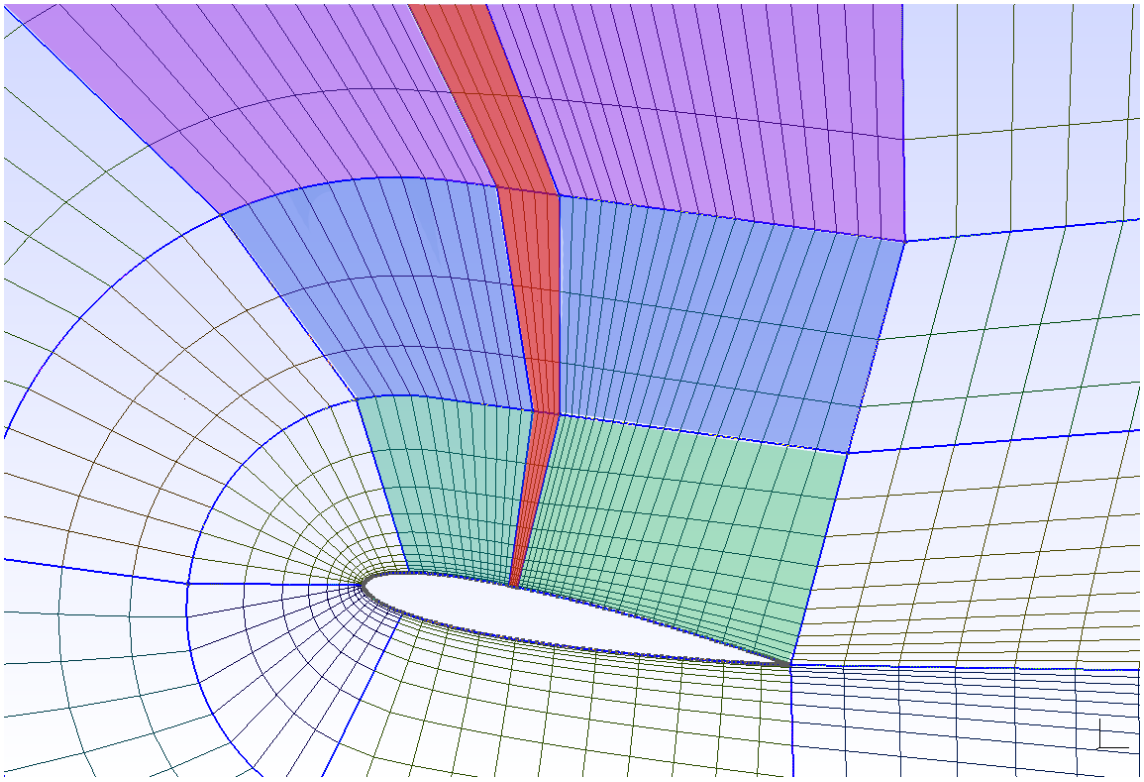

Figure A.2: Distribution of upper surface with normal stream wise jet

The above figure shows in a qualitative way how the mesh looks like in the code. The green part is the near upper surface that once was unified. Likewise for the rest of the

surfaces, mid field has the blue color and upper (which is not fully shown in the figure) has the violet color. The jet now goes through all these surfaces what makes nine line loops, nine surfaces instead of the three that were before implementing the jet. With the presence of these new surfaces, a tiny groove appears in the upper airfoil surface. This is the exact point were the jet is relocated to eject the oscillating flow.

The dynamics and the equations of the jet flow are already described in chapter 2.2.4., however, the implementation of it was done through the jetconditions file to fix the variables and indicate to each of the surfaces the boundary conditions.

A.2.1. Jet conditions file

A.2.1.1. Parameters of the jet

Starting off with the parameters displayed in the below screenshoot of the code used, the first three are referred to the proper simulation. Basically, they define the time of the simulation and the quantity of checks Nektar will print to know the evolution of the aerodynamic forces along the entire test. Other key parameters are the external conditions were the simulation took place such as Reynolds number , the angle of the airfoil, the actual jet position and in the lower parameters the pre-calculated values that are introduced in the jet movement equations.

```
<PARAMETERS>
  <P> TimeStep      = 0.0005    </P>
  <P> NumSteps      = 500000    </P>
  <P> IO_CheckSteps = 5000     </P>
  <P> IO_InfoSteps  = 100       </P>
  <!--<P> SubStepCFL    = 0.5       </P>-->
  <!--<P> MinSubSteps   = 4         </P>-->
  <!--<P> MaxSubSteps   = 100       </P>-->
  <P> Re            = 1000      </P>
  <P> Kinvis        = 1./Re     </P>
  <P> aoa           = 09        </P>
  <P> OutflowBC_theta  = 1.0    </P>
  <P> OutflowBC_alpha1 = 1.0    </P>
  <P> OutflowBC_alpha2 = 0.0    </P>
  <P> D0            = 1.0       </P>
  <P> Kinvis        = 1./Re     </P>
  <P> t1=0.12                    </P>
  <P> c=1                    </P>
  <P> a0=0.2969                 </P>
  <P> a1=-0.1260                </P>
  <P> a2=-0.3516                </P>
  <P> a3=0.2843                 </P>
  <P> a4=-0.1036                </P>
  <P> xjet=0.34                 </P>
  <P> pi=3.141592653589793238               </P>
  <P> aoa           = 9*pi/180 </P>
  <P> h=5*t1*c*(a0*sqrt(xjet/c)+a1*(xjet/c)+a2*(xjet/c)^2+a3*(xjet/c)^3+a4*(xjet/c)^4) </P>
  <P> dytdxja =5*t1*c*(a0/(2*sqrt(xjet/c))+a1+2*a2*(xjet/c)+3*a3*(xjet/c)^2+4*a4*(xjet/c)^3) </P>
  <P> beta=-atan(dytdxja)        </P>
  <P> cmu=0.012       </P>
  <P> b=0.02        </P>
  <P> vj=sqrt(cmu/(2*b))        </P>
  <P> A=-6*vj/(b*b)        </P>
  <P> B=-A*b        </P>
  <P> fjet=500        </P>
  <P> thetam=45*pi/180        </P>
  <P> w=2*pi*fjet        </P>
</PARAMETERS>
```

Figure A.3: Parameters of the jet

A.2.1.2. Expansions jet conditions file

One important section of the jet conditions file is the expansions used. These are the connection between the mesh and the conditions that are applied to the respective zones. In

order to set a relation among them, composites are defined. The following shows the number of nodes that each expansion has and these are the numbers that have been varied in chapter 1 and section 1.9.3.. The higher the number of the expansion, the more nodes Nektar has to solve Navier Stokes equations, thus higher definition. Certainly, with the mesh divided due to the added jet, those surfaces must always have a higher expansion as that is a critical point to measure and analyze the aerodynamics.

```
<EXPANSIONS>
  <E COMPOSITE="C[9]" NUMMODES="4" TYPE="MODIFIED" FIELDS="u,v,p" /> <!-- FarField -->
  <E COMPOSITE="C[10]" NUMMODES="6" TYPE="MODIFIED" FIELDS="u,v,p" /> <!-- UpperMidFieldWake -->
  <E COMPOSITE="C[11]" NUMMODES="6" TYPE="MODIFIED" FIELDS="u,v,p" /> <!-- MidFieldExceptUpperWake -->
  <E COMPOSITE="C[12]" NUMMODES="8" TYPE="MODIFIED" FIELDS="u,v,p" />  <!-- UpperNearField -->
  <E COMPOSITE="C[13]" NUMMODES="8" TYPE="MODIFIED" FIELDS="u,v,p" />  <!-- LowerNearField -->
  <E COMPOSITE="C[14]" NUMMODES="8" TYPE="MODIFIED" FIELDS="u,v,p" />  <!-- Wake -->
  <!--<E COMPOSITE="C[7-12]" NUMMODES="4" TYPE="MODIFIED" FIELDS="u,v,p" />--> <!-- All -->
  <!--<E COMPOSITE="C[0]" NUMMODES="7" FIELDS="u,v,p" TYPE="GLL_LAGRANGE" />-->
  <!--<E COMPOSITE="C[0]" NUMMODES="7" FIELDS="u,v,p" TYPE="GLL_LAGRANGE_SEM" />-->
</EXPANSIONS>
```

Figure A.4: Expansions of jet condtions file

A.2.1.3. Regions of the jet

All the regions correspond to the surfaces and composites generated before. For instance, in the case of this normal stream wise jet, the following boundary regions were generated:

```
<BOUNDARYREGIONS>
  <B ID="0"> C[1] </B> <!-- Inlet -->
  <B ID="1"> C[2] </B> <!-- Outlet -->
  <B ID="2"> C[3] </B> <!-- Upper Surface before jet -->
  <B ID="3"> C[4] </B> <!-- Jet -->
  <B ID="4"> C[5] </B> <!-- Upper Surface after jet -->
  <B ID="5"> C[6] </B> <!-- Lower Surface -->
  <B ID="6"> C[7] </B> <!-- Upper Boundary -->
  <B ID="7"> C[8] </B> <!-- Lower Boundary -->
</BOUNDARYREGIONS>
```

Figure A.5: Boundary regions

The most important regions that need to have conditions different than zero, are the inlet which has the air coming through:

```
<BOUNDARYCONDITIONS>
  <REGION REF="0">
    <D VAR="u" VALUE="1" />
    <D VAR="v" VALUE="0" />
    <N VAR="p" USERDEFINEDTYPE="H" VALUE="0"/> <!--<D VAR="p" VALUE="0"/>-->
  </REGION>
  <REGION REF="1">
    <R VAR="u" USERDEFINEDTYPE="HOutflow" VALUE="0" PRIMCOEFF="D0/TimeStep" /> <!--<N VAR="u" VALUE="0" />-->
    <R VAR="v" USERDEFINEDTYPE="HOutflow" VALUE="0" PRIMCOEFF="D0/TimeStep" /> <!--<N VAR="v" VALUE="0" />-->
    <R VAR="p" USERDEFINEDTYPE="HOutflow" VALUE="0" PRIMCOEFF="1.0/(D0*Kinvis)" /> <!--<D VAR="p" USERDEFINEDTYPE="H" VALUE="0" />--> <!--<D
VAR="p" VALUE="0"/>-->
  </REGION>
```

Figure A.6: Boundary conditions of the jet

These two lines of code shown in Figure A.7 are the equations that describe the movement of the jet for the three variables of velocity: u,v and w. Inside of each the angle of attack is already considered. The shown letters are indeed pre-established values over the parameters section.

```
<REGION REF="3">
  <D VAR="u" USERDEFINEDTYPE="TimeDependent" VALUE="(A*((x-h*sin(aoa))/cos(aoa)+c-(xjet-b/2))^2+B*((x-h*sin(aoa))/cos(aoa)+c-(xjet-b/2)))*sin(beta
+aoa)+((A*((x-h*sin(aoa))/cos(aoa)+c-(xjet-b/2))^2+B*((x-h*sin(aoa))/cos(aoa)+c-(xjet-b/2)))*sin(atan(thetam*sin(w*t))))*cos(beta+aoa)" />
  <D VAR="v" USERDEFINEDTYPE="TimeDependent" VALUE="(A*((x-h*sin(aoa))/cos(aoa)+c-(xjet-b/2))^2+B*((x-h*sin(aoa))/cos(aoa)+c-(xjet-b/2)))*cos(beta
+aoa)-((A*((x-h*sin(aoa))/cos(aoa)+c-(xjet-b/2))^2+B*((x-h*sin(aoa))/cos(aoa)+c-(xjet-b/2)))*sin(atan(thetam*sin(w*t))))*sin(beta+aoa)" />
  <N VAR="p" USERDEFINEDTYPE="H" VALUE="0" />
</REGION>
```

Figure A.7: Jet surface conditions inside jetconditions file

The rest of the regions are equal to zero according to boundary conditions of boundary layer all around the airfoil.

```
<REGION REF="4">
  <D VAR="u" VALUE="0" />
  <D VAR="v" VALUE="0" />
  <N VAR="p" USERDEFINEDTYPE="H" VALUE="0" />
</REGION>
<REGION REF="5">
  <D VAR="u" VALUE="0" />
  <D VAR="v" VALUE="0" />
  <N VAR="p" USERDEFINEDTYPE="H" VALUE="0" />
</REGION>
<REGION REF="6">
  <N VAR="u" VALUE="0" />
  <D VAR="v" VALUE="0" />
  <N VAR="p" USERDEFINEDTYPE="H" VALUE="0" />
</REGION>
<REGION REF="7">
  <N VAR="u" VALUE="0" />
  <D VAR="v" VALUE="0" />
  <N VAR="p" USERDEFINEDTYPE="H" VALUE="0" />
</REGION>
```

Figure A.8: Rest of surface conditions inside the jetconditiosn file

A.3. Stream-wise jet mesh development

Switching to the stream-wise jet whom results are the best ones, the procedures to define the mesh and the boundary conditions are genuinely similar. Nevertheless, the idea behind the making is harder in this case.

In contrast to the 'vertical' lines of the normal stream-wise jet, now the surface over the airfoil had to be halfway crossed due to the jet situation along the upper surface. In addition to that, there wasn't only the need to cross the surface above the wing but the rest of the wake plus the fringe section to keep the equilibrium and structure among the sections.

Going even further back, there is a problem with the jet slot for this case as is not as easy as seizing the tiny section generated by the jet. In particularly, now the jet is divided into three new lines that break the initial geometry of the wing to locate the exit of the flow.

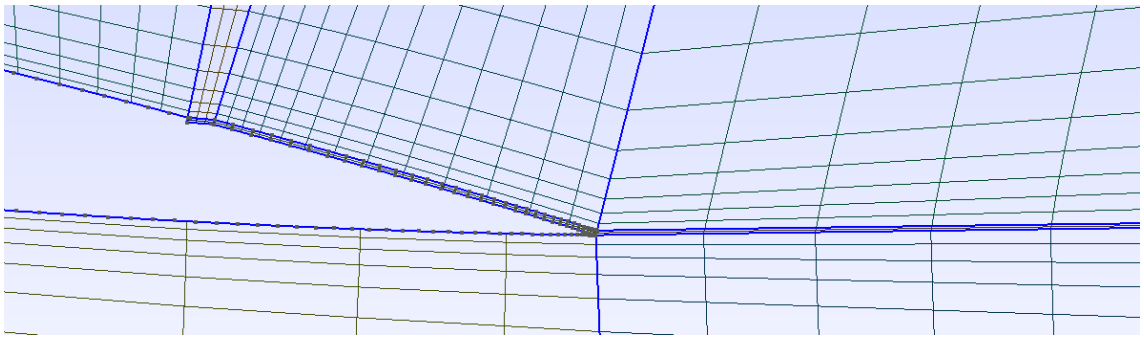

Figure A.9: Mesh solution for the jet's slot

A.3.0.1. Designing the jet slot

Considering that the current stream-wise jet is indeed flowing as the actual air flow and to avoid any notch sticking out and breaking the aerodynamics, the slot was made inwards instead of outwards. The trick here is to avoid any complex geometry as that could lead to problems for the solver and at the same time, providing the most horizontal position of the slot exit to disrupt as little as possible the air flow that passe over it.

The labour to fix not only the jet but its mesh is quite tedious as it has to balance the rest of the mesh by following the curvature of the airfoil in the exact way. To attain this configuration the following code has been used to copy the points of the airfoil and place them over a certain distance previously studied:

```
jetpos=0.73;
hjet=0.003*c;
anglejet=80;
Njv=4;
Njh=3;

xjet = c*(jetpos);
yjet = 5*t*c*(a0*Sqrt(xjet/c)+a1*(xjet/c)+a2*(xjet/c)^2+a3*(xjet/c)^3+a4*
(xjet/c)^4);
dytdxja = 5*t*(a0/(2*Sqrt(xjet/c))+a1+2*a2*(xjet/c)+3*a3*(xjet/c)^2+4*a4*
(xjet/c)^3);

xuj0 = -c+xjet;
yuj0 = yjet;
xuj = xte0+(xuj0-xte0)*Cos(aoa)+(yuj0-yte0)*Sin(aoa);
yuj = yte0-(xuj0-xte0)*Sin(aoa)+(yuj0-yte0)*Cos(aoa);

xjetaoa=xuj;
yjetaoa=yuj;
gamma=-Atan(dytdxja)+aoa;

delta=anglejet*Pi/180;
m1=Tan(Pi-gamma-delta);

n1=yjetaoa-m1*xjetaoa;
la=(1/m1^2+1);
lb=(-2*xjetaoa/m1-2*n1/m1^2-2*yjetaoa);
lc=xjetaoa^2+2*xjetaoa*n1/m1+n1^2/m1^2+yjetaoa^2-hjet^2;

y001=(-lb+Sqrt(lb^2-4*la*lc))/(2*la);
y002=(-lb-Sqrt(lb^2-4*la*lc))/(2*la);

If (y001<y002)
        x00=(y001-n1)/m1;
        y00=y001;
Else
        x00=(y002-n1)/m1;
        y00=y002;
EndIf

nuevooo=newp; Point(nuevooo)={x00,y00,0};
ujPf=newp; Point(ujPf)={xjetaoa,yjetaoa,0};
vnewjet=newl; Line(vnewjet)={ujPf,nuevooo};
```

Figure A.10: Code delivered to Gmsh to locate the jet slot

This code shown in Figure A.17 is the one used to find the right angle and position with respect to the geometry of the NACA. It mainly searches the intersection with some mathematical expressions and then save the point to use it as follows:

```
x00h=c+(x00)*Cos(aoa)-(y00)*Sin(aoa);
y00h=(x00)*Sin(aoa)+(y00)*Cos(aoa);

m1h=(yjet-y00h)/(xjet-x00h);

m2h=-1/m1h;
n2h=y00h-x00h*m2h;

xguess=jetpos;

For i In {0 : 10}
        xguess=xguess-(5*t*c*(a0*Sqrt(xguess/c)+a1*(xguess/c)+a2*(xguess/
c)^2+a3*(xguess/c)^3+a4*(xguess/c)^4)-m2h*xguess-n2h)/(5*t*(a0/(2*Sqrt
(xguess/c))+a1+2*a2*(xguess/c)+3*a3*(xguess/c)^2+4*a4*(xguess/c)^3)-m2h);
        Printf("aa %g",xguess);
EndFor

xjet2=xguess;
yjet2=5*t*c*(a0*Sqrt(xjet2/c)+a1*(xjet2/c)+a2*(xjet2/c)^2+a3*(xjet2/c)^3
+a4*(xjet2/c)^4);

xuj0 = -c+xjet2;
yuj0 = yjet2;
xuj = xte0+(xuj0-xte0)*Cos(aoa)+(yuj0-yte0)*Sin(aoa);
yuj = yte0-(xuj0-xte0)*Sin(aoa)+(yuj0-yte0)*Cos(aoa);

xjet2aoa=xuj;
yjet2aoa=yuj;

ujPa=newp; Point(ujPa)={xjet2aoa,yjet2aoa,0};
ljetdown=newl; Line(ljetdown)={nuevooo,ujPa};
```

Figure A.11: Second part of the location to locate the jet slot in Gmsh.

The above code has a loop that from some referenced points, it paint the points that were generated of the airfoil upwards to prepare for the mesh generation.

Once the jet has its new points defined and well-located, it is time to unify them and give them their own function with respect to the mesh generation. The following section explains how the mesh has been done and how works.

A.3.0.2. Mesh of the stream-wise jet

The figure A.12 shows analogously as the normal stream-wise jet, how the mesh is structured. There are some numbers to reference to the text: Number 1 is the little opening wall for the jet slot. There, the conditions are the ones of the jet flow which are described right after this section. Regarding number 2, it can be found part of the upper surface of the airfoil. Number 3 is the aforementioned correction of the mesh to hold the structure and organization. Eventually, there is number 4 that basically shows that the further surfaces of wake and fringe also should include the tiny mesh generated by the jet in order to maintain the lines over the whole mesh so Nektar can find all the nodes correctly and compute the solution for each.

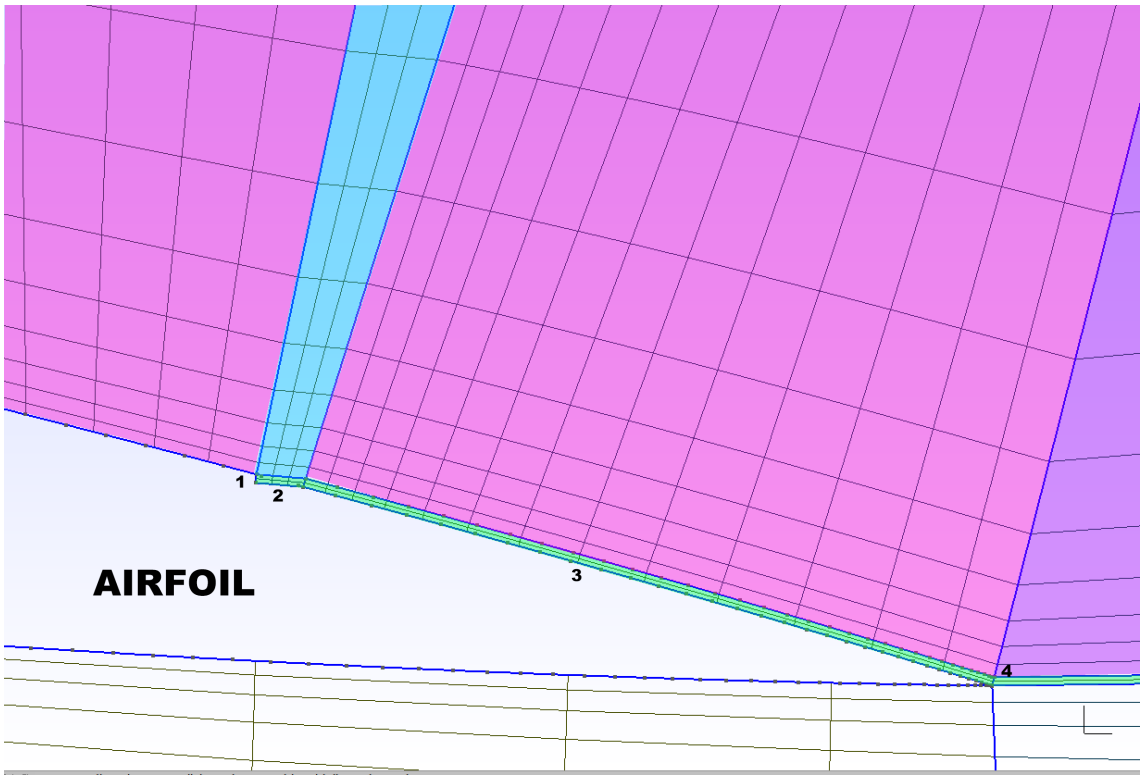

Figure A.12: Mesh structure distribution of the SW jet slot

As it can be observed, there is a change of color in between the Near field mesh and the wake region. These regions are the ones that were described for number 4. If the lower mesh that was inevitably added due to the jet slot wouldn't continue on the other side of the trailing edge, there would be a disrupt of the lines that carry the nodes and that would break the balance, therefore Nektar wouldn't be able to process the information correctly.

By looking back to the Figure A.9 it can be seen that there are only two lines computational nodes going along. This is fair enough as afterwards in the upcoming section , there are the expansions that increase the quantity and the thinness of the mesh to get better definition.

A.3.1. Stream-wise jet conditions

Likewise the normal stream-wise jet, the expansions look exactly the same for the entire simulations as with those value the results obtained are good enough for the whole study. Always with higher density of mesh in the areas where the jet is affecting the aerdonyamics

```
<EXPANSIONS>
  <E COMPOSITE="C[9]" NUMMODES="4" TYPE="MODIFIED" FIELDS="u,v,p" /> <!-- FarField -->
  <E COMPOSITE="C[10]" NUMMODES="6" TYPE="MODIFIED" FIELDS="u,v,p" /> <!-- UpperMidFieldWake -->
  <E COMPOSITE="C[11]" NUMMODES="6" TYPE="MODIFIED" FIELDS="u,v,p" /> <!-- MidFieldExceptUpperWake -->
  <E COMPOSITE="C[12]" NUMMODES="8" TYPE="MODIFIED" FIELDS="u,v,p" />  <!-- UpperNearField -->
  <E COMPOSITE="C[13]" NUMMODES="8" TYPE="MODIFIED" FIELDS="u,v,p" />  <!-- LowerNearField -->
  <E COMPOSITE="C[14]" NUMMODES="8" TYPE="MODIFIED" FIELDS="u,v,p" />  <!-- Wake -->
  <!--<E COMPOSITE="C[7-12]" NUMMODES="4" TYPE="MODIFIED" FIELDS="u,v,p" />--> <!-- All -->
  <!--<E COMPOSITE="C[0]" NUMMODES="7" FIELDS="u,v,p" TYPE="GLL_LAGRANGE" />-->
  <!--<E COMPOSITE="C[0]" NUMMODES="7" FIELDS="u,v,p" TYPE="GLL_LAGRANGE_SEM" />-->
</EXPANSIONS>
```

Figure A.13: Expansions for the stream-wise jet

to have a more reliable results when processing the simulation.

A.3.1.1. Solverinfo of the jet conditions

Moving on to the solverinfo which hasn't been explained in the previous section, the following information is introduced to compute the simulation: After following the tutorials and

```
<SOLVERINFO>
  <I PROPERTY="SOLVERTYPE"              VALUE="VelocityCorrectionScheme"         /> <!--"VCSWeakPressure" "CoupledLinearisedNS"-->
  <I PROPERTY="EQTYPE"                  VALUE="UnsteadyNavierStokes"     />
  <I PROPERTY="Projection"              VALUE="Continuous"               /> <!--"Mixed_CG_Discontinuous" "DisContinuous NO"-->
  <I PROPERTY="EvolutionOperator"       VALUE="Nonlinear"                />
  <I PROPERTY="TimeIntegrationMethod"   VALUE="IMEXOrder2"               /> <!--"BackwardEuler" "BDFImplicitOrder2"-->
  <I PROPERTY="Driver"                  VALUE="Standard"                 /> <!--"Adaptive"-->
  <I PROPERTY="AdvectionForm"           VALUE="SkewSymmetric"            /> <!--"Convective"-->
  <I PROPERTY="Extrapolation"           VALUE="Standard"                 /> <!--"SubStepping"-->
  <!--<I PROPERTY="SubStepIntScheme"        VALUE="ForwardEuler"          />-->
  <!--<I PROPERTY="GlobalSysSolve"         VALUE="IterativeStaticCond"   />-->
  <!--<I PROPERTY="SmoothAdvection"        VALUE="True"                  />--> <!--"False" Use just with nodal expansions-->
  <!--<I PROPERTY="SpectralVanishingViscosity" VALUE="True"              />-->
  <!--<I PROPERTY="DEALIASING"             VALUE="ON"                    />-->
  <!--<I PROPERTY="SPECTRALHPDEALIASING"   VALUE="True"                  />-->
</SOLVERINFO>
```

Figure A.14: Solverinfo of the stream-wise jet conditions file

the guidelines, for the case simulated this were the right solver parameters introduced for Nektar to compute.

A.3.1.2. Stream-wise parameters

First half of the parameters are shared alike the other jet. However, for the second half of the parameters the jet has been modified and so are the numbers for its movement. Therefore, these are the new parameters resulting from the new jet parametrization.

```
  <P> xjet=0.73                </P>
  <P> delta=-80*PI/180        </P>
  <P> b=0.003         </P>


  <P> aoa=-9*PI/180 </P>
  <P> yjet=5*t1*c*(a0*sqrt(xjet/c)+a1*(xjet/c)+a2*(xjet/c)^2+a3*(xjet/c)^3+a4*(xjet/c)^4) </P>
  <P> dytdxja =5*t1*c*(a0/(2*sqrt(xjet/c))+a1+2*a2*(xjet/c)+3*a3*(xjet/c)^2+4*a4*(xjet/c)^3) </P>
  <P> x0=(xjet-c)*cos(aoa)-yjet*sin(aoa)       </P>
  <P> y0=(xjet-c)*sin(aoa)+yjet*cos(aoa)        </P>
  <P> theta=PI/2+atan(dytdxja)-abs(aoa)-abs(delta)  </P>
  <P> x1=x0+b*cos(theta-PI/2) </P>
  <P> y1=y0+b*cos(theta) </P>
  <P> cmu=0.07       </P>
  <P> A=1/(((x0+x1)/2)^2+(x1^2-x0^2)*(x0+x1)/(2*(x0-x1))-x0*(x0+(x1^2-x0^2)/(x0-x1)))  </P>
  <P> B=-A*(x0^2-x1^2)/(x0-x1)        </P>
  <P> C=-A*x0^2-B*x0 </P>

  <P> Am=0.3 </P>
  <P> u0=3/2*sqrt(cmu/(b*(2+Am))) </P>
  <P> fjet=0.892        </P>

  <P> w=2*PI*fjet         </P>
 </PARAMETERS>
```

Figure A.15: Parameters of stream-wise jet

It is important to stress that as mentioned earlier, the amplitude, c_μ and frequency play a major role for this stream-wise jet as each of it can modify the results a lot. In this particular case, the shown data is from the jet located at 73 % of the chord, a $c_\mu = 7\%$ and a frequency of 0.892.

A.3.1.3. Regions of the stream-wise jet

The jet's region's value change a bit in this case. As aforesaid, the equation describing the movement of the jet is different now, it's actually oscillation in stream-wise direction (exactly what it would be seen as the jet is oscillating inwards the z axis).

```
<REGION REF="0">
  <D VAR="u" VALUE="1" />
  <D VAR="v" VALUE="0" />
  <N VAR="p" USERDEFINEDTYPE="H" VALUE="0"/> <!--<D VAR="p" VALUE="0"/>-->
</REGION>
<REGION REF="1">
  <R VAR="u" USERDEFINEDTYPE="HOutflow" VALUE="0" PRIMCOEFF="D0/TimeStep" />
  <R VAR="v" USERDEFINEDTYPE="HOutflow" VALUE="0" PRIMCOEFF="D0/TimeStep" />
  <R VAR="p" USERDEFINEDTYPE="HOutflow" VALUE="0" PRIMCOEFF="1.0/(D0*Kinvis)" />
</REGION>
<REGION REF="2">
  <D VAR="u" VALUE="0" />
  <D VAR="v" VALUE="0" />
  <N VAR="p" USERDEFINEDTYPE="H" VALUE="0" />
</REGION>
<REGION REF="3">
  <D VAR="u" USERDEFINEDTYPE="TimeDependent" VALUE="(A*x^2+B*x+C)*(u0*(1+0.5*Am*cos(w*t)))*cos(theta)" />
  <D VAR="v" USERDEFINEDTYPE="TimeDependent" VALUE="(A*x^2+B*x+C)*(u0*(1+0.5*Am*cos(w*t)))*sin(theta)" />
  <N VAR="p" USERDEFINEDTYPE="H" VALUE="0" />
</REGION>
```

Figure A.16: New region equations for the stream-wise jet

The equation shown above is complemented with the values found in the parameter's section.

A.3.1.4. Filters and functions

As an extra information to complete the annex regarding the adaptation of the mesh, there is this section where it briefly explains how the results were obtained and extracted.

```
  <FUNCTION NAME="InitialConditions">
    <F VAR="u,v,p" FILE="jetmeshbl73.fld"/>
    <!--<E VAR="u" VALUE="0" />
    <E VAR="v" VALUE="0" />
    <E VAR="p" VALUE="0" />-->
  </FUNCTION>

</CONDITIONS>

<FILTERS>
  <FILTER TYPE="AeroForces">
    <PARAM NAME="OutputFile">jh062</PARAM>
    <PARAM NAME="StartTime">0</PARAM>
    <PARAM NAME="OutputFrequency">10</PARAM>
    <PARAM NAME="Boundary">B[2,3,4,5]</PARAM>
    <PARAM NAME="Direction1">
      1 0 0
    </PARAM>
    <PARAM NAME="Direction2">
      0 1 0
    </PARAM>
  </FILTER>
</FILTERS>
```

Figure A.17: Function and filters

The function section "initial conditions" is the one that describes where the simulation has to kick off. At the beginning, everything that was sent to the cluster to simulate was with values equal to zero. However, once there was enough simulations saved, the simulation as restarted from one of those pre-simulated files to save up resources and time of simulations. This is useful as it avoids a longer transitory part at the beginning of the results, it takes fewer time to stabilize the simulations.